2010

Spectrally narrowed leaky waveguide edge emission and transient electroluminescent dynamics of OLEDs

Zhengqing Gan
Iowa State University

Spectrally narrowed leaky waveguide edge emission and transient electroluminescent dynamics of OLEDs

By

Gan Zhengqing

A dissertation submitted to the graduate faculty

in partial fulfillment of the requirements for the degree of

DOCTOR OF PHILOSOPHY

Major: Condensed Matter Physics

Program of Study Committee:

Joseph Shinar, Major Professor
Ho Kai-Ming
Kaminski Adam
Carter-Lewis David A
Dalal Vikram L

Iowa State University

Ames, Iowa

2010

Table of Contents

LIST OF FIGURES

Acknowledgement

First of all, I would like to express my most sincere gratitude to my advisor, Prof. Joseph Shinar. He not only provides a nice research environment but also excellent advice and encouragement so many years. I must also acknowledge his assistance and suggestion in my future career.

I would like to thank to Dr. Ruth Shinar, appreciate all her suggestion, help and support in my research and life.

I would like to show my special thanks to my wife, LinJu. She makes my life full of happiness. She always encourages me move forward and supports my decision.

My appreciation to current and former collaborators in Dr.Shinar's group: Dr. Yun Tian, Dr. Zhaoqun Zhou, for their guidance and suggestion in my research. Dr. Yuankun Cai, Mr. Rui Liu, Dr. Ying Chen for their technical supports on experiments. I also have to say thanks to all the group members for their assistance and suggestions in this long journey of pursuing a PhD degree.

Finally, I would like to thank to my parents for their selfless love and support.

CHAPTER 1 INTRODUCTION TO

ORGANIC LIGHT EMITTING DIODES

Sony's first commercialized television, marketed in 2008, introduced the advantageous attributes of Organic Light Emitting Diodes (OLEDs) in display technology to the general public. Indeed, OLED-based displays and solid-state-lighting markets are expected to increase dramatically in the near future. Generally, an OLED consists of a stack of organic layers sandwiched between a transparent conducting anode and a metallic cathode. When a certain voltage is applied, holes and electrons, from the anode and cathode, respectively, are injected into the device. A fraction of their recombination results in electroluminescence. Both small-molecular and polymer OLEDs have been studied extensively. Their quality has improved significantly during the last two decades—threshold voltage was lowered, power efficiency increased, brightness enhanced, and operational lifetime improved.

OLEDs are ultrathin, flexible, light weight, low-power consumption devices. These attributes make them advantageous over today's flat panel technology, such as LCD or plasma. OLEDs can be used in television screens, computer displays, and small, portable system screens, such as cell phones and PDAs. Numerous companies are active in this field, including Sony, Eastman Kodak, DuPont, Samsung, GE, and Osram. In 1998, Pioneer/Toyota pioneered the first small molecular OLED display for vehicular stereos. Ten years later, the first OLED TV was introduced.

OLEDs also can be used as light sources for general space illumination and large-area light emitting elements. The paper-thin flexible OLED light bulb provides an entirely new way to light a home or business, high efficiency and low power consumption save electric energy. Roll-to-roll fabrication technology lowers the production cost. Although OLED solid-state lighting is still a step away from commercialization, we have already seen a new illumination technology. The first OLED table light prototype was unveiled on May 2008 in Las Vegas by OSRAM. This predicted the revolution in lighting illumination has already begun.

In parallel, organic transistors, solar cells, semiconductor memory, and organic semiconductor lasers are under development. Due to the potentially low cost and variety of organic materials, the fast development of the organic electronics devices is expected to soon share the market dominated by the inorganic semiconductor devices.

1.1 History of OLEDs

The first electroluminescence (EL) in organic materials was produced by Bernanose and co-workers at Universite de Nancy, France in 1953.[1] A high voltage alternating current (AC) field was applied to acridine orange and quinacrine, either deposited on or dissolved in cellulose or cellophane thin films.[2,3,4] In 1963, Pope and co-workers[5] applied high voltage and direct current (DC) to a single crystal anthracene and single crystal anthracene doped with 0.1 mole % teracene; EL was observed in both devices. Due to the thick anthracene crystal, the driving voltage was incredibly high (more than 100 V). Although Vincett reported the driving voltage of blue light emitting anthracene crystal devices was significantly lowered by vacuum depositing anthracene films,[6] the external

quantum efficiency was only ~1% and the device degraded fast, due to the high voltages. Later in 1977, powdered graphite electrodes were used in anthracene crystals and the external quantum efficiency achieved 4-6%.[7]

Poor efficiency and high driving voltage of these devices did not attract industry's interest. A breakthrough was achieved by Tang and VanSlyke in 1987.[8] A double layer structure of organic thin film diode was prepared by vapor deposition. N, N'=diphenyl-N, N'-bis (3-methylphenyl) 1,1'-biphenyl-4, 4' diamine (TPD) and tris (8-hydroxyquinoline) aluminum (Alq_3) were thermally evaporated with a total thickness of 100 nm. Higher external quantum efficiency (1%) and luminous efficiency (1.5 lm/W) were achieved when a low driving voltage (less than 10 V) was applied across the diode. This breakthrough gave hope for the use of these organic materials and showed the potential of OLEDs as a new promising display technology. They attracted worldwide industry and academia attention and interest, and extensive studies followed. More and more functional layers were introduced into the device structure. In addition to the electrodes, most of the devices include a hole injection layer, a hole transport layer, an emission layer, an electron transport layer, and an electron injection layer.

Polymers were considered insulated materials for a long time, but in 1977, Shirakawa and co-workers reported high conductivity in oxidized and iodine-doped polyacetylene at room temperature.[9] This ground breaking and significant discovery opened a new field of polymer semiconductors, leading to the 2000 chemistry Nobel Prize awarded to Heeger, MacDiarmid, and Shirakawa.

Following the successful improvement in fabricating small molecular OLEDs, Friend and coworker[10] described the first polymer light-emitting diode (PLED) fabricated by

spin coating a precursor polymer of the luminescent Poly(p-phenylene vinylene) (PPV) onto an indium tin oxide (ITO)-coated glass substrate and then thermally converted it to PPV. The standard methods of depositing polymer films are spin-coating and inkjet printing using their solutions, since thermal treatment can cause polymer cross-linking or decomposition. Thus, a high vacuum system, used for thermal evaporation of small molecules, is not needed. Ink-jet printing[11] for depositing polymer materials can be used in future roll-to-roll fabrication to lower the fabrication cost. This is the intrinsic potential advantage of PLEDs over small molecular devices.

Fluorescent emission is the main mechanism of OLED light emission. The internal quantum efficiency of OLEDs and PLEDs is limited by this intrinsic mechanism, due to the 25% statistical probability of fluorescing singlet states and 75% of phosphorescent triplet states. Hence, the ideal maximum fluorescence yield is limited to 25%. To overcome this limitation of fluorescent materials, Baldo[12] used phosphorescent dyes (transition metal compounds with organic ligands or organometallic compounds) as dopants in appropriate host materials, which resulted in impressive external quantum efficiencies. This is due to the fast and efficient intersystem crossing (ISC) that increased the internal quantum efficiency to a value higher than 90%, which theoretically could reach 100%.[13,14]

Along with the improvement in OLED quality, industry made a lot of effort on commercialization of OLED displays, due to the advantages of OLEDs in large displays. In 1996, CDT gave the world's first public demonstration of Light Emitting Polymer devices. In 1998, Kodak and Sanyo showed a full-color active matrix organic display; it was the first color organic EL (OEL) display, which increased OLEDs' competitive edge

and led to an increased R&D effort by a number of companies (UDC, Pioneer, Toshiba, Motorola, LG). In 2003, Kodak introduced the first digital camera with an OLED screen. In 2007, the emergence of the Sony's First OLED TV XEL-1 excited the world.

The price of OLED products is relatively high, because the thermal evaporation deposition is still the main fabrication technique. However, in March 2008, GE demonstrated the world's first OLEDs manufactured by the roll-to-roll technique, a key step toward making OLEDs and other organic electronics products at dramatically lower costs than possible today.

1.2 OLED Structure

OLEDs basically consist of three kinds of layers—an ITO anode, organic layers, and an aluminum cathode. These thin film layers are deposited on a glass or a flexible polymer substrate. When holes and electrons are injected into a single organic layer from these electrodes, they recombine near the cathode because the mobility of holes is usually much larger than that of electrons in most organic materials. Thus, the quenching and absorption by the cathode result in an extremely low efficiency. Hence, multilayer devices were developed to increase the device's efficiency. Appropriate multilayer structures enhance the performance of the devices by lowering the injection barriers from the electrodes and by enabling the controlling of the recombination region, moving it away from the organic and cathode interfaces. An OLED multi-layer structure, including the ITO anode, hole injection layer (HIL), hole transport layer (HTL), electron blocking layer, emissive layer (EML), hole blocking layer, electron transport layer (ETL), and electron injection layer (EIL), is shown in Figure 1-2. Some organic materials can play

multi-functions. For example, Alq_3 can work as an ETL and EML, simplifying the device structure. The HTL fulfills the role of assisting the injection of holes from ITO and transporting them to the recombination zone, which locates within EML, while the ETL assists the injection of electrons from a metal cathode. Recombination then occurs in the EML or at the interface of organic layers (between HTL and ETL). As mentioned previously, a separate EML is not always necessary, because both the HTL and the ETL can function as an EML. If the recombination happens in the HTL(ETL) side of the interface, the HTL(ETL) behaves as an EML. The HIL and EIL are also termed buffer layers; copper phthalocynine (CuPc) is a typical buffer layer on the anode side. 5 nm CuPc smooth the ITO surface and lower the hole injection barrier; thus, the quality of OLEDs can be significantly improved. LiF is a typical EIL; it helps enhance the electron injection by forming a dipole layer or lightly doping the ETL. To further enhance carrier injection and transportation, a graded junction layer[15] is introduced. Generally, this layer is between the HTL and EML, and its components gradually change from a pure hole transporting material to an emissive material. Thus, although the barrier between the HTL and EML does not change, the interface is enlarged, and the total carriers, which hop from the HTL to the EML, increase.

More advanced OLED structures were introduced recently. Tandem OLEDs (Figure 1-1), which have multiple emitting units stacked vertically in series, were reported to be useful for providing high luminance, enhancing the current efficiency, and tuning the emission spectrum.[16,17,18] The units in the tandem OLED can be nominally identical or of different structures with a particular design. One of the most important components of tandem OLEDs is the connection layer between the different units, i.e., the charge

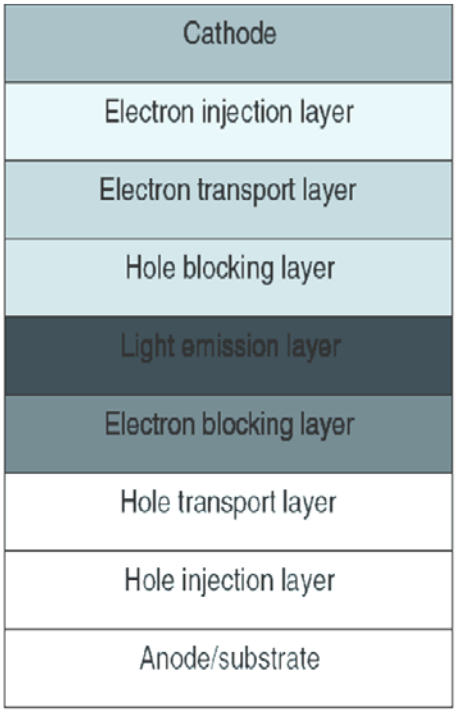

Figure 1-2 Multilayer Small Molecular OLED

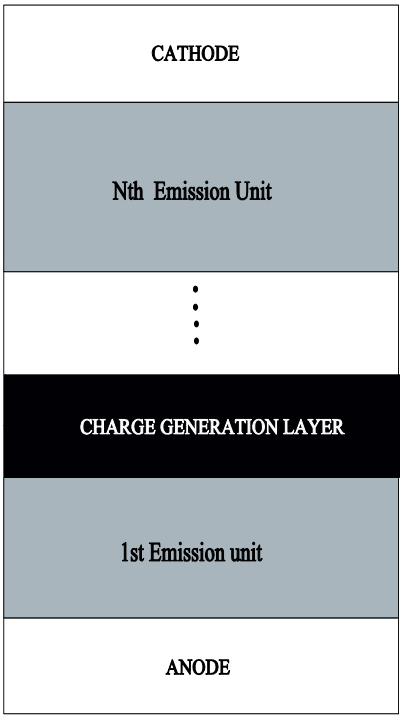

Figure 1-1 Tandem OLED structure

generation layer. Straightforward thinking is to insert transparent anode and cathode layers side-by-side at the interface between units. For simplifying the fabrication and device structure, multi functional materials, which could serve both as HIL and EIL, were introduced and synthesized. ITO, V_2O_5, WO_3, MoO_3 or p-type organic materials are typically used as HIL, and n-type organic electron transport materials doped with low work function metals, such as Cs, Li, and Mg, are used as EILs. By properly choosing structures of units with different emission colors, tandem OLEDs could emit white light with high efficiency, which is attractive in solid-state illumination.[19]

A large part of the emission is guided and lost in the organic thin film and glass substrates, because a waveguide structure is formed due to refractive index mismatch between different layers. Several approaches have been developed to increase the extraction efficiency of the surface emission. These approaches include geometric patterning (micro-lens arrays (MLAs),[20,21] surface roughing,[22] nano-pyramids,[23] concave lens[24]) micro cavity OLEDs,[25] low index grids,[26] and distributed feedback (DFB)-OLED structures.[27]

1.3 Molecular Materials for OLEDs

Organic semiconductors are π-conjugated materials, where single and double or single and triple bonds alternate throughout the molecule or polymer backbone. According to their molecular weight, organic materials can be classified into two categories—small molecule and polymer. Organic materials also can be divided by their function—hole-transport materials (HTMs), electron transport materials (ETMs), emitter materials (EMs), and dopant materials. Organic layers are the main components of the

OLED devices, and organic materials are the key to improve the device quality. More and more efforts are put into synthesis of new organic materials with good conductivity, high quantum efficiency, and stability. By tuning the HOMO (Highest Occupied Molecular Orbital) and LUMO (Lowest Unoccupied Molecular Orbital), the emission color of organic materials can be controlled. And, a new class of materials, known as n-conjugated organic compounds,[28] has been developed, which can even emit white light individually. Fast development of the organic materials stimulates and guarantees the growing of OLED applications.

1.3.1 π-Conjugated Materials

A carbon-carbon bond is a covalent bond. The single bond is a sigma (σ) bond and the double bonds are π bonds as shown in Figure 1-4. In these bonds, the s orbital and two of the three p orbitals of the C atom form three sp^2 hybrid orbitals, which lie in a plane with an angle of 120° in between; the sp^2 orbitals of the two adjacent C atoms form the σ bond. The remaining p orbitals of these adjacent C atoms overlap and form the π bond perpendicular to the sp^2 plane. The π bond has regions of electron density on either side of the carbon nuclei plane, but has no electron density directly between the nuclei. π bonds are usually weaker than σ bonds because their electron density is farther from the positive charge of the carbon nucleus.

The aromatic ring often found in π-conjugated materials is modeled as a six-membered carbon ring with alternating single and double bonds, or more precisely, the electron density evenly distributed through a π bond above and below the ring plane as shown in Figure 1-3. The σ orbitals are localized and concentrated mainly between the

carbon nuclei, but the electrons forming the π orbials are delocalized over all the atoms and are responsible for the π-conjugated materials' semiconducting properties.

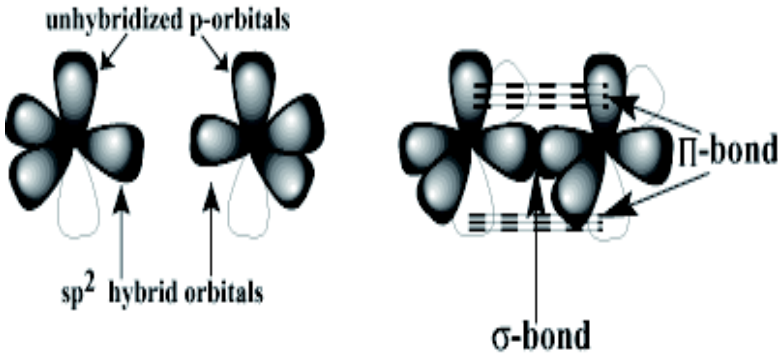

Figure 1-4 the formation of π conjugated bond

The orbitals with the lower energy are the bonding molecular orbitals; the orbitals with the higher energy are the anti-bonding molecular orbitals. Benzene has six molecular orbitals, three bonding (which contain six π electrons) and three anti-bonding. The degenerate bonding orbitals are the highest occupied molecular orbital (HOMO) of benzene. And, the degenerate anti-bonding orbitals are the lowest unoccupied molecular

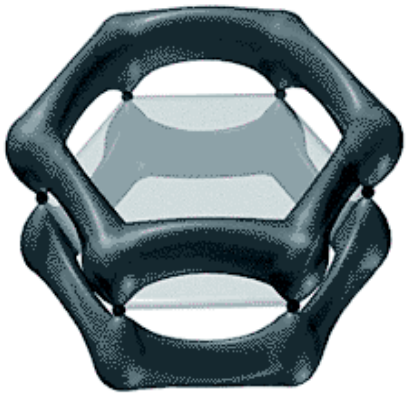

Figure 1-3 Electron density distributed through the pi π bond above and below the benzene ring

orbital (LUMO). The HOMO corresponds to the top of the valence band in inorganic semiconductors and the LUMO corresponds to the bottom of the conduction band. The transition of electrons between the HOMO and LUMO results in absorption or emission of photons.

1.3.2 Electronic Processes in Organic Materials

Generally speaking, when holes and electrons are injected into organic materials, they are hopping between organic molecules (or segments of a polymer) due to the external electric field. If an electron and a hole happen to hop onto the same molecule, Coulombically-bound electron-hole pair, called exciton, forms. Exciton dynamics is of primary importance in OLEDs. The binding energy of the electron-hole pair is large ~$1eV$, a Frenkel exciton.

For non-doped devices, the electron and hole recombine in single component materials. The excited molecular singlet can relax directly to the ground state, or by intersystem crossing to an excited molecular triplet, and their radiative decay produces fluorescence and phosphorescence, respectively. The interaction of an excited molecular state with a ground state molecule leads to formation of a locally excited excimer or charge transfer excimer, if the distance between molecules is shorter than 0.4 nm. If the distance is larger than 0.4 nm, a direct transition from the LUMO-located electron of one molecule to the HOMO-located hole of another molecule could happen—such “emitting state” is called electromer.

In the case of doped devices, the situation becomes complicated. Excitons can form in the host material whose energy transfers to guest molecules rapidly, and the doped

material emits light. The interaction of the excited host molecule and the ground state guest molecule can form exciplexes and electroplexes.[29,30] Another situation is the donor can trap electrons or holes, and exciton forms on donor molecules directly without energy transfer.

In principle, the macroscopic properties of a multi molecular system can be deduced by solving the Schrödinger equation, but it is too complex to obtain analytical solutions even for the simplest molecules. Thus, the Born Oppenheimer (BO) approximation is used to simplify the situation. It assumes the nuclear position is fixed and the electrons can respond instantaneously to any change in the configuration of the nuclei. The energy level of molecules can be determined under this assumption. The BO approximation results in the Franck-Condon principle in optical transitions.

The ground state of most stable molecules is a singlet, and usually only singlet excitons can decay radiatively. Fluorescence is the radiative transition from the lowest excited singlet state to the ground state. This process is very fast with a lifetime of ~1 ns. Phosphorescence is a radiative transition from the lowest triplet state to the ground state, due to intersystem crossing. And, the lifetime of this process is typically microseconds to milliseconds.

In guest-host systems, the energy of the donor molecule can transfer to the acceptor molecule. There are two types of resonance energy transfer processes—Förster and Dexter energy transfer. Förster is a long-range energy transfer process, typically occurring in a distance of 10~100 Å. Dexter energy transfer is a short-range transfer, and

it only occurs over a distance of ~10 Å. Electron exchange is the dominant interaction in the Dexter energy transfer.

1.3.3 Materials for OLEDs

The attributes of the organic materials are crucial for increasing the efficiency and brightness of the OLEDs. More and more organic materials are synthesized to reach the requirement of the high quality OLEDs—high efficiency, high carrier mobility, high crystallization temperature, and robustness. Materials, which have different functions, are presented next.

1.3.3.1 Hole Transport Materials.

Because the energy barrier at the interface of directly contacting ITO and organic emitting materials is high and holes are not easily injected into the organic layer, HTLs are always inserted between anode and the EML to lower the energy barrier. Good HTL materials should satisfy one or more of the general requirements.[31] They should be morphologically stable and form uniform thin films, have a small ionization potential, hole mobility should be high, and solid-state electron affinity should be small.

These requirements can be used as general guiding principles for selecting hole transport materials. N, N'- diphenyl- N, N'- bis(3-methyl phenyl)- 1, 1'- biphenyl- 4, 4'- diamine (TPD), one of the aromatic diamines, has been used as a typical HTL material, due to its excellent hole injection, transport properties, and its good electron blocking capability. However, its glass transition temperature is only 63 ℃, so the vacuum sublimed thin TPD film is not stable. Other diamine derivatives, including N, N'- diphenyl- N, N'- (2- napthyl)- (1, 1'- phenyl)- 4, 4'- diamine (NPD) and spiro- TPD,

have been used.[32] The better stability of these materials enhances the quality of OLED devices.

Tang et al. first demonstrated that phthalocyanines, $CuPc$ and H_2Pc, with an ionization potential around 5.0 eV, which is close to the ionization potential of ITO, worked well as HTL, but PCs have large absorption in the visible region.[33] The starburst polyamine[34] (m- MTDATA) has less absorption in the visible region and the ionization potential is $5.1 eV$. The excellent amorphous morphology of m-MTDATA enhanced device stability. HTL can also act as an electron-blocking layer to prevent the flow of electrons transferring through the EML reaching the anode. For this purpose, a shallow LUMO level is desirable. Commonly used HTL materials fall into three simple classes:

1. Triarylamines
2. Triphenylmethanes
3. Phenylazomethines

TPD, NPD, and m-MTDATA are all triarylamines. For advanced OLED structures, hole transport materials can be further divided into HTL-A (hole transport layer in contact with the anode) and HTL-E (hole transport layer in contact with the EML). This type of double HTLs further lowers the energy barrier and is indispensable for high performance OLEDs.

1.3.3.2 Light Emitting Materials.

As mentioned previously, EML is deposited above the HTL. Actually, if the hole or electron transport materials possess a bipolar carrier transport characteristic and highly efficient fluorescence, they can be used as the emitting material. In small molecular

OLEDs, guest-host systems are very common, but in PLEDs, the emission layer is usually composed of a single polymer.

An emission material is able to transport both holes and electrons so the charge carriers are able to hop into EML layers and recombine. The recombined charges then create excitons, where a fraction will decay radiatively and emit light. For long-lived devices, a mixture of materials must remain in uniform dispersion and not be subject to material migration under an applied electric field.

Alq_3 is a stable green emitter for small molecular OLEDs and metallic complexes of this type have many of the desired stability and film forming properties necessary to provide useful performance. A thorough investigation was conducted in which Alq_3 derivatives were examined systematically.[35,36] Oxadiazoles provided the source material for the first blue OLED,[37,38] but these devices have a short life span. Distyrylarylenes, generally blue emitting materials, were studied extensively by Hosokawa and coworkers.[39] 4, 4'- bis (2, 2'- diphenylvinyl) -1, 1'- biphenyl (DPVBi) has proven to be a particularly promising material for blue OLEDs. However, its glass transition temperature (T_g) is only 64 ℃. The related spiro-DPVBi, with T_g ~100 ℃, yields considerably more stable devices.[40]

1.3.3.3 Electron Transport Materials

The ETL is deposited after the EML to help transport electrons from the cathode to the organic layers. Ideally, electrons are transported via a hopping mechanism. So, the LUMO of the ETL needs to be close to the work function of the cathode to lower the energy barrier. As with other organic layers, it should form uniform and relatively stable amorphous films and have high T_g. Meanwhile, most ETMs also serve as hole blocking

layers to effectively confine the exciton formation in the EML. An ETM is necessary to balance the charge injection and transport, and it significantly improves the performance of the OLEDs.

There are several classes of chemical structures of useable ETMs:

1. Metal chelates
2. Oxadiazole compounds
3. N=C (imine) containing quinoline, anthrazoline, phenanthraline, and pyridine compounds
4. Cyano and F-substituted compounds

Time-of-flight (TOF) and electron-only diode measurements as well as the overall OLED qualities are used to determine or justify the quality of the electron transport properties of ETM. Alq_3 was the first emission and electron transport material explored by the Kodak group and is used in almost all long-lived OLEDs. The electron mobility of Alq_3 is $\sim 1.4 \times 10^{-6}\ cm^2/(Vs)$, two orders higher than its hole mobility $2.0 \times 10^{-8}\ cm^2/(Vs)$. The HOMO energy level is ~5.95 eV and its LUMO energy level is ~3.00 eV.[41] It is stable and has a T_g of 172℃. Besides the aluminum hydroxyquinolinate chelates, other chelates of substituted 8-hydroxyquinoline, such as those with Zn^{2+} and Be^{2+}, have also been used as the ETM in OLEDs.[42,43]

1.3.3.4 Dopants

Dopant materials can be doped into host materials for obtaining not only high EL quantum efficiency, but also a longer life-time. The HOMO and LUMO energy of dopant materials should match that of the host materials, and the energy transfer process from host to guest should be very fast.

a) Fluorescent dopants

(10-(2-benzothiazolyl)-1,1,7,7-tetramethyl-2,3,6,7-tetrahydro-1H,5H,11H-[l]benzo-pyrano[6,7,8-ij]quinolizin-11-one) (C-545T) is an important green laser dye. It has high fluorescent quantum efficiency (QE) in both its dilute solution and solid film. 4-(dicyanomethylene)- 2- methyl- 6- [p- (dimethylamino) styryl]- 4H- pyran (DCM) is a bright and efficient red arylidene laser dye.[44] The device with DCM-doped Alq_3 showed an external QE (EQE) of 2.3%. The emission is orange-red peaking in the range of 570~620 nm. High concentration doping will result in concentration quenching. 4,4'-(Bis(9-ethyl-3-carbazovinylene)-1,1'-biphenyl (BCzVBi) is a blue dopant and belongs to the distyrylarylene series. When it is doped into DPVBi, the device could achieve luminous efficiency of 1.5 lm/w with EQE of 2.4%. The highest brightness exceeds 10000 cd/m^2.[45]

b) Phosphorescent dopants

Iridium organometallic complexes are one of the most important high efficiency phosphorescent dopant materials. The triplet lifetime of this class of materials is normally around 1-100 μs, and, the QE is high at room temperature, and the color can be easily tuned by modification of the ligand chemical structure. $Ir(ppy)_3$ was the first iridium complex studied.[46] Its triplet lifetime is ~1 μs and the efficiency is about 40% at room temperature.[47] When doping 6% $Ir(ppy)_3$ into 4,4′ -bis(9-carbazolyl)-2,2′ -biphenyl (CBP), the device exhibited a high QE of ~8%. Pt(II) octaethylporphine (PtOEP) was one of the first conlanthanide phosphorescent organometallic complexes used.[12] It has a narrow red emission band centered at ~650 nm. But, its long triplet lifetime of PtOEP leads to low QE, especially in high current conditions. Iridium(III)bis[(4, 6- di-

fluorophenyl)- pyridinato- N, C2'- picolinate] (Firpic) is a blue phosphorescent dopant. When doped into CBP, the maximum QE reached 6% and the luminous power efficiency was 7.7 lm/W with peak luminance of 6400 cd/m^2.

1.4 OLED Fabrication Methods

As mentioned above, there are two major OLED categories: 1) small molecule OLEDs (SMOLEDs) and 2) PLED. The fabrication techniques for them are different. Thermal evaporation is used in SMOLEDs, and spin coating or ink-jet printing[48] techniques are used for PLEDs. Besides, organic vapor phase deposition (OPVD), thermal transfer,[48] organic molecular beam deposition (OMBD),[49] and "roll to roll" have also been used to deposit thin organic layers.

1.4.1 Thermal Evaporation

Small molecular organic layers are deposited sequentially onto the substrate with anode by thermal evaporation. A base pressure of ~10^{-6} Torr or better is needed for thermal evaporation. The evaporation chamber often contains several different material sources to increase experimental efficiency. At the bottom of the evaporation chamber, heating coils are placed between pairs of electrodes. Ceramic baskets (e.g., boron nitride, aluminum oxide, and quartz) or metallic boats (e.g., tantalum or molybdenum) are used as an organic material container, and installed in the heating coils. One of the most salient advantages of thermal evaporation is the thickness of each layer in multilayer devices can be controlled precisely. The evaporation rate, monitored by quartz oscillators, is typically in a range of 0.1~3 Å/s. Most organic materials have a high vapor pressure at temperatures lower than their melting point. Therefore, the materials are sublimed for deposition. However, the risk of cross contamination between evaporation sources exists,

since several materials are in the same chamber. This has negative effects on the quality of OLEDs.

Due to the intrinsic property of the point source, the thickness of an organic film in the center of the substrate is larger than at the edge of the substrate. To enhance the uniformity of the film, the distance between the point source and the substrate should be large. Alternatively, some manufacturers are developing linear sources,[50] and either the source or the substrate is transferred in one direction. Such geometry could deposit uniform films without a great distance between source and substrate, and also enhance the material usage and deposition rate.

Two-dimensional combinatorial fabrication techniques[51] can be used in thermal evaporation to enhance the experiment efficiency and accuracy in comparing devices. A top plate with a sliding shutter is used in the evaporation system. The shutter position can be controlled easily by a rotating knob on the other side of the plate. Thus, the shutter can partially cover the substrate. By using this technique, the thickness of organic layers can be varied systematically across the substrate's surface, and devices with different structures can be relatively easily fabricated in a single deposition procedure for optimizing the device structure.

1.4.2 Spin Coating Technique

Due to the large molecular weight and crosslink of polymers upon heating, they cannot be thermally evaporated in a vacuum chamber. So, spin coating is generally used to deposit polymer films. It is a preferred method for fabrication of thin, uniform films on flat substrates. An excess amount of polymer solution is placed on the substrate, and then the substrate is rotated at high speed to spread the fluid by centrifugal force. The rotation

speed and material concentration in the solution determine the film's thickness. This solution-based process imposes restrictions on the nature of the polymers and side groups are attached to the polymer's backbone to make it soluble. Hence, for some insoluble polymers, a soluble precursor polymer is spin coated onto a desired substrate first and then converted to the polymer by annealing at a certain temperature. For example, PPV films are fabricated by spin coating PPV precursors, which will be converted to PPV by annealing at ~200 ℃ for 24 hours.[10,52]

Usually, PLEDs are single layer devices, because spin coating another polymer above the already coated film may wash away and damage the existing film. To fabricate multi layer PLEDs, a careful selection of polymer solution is necessary. Only solvents, which would not redissolve the deposited film, can be used to deposit additional layers.[53]

As mentioned, the thickness of the polymer film can be roughly controlled by the concentration of the polymer solution and the spinning revolution. A disadvantage of spin coating is the thickness of the film cannot be monitored during deposition and the combinatorial fabrication method cannot be integrated into spin coating. Another limitation of this method is it does not provide a method to fabricate full color displays, but it has been established as a promising technique to make small size monochromatic displays.

1.4.3 Organic Vapor Phase Deposition (OVPD)

The growth of molecular organic thin films by OVPD was initially used by Forrest et al. It has proven useful for organic semiconductor deposition and for patterning the device with micron resolution. Vapor phase epitaxial is used extensively in the inorganic

semiconductor industry and the analogous technique is introduced for organic material deposition.

In OVPD, the organic material is thermally-evaporated and an inert carrier gas, such as nitrogen, is used to dilute and carry the vapor, and then transport it in a hot-walled reactor toward a cooled substrate. Uniform coatings can be achieved by controlling the flow pattern. The hot deposition chamber prevents the organic material from condensing anywhere but on the substrate's surface, therefore, improving the efficiency of material usage. Since the organic material vapor is carried and transported by an inert carrier gas, the position of evaporation sources can be outside of the reactor tube, spatially separating the function of evaporation and transport. The deposition process can be precisely controlled, due to the fact the deposition rate is controlled by the mass flow controllers rather than the temperature of a thermal source, because small changes in temperature have a significant effect on deposition rate. OVPD avoids this problem by controlling the flow of the carrier gas.

1.4.4 Ink Jet Printing

Most of the companies working on OLED displays focus on ink-jet printing as the method for depositing organic films. This method offers substantially higher productivity than traditional, high temperature, and vacuum technologies. The ink jet process relies on using a piezoelectric print-head to create deformation on a closed cavity through the application of an electric field. The volume of a nozzle through which the fluid in the cavity is ejected can be determined by the applied voltage, nozzle diameter, and ink viscosity. The final width of the printed pixel is a result of the volume of fluid expelled and the thickness of the droplet. Usually, hundreds of print-heads are needed to obtain a

reasonable print speed. Thus, the reliability and the uniformity of the print-heads is a concern for high-speed, large-scale manufacturing.

1.4.5 Other Organic Deposition Methods

Laser thermal transfer method[54] was invented in Eastman Kodak. Their method is used for patterning high-resolution OLED displays. A light-absorbing layer, which produces heat in response to light, is disposed over a substrate called donor element, and an emissive layer is disposed over the light-absorbing layer. When the donor element and the OLED accepter substrate are in position for transferring, and the light is absorbed by the light absorbing layer, then the generated heat causes the vaporization transfer of the emissive material to the OLED across a gap.

Organic Molecular Beam Deposition (OMBD)[55] is a method for depositing organic crystalline films. The deposition system follows the conventional molecular beam epitaxy systems and an ultra high vacuum (UHV) condition is required. This allows the reproducible growth of complex layer sequences with a defined thickness of various organic semiconductors. The growth rate is in the range of 1~5 nm/min, much lower than the thermal evaporation method which could only form amorphous films. Due to the precise controlling of the film thickness, device structure can be optimized easily.

Roll-to-roll processing is a technology still in development. The patterning of the device is obtained through modification of the rolls used to deposit the ink. This method almost takes full advantage of organic materials and will save cost greatly. GE first demonstrated the roll-to-roll manufacturing process. This should be a major step towards getting OLED lighting devices into mass marketing.

1.5 OLED Basic Operational Mechanism

A simple OLED is constructed by a thin organic layer sandwiched between two electrodes. When applying a forward bias between the electrodes, holes are injected from the anode and electrons from the metal cathode. These carriers drift through the organic layer by the external electric field. Holes and electrons will recombine in the organic layer and form excitons, and some of these excitons will decay radiatively, resulting in light emission. Briefly, the OLED emitting process includes charge injection, transportation, and recombination.

1.5.1 Carrier Injection

Organic material is usually considered as insulator with the resistivity in the range of 10^{15} Ω ~10^{20} Ω at low electric fields ($< 10^4\ V/cm$). This implies organic materials have a low intrinsic carrier concentration and mobility. When a contact between the electrode and the organic is established, there is some initial injection of electrons into states in the organic/metal interface. The "image force" potential, due to the Coulomb attraction between electrons and holes, will lower the energy of the interface barrier and result in the electrons hopping from the metal Fermi surface. While without external electric field, the charge still cannot hop into the bulk states deep in the organic layer. Application of the external electric field lowers the energy level in the bulk of organic layer and the charge can hop into it to form a continuous current. Microscopically, carrier hopping can be described as a tunneling from a thermally-excited state in the metal to the HOMO or LUMO of the organic molecule.

The flow of the hopping charge current along the direction perpendicular the substrate through the organic film can be expressed by

$$j = j_s(x) + e\mu n(x)\left[F - \frac{e}{16\pi\epsilon_0\epsilon x^2}\right] - eD\frac{dn(x)}{dx}$$

where n(x) is the coordinate-dependent concentration of free charge carriers and D is their diffusion coefficient directly related to the carrier mobility (μ) through the Einstein relation $D = \mu kT/e$. The current contains three parts—hot carrier stream of $j_s(x)$, drift current, and diffusion current.

If the diffusion current term is negligible, the drift current in the combined image and external electric fields dominates.

$$j = j_0 \exp\left(-c/F^{1/2}\right)$$

where $c = l^{-1}(e/16\pi\epsilon_0\epsilon)^{1/2}$ for hot carriers penetrating the sample with the mean free path l or $c = \left(\frac{2\pi}{h}\right)(em^*\chi_c/2\pi\epsilon_0\epsilon)^{1/2}$, assuming the carriers to be one-dimensional Bloch waves damped within the potential threshold; F is the electric field. When the trapping of the charge carrier is taken into account, $c = (e^2/16\pi\epsilon_0\epsilon\mu kT\tau_{trap})^{1/2}$, where τ_{trap} is the carrier trapping time.

More precisely, the drift-diffusion equation is solved by considering both the drift and diffusion effects. Based on inorganic semiconductors, the Richardson-Schottky thermal emission process is given by:[56]

$$J = \frac{4\pi emk_B}{h^3}T^2 \exp\left(-\frac{e\Phi_B}{k_BT}\right)\left[\exp\left(\frac{eV}{k_BT}\right) - 1\right]$$

where h is the Planck constant, m is the effective mass of the carrier, k_B is the Boltzmann's constant, Φ_B is the barrier height, and V is the applied voltage. However, this thermionic emission injection mechanism cannot achieve high current density in OLEDs. But, some deliberate treatment at the interface of the organic layer and metal,

such as doping, could increase the current injection by increasing both the intrinsic carrier concentration and mobility.

At high electric fields, the image field barrier approaches a triangular shape and the collected current is governed by tunneling. Fowler-Nordheim (FN) tunneling theory is used here to predict the tunneling current:[57]

$$j = BF^2 \exp(-bF)$$

and

$$b = [4(2m_e^*)^{\frac{1}{2}}/3\hbar e]\chi_c^{3/2}.$$

Here, B is a constant and m_e^* is the effective mass of electron. χ_c is the injection barrier referred to the Fermi level of the injecting electrode.

However, the FN tunneling current is temperature independent, but the current-voltage curve of OLEDs is temperature dependent.[58] Thus, only the tunneling current cannot fully explain the current injection mechanisms. But, at a relatively lower barrier and high electric field, the FN mechanism is still acceptable. So, at the present, to understand injection mechanism, the thermal emission model is adopted at low bias and the FN tunneling model is used at high bias.

1.5.2 Carrier Transportation

Due to the low intrinsic carrier concentration of organic films, Ohm's law is followed at a low applied voltage and the electrode can supply more carriers per unit time than can be transported through the sample. Such type of organic/metal contact is called Ohm contact. In practice, an electrode can only be Ohmic if the injection barrier is small enough to ensure that no field-assisted barrier lowering is required to maintain a sufficiently high injection rate.[59] At high electric fields, the injected carrier density would

be larger than the intrinsic carrier density and form space charges near the organic-electrode interfaces. In this case, for the perfectly ordered or disordered insulating materials, or those containing very shallow traps, the current will obey Child's law:

$$j_{scl} = \frac{9\ \varepsilon_0 \varepsilon \mu F^2}{8d} = \frac{9\ \varepsilon_0 \varepsilon \mu V^2}{8d^3}$$

Here, ε_0 is the vacuum dielectric constant, ε is the relative dielectric constant, μ is the microscopic mobility of the carriers, d is the thickness of the organic film, F is the electric field, and V is the voltage.

At low voltage, the J-V characteristic is Ohmic, as mentioned above, because the thermally-generated free carriers are predominant:

$$j = qp_0\mu\frac{V}{d}$$

and the transition voltage is

$$V = \frac{8qp_0d^2}{9\ \varepsilon_0\varepsilon}$$

In the presence of discrete traps:

$$J_{scl} = \frac{9\ \varepsilon_0 \varepsilon \Theta \mu F^2}{8d} = \frac{9\ \varepsilon_0 \varepsilon \Theta \mu V^2}{8d^3}$$

Θ is the fraction of free to trapped space charge:

$$\Theta \cong \frac{N_{eff} exp\ (-E_t/kT)}{H - n_t}$$

N_{eff} is the effective density of electronic states, and E_t and H are discrete trap depth and trap concentration, respectively.

In organic semiconductors, however, the traps are distributed in energy according to often assumed exponential function $h(E) = (H/lkT)exp(-E/lkT)$ with total

concentration of traps H and a characteristic distribution parameter l, the space charge layer (SCL) current can be expressed as:[60]

$$J_{SCLC} = \frac{N_{eff} e\mu}{H^l} \left(\frac{\varepsilon_0 \varepsilon}{e}\right)^l \left[\frac{l^2 \sin[\pi/l]}{(l+1)\pi}\right]^l \left(\frac{2l+1}{l+1}\right)^{l+1} \frac{F^{l+1}}{d^l}$$

Unlike inorganic semiconductors whose carrier mobility is generally independent of the applied field, the carrier mobility of most organic materials strongly depends upon the external electric field. The hole mobility is typically $10^{-7}\sim10^{-3} cm^2/Vs$, and the electron mobility is lower by a factor of 10~100. Such low mobility is due to the disorder in the amorphous or polycrystalline materials. Carrier mobility is usually measured by TOF,[61] and compared with an analysis of dc current-voltage characteristics.[62] The universal dependence of charge carrier mobility on the electric field is

$$\mu(E,T) = \mu(0,T)\exp\left(\gamma\sqrt{E}\right)$$

where $\mu(0,T)$ is the low field mobility and γ is an empirically determined coefficient. The dependence of ln (μ) on $E^{1/2}$ is of the Poole-Frenkel type. This describes the carrier detrapping from Coulomb traps by an applied field. The method of delayed pulsed EL enables measuring the mobility's electric field dependence up to relatively high fields of ~1MV/cm, while the TOF and dc transport measurements usually measure low field less than 0.3MV/cm.

Polaron and disorder models are used to explain the electric field dependence of the carrier mobility. The polaron model assumes the energetic disorder energy is small compared to the deformation energy, the localized carrier interacts strongly with molecular vibration of host and neighboring molecules, so significant relaxation of the local molecular structure occurs around the carrier. The carriers can hop to an adjacent

molecule only by carrying relaxation along with it. This relaxation or stabilization lowers the energy of the negative carrier below the LUMO and increases the energy of the positive carrier above the HOMO. In the disorder model, it assumes the coupling of a charge carrier to molecular modes is weak, and the activation energy reflects the static disorder of the hopping sites. The fundamental difference between the disorder and polaron models is related to the difference in energy of hopping sites, due to disorder and the change in molecular conformation upon addition or removal of a charge at a given site. The polaron model predicts mobility is a product of a Boltzmann probability of energy coincidence and the probability that a carrier will jump between adjacent sites by thermal activation, once energy coincidence occurs. The most widely accepted model is proposed by Emin:[63]

$$\mu \propto \frac{sinh\ (E/E_0)}{E/E_0}$$

But, it can only be used in a limited range.

Most recently, theories like Gaussian disorder models, based on the special correlation of energetic disorder, have been suggested. In the case of polymers, energetic disorder arises from the distribution of the conjugation length.

1.5.3 Carrier Recombination

When oppositely charged carriers are injected and transported into organic layers, they will recombine and release a considerable amount of energy in the form of light. A fraction of electron and hole current will recombine inside the organic layers and emit photons and phonons; the remaining fraction will recombine at the cathode and anode

with the energy released here converting into heat. By designing the device structure to balance the electron and hole currents, the recombination efficiency could be increased.

The initial recombination (IR) or geminate recombination (GR) - and volume-controlled recombination (VR) can be distinguished on the basis of the charge carrier's origin.[64] GR is the recombination process following the initial carrier separation from an unstable, locally-excited state, forming a nearest-neighbor charge transfer (CT) state. The electric field-induced luminescence quenching can be observed because external electric field-enhanced dissociation decreases the number of emitting states. In the OLED emission process, volume controlled recombination dominates, because electrons and holes are injected independently from the anode and cathode. The recombination process is kinetically bimolecular. The classic treatment of carrier recombination can be related to the notion of recombination time τ_{rec}. Recombination time depends upon the carrier motion time τ_m, which is the time to obtain the carriers within the capture radius and the elementary capture time τ_c.

$$\tau_{rec} = \frac{\tau_m \tau_c}{\tau_m + \tau_c}$$

If $\tau_m \gg \tau_c$, it is a Langevin-like volume recombination; if $\tau_m \ll \tau_c$, it is a Thomson-like volume recombination.[65] They also can be distinguished by comparison of the mean free path and the Coulombic capture radius. In organic materials, Langevin-like recombination is satisfied, in which random diffusive motion of charges dominates and drift can be viewed as a small bias in the time averaged displacement.

In the Langevin model, the electron and hole capture process is spin independent. Statistically, we could achieve 25% singlet excitons (S_1) and 75% triplet excitons (T_1):

$$4(e + h) \rightarrow S_1 + 3T_1$$

Therefore, the highest internal quantum efficiency of fluorescent based OLED, which only emits from the radiative decay of singlet excitons, is 25%.

At high carrier injection, triplet excitons can contribute to the EL mechanism via triplet-triplet annihilation:

$$4(T_1 + T_1) \rightarrow S_1 + 3T_1$$

At even higher carrier density, the carrier-induced and triplet-induced absorption take place.

1.6 OLED Device Efficiency and Optimization

Efficiency is the key issue for both energy consumption and the longevity of the devices. The ability to operate the device at a lower input power at a given luminance decreases the Ohmic heating and increases the device's lifetime. SMOLEDs behave very similar to inorganic semiconductor devices, but there are still two fundamental differences. First, all solid films made of small molecules useful for OLEDs are wide energy gap semiconductors. Vacuum sublimed films have extremely high resistivity on the order of $10^{15}\Omega\ cm$, and there are no free charges present in OLEDs without injection. So OLEDs are not under electrostatic equilibrium but rather under dynamic charge equilibrium when devices are in operation. Second, singlet and triplet excitons are produced by charge recombination, and emission is due to radiative transitions from the neutral excited states to the ground states. Although there is no experimental evidence on the radiative recombination of positive and negative charges in OLEDs, which typically occur in inorganic LEDs, the estimation of the EL quantum efficiencies becomes quite simple with these two basic assumptions.

Based upon the basic understanding of the working mechanism for charge injection type EL, the internal QE of the OLED can be written as

$$\eta_\phi = \gamma\beta\phi_f$$

This is defined as the ratio of the numbers of emitted photons within a device divided by the number of charges injected into a device. Here, γ is the charge balance factor, β is the production efficiency of emissive excitations, and ϕ_f is the fluorescence quantum yield.

The external quantum efficiency can be defined naturally from the internal QE:

$$\eta_\phi(ext) = \chi\eta_\phi$$

χ is the light output coupling factor. So, the external QE (EQE) is the ratio of the number of produced photons outside a device divided by the number of charges injected. From the definition of efficiency, EQE could be increased by designing the device to increase the charge balance factor, production efficiency, fluorescence quantum yield, and the output coupling factor.

The charge balance factor is defined by the ratio of the number of injected charges experimentally obtained from the measured current density J and the electron hole recombination current J_r

$$\gamma = \frac{J_r}{J}$$

If the number of holes injected into the device equals to the electrons injected, all holes and electrons are assumed to be consumed for recombination, then $J = J_r$ and $\gamma = 1$. To increase the charge balance factor, the holes and electrons also need to be confined within the device emissive region. By using the multilayer structures, charge

blocking layers can be introduced at the organic layers interfaces to improve the efficiency of the charge recombination and, in turn, the charge balance factor.[66,67]

Production efficiency of emissive excitation β is the branching ratio for singlets and triplets. Based upon simple spin statistics, assuming weak intermolecular interactions, the upper limit for the internal QE in OLEDs is 25%. Before the development of good phosphorescent emitters at room temperature, the design of highly fluorescent molecule with high fluorescence quantum yield has been one of the most important research targets. Although radiation from triplet states is "forbidden", some materials can emit efficiently from the TE state. Due to the existence of heavy metal atoms in these molecules, the spin and orbital coupling result in the mixing of singlet and triplets, so the radiative decay of triplet state is partly allowed. In a phosphorescent OLED, host SE and TE energy are transferred to the guest SE and TE states. Then, the guest SE intersystem crosses to the guest TE, and finally, the guest TE decays radiatively, resulting in the phosphorescence. So, theoretically, in phosphorescent materials, the production efficiency β could reach 100%.

Enhancing the out coupling factor, χ, is another efficient way to increase the device's efficiency. Simple ray optics model could be used to estimate the factor:

$$\chi = 1 - \sqrt{1 - \frac{1}{n^2}}$$

When n is larger than 1.6, the formula could be approximated by $(2n^2)^{-1}$. Organic materials' refractive indices are usually 1.7, and, thus, χ is frequently approximated by 20%. Such low out coupling efficiency leaves considerable opportunity for improvement. Substrate surface modification[68,69] can extract the glass mode light; whereas, wave guided

light out coupling methods include the use of sub-wavelength photonic crystals,[70] surface plasmons,[71] periodic dielectric mirrors,[72] very low index Aerogel layer,[73] and so on.

The power conversion efficiency is frequently expressed in the luminous power efficiency (lm/W). It includes the term of the human eye's sensitivity with its strong dependence on the emission wavelength. A better measure of the power efficiency may be given in terms of the electron to photon conversion efficiency (W/W) expressed by the ratio of the power of the emitted to the input electric power, and it can be expressed as follows:

$$\eta_E = \eta_\phi \frac{\varepsilon_p}{eV}$$

η_ϕ is the internal quantum efficiency, and ε_p is the average photon energy of the entire EL spectrum, V is the applied voltage. Thus, the improvement in the charge injection barrier at the anode and the cathode is effective for increasing the power efficiency through the decrease of the drive voltage.

Reference

[1]. **A. Bernanose, M. Comte, P. Vouaux.** J. Chem. Phys, Vol. 50, p. 64 (1953)

[2]. **A. Bernanose, P. Vouaux.** J. Chem. Phys, Vol. 50, p. 64 (1953)

[3]. **A.Bernanose, P. Vouaux.** J. Chem. Phys, Vol. 52, p. 396 (1955)

[4]. **A. Bernanose, P. Vouaux.** J. Chem. Phys, Vol. 52, p. 509 (1955)

[5]. **M. Pope, H. P. Kallmann, and P. Magnante.** J. Chem. Phys, Vol. 38, p. 2042 (1963)

[6]. **P. S. Vincett, W.A.Barlow and R. A. Hann, G. G. Roberts.** Thin Solid Films, Vol. 94, p. 171 (1982)

[7]. **Jyongsil Gu, Mitsuo Kawabe, Kohzoh Masuda, and Susumu Namba.** J. Appl. Phys, Vol. 50, p. 2493 (1977)

[8]. **C. W. Tang and S. A. VanSlyke.** Appl. Phys. Lett, Vol. 51, p. 913 (1987)

[9]. **Hideki Shirakawa, Edwin J. Louis, Alan G. MacDiarmid, Chwan K. Chiang and Alan J. Heeger.** J. Chem. Soc., Chem. Commun, p. 578 (1977)

[10]. **J. H. Burroughes, D. D. C. Bradley, A. R. Brown, R. N. Marks, K. Mackay, R. H. Friend, P. L. Burns, and A. B. Holmes.** Nature, Vol. 347, p. 539 (1990)

[11]. **Berend-Jan de Gans, Paul C. Duineveld, and Ulrich S. Schubert.** Adv. Mater, Vol. 3, p. 203 (2004)

[12]. **Baldo, M.A., et al.** Nature, Vol. 395, p. 154 (1998)

[13]. **Junji Kido, Masato Kimura and Katsutoshi Nagai.** Science, Vol. 267, p. 1332 (1995)

[14]. **Chihaya Adachi, Marc A. Baldo, Mark E. Thompson, and Stephen R. Forrest.** J. Appl. Phys, Vol. 90, p. 5048 (2001)

[15]. **J.Kido. San Diego, CA :** August 26-30, 2007, 2007 Organic Light-Emitting Materials and Devices XI SPIE Conf. 6655, SPIE Annual Meeting.

[16]. **J. Kido, T. Nakada, J. Endo, N. Kawamura, K. Mori, A. Yokoi, and T. Matsumoto.** Proceedings of the 11th International Workshop on Inorganic and Organic Electroluminescence and 2002 International Conference on the Science and Technology of Emissive Displays and Lighting, p. 539 (2002)

[17]. **T. Matsumoto, T. Nakada, J. Endo, K. Mori, N. Kavamura, A. Yokoi, and J. Kido.** 2003 Society for Information Display (SID) International Symposium, Digest of Technical Papers, p. 979 (2003)

[18]. **Chieh-Wei Chen, Yin-Jui Lu and Chung-Chih Wu, Elbert Hsing-En Wu, Chih-Wei Chu, and Yang Yang.** Appl. Phys. Lett, Vol. 87, p. 241121 (2005)

[19]. **Tae-Woo Lee, Taeyong Noh, Byoung-Ki Choi, Myeong-Suk Kim, and Dong Woo Shin, J. Kido.** Appl. Phys. Lett, Vol. 92, p. 043301 (2008)

[20]. **Mao-Kuo Wei, I-Ling Su, Yi-Jia Chen, Ming Chang, Hong-Yi Lin and Tung-Chuan Wu.** J. Micromech. Microeng, Vol. 16, p. 368 (2006)

[21]. **Wen-Kuei Huang, Wen-Sheng Wang, Hui-Chun Kan and Fang-Chung Chen.** Jpn. J. Appl. Phys, Vol. 45, p. L1100 (2006)

[22]. **T. Fujii, Y.Gao, R.Sharma, E.L. Hu, S.P. DenBaars, and S. Nakamura.** Appl.Phys.Lett, Vol. 84, pP.855-857 (2004)

[23]. **J. Q. Xi, H. Luo, A.J. Pasquale, J.K. Kim, and E.F. Schubert.** IEEE Photonics Technol. Lett, Vol. 18, pP.2347-2349 (2006)

[24]. **Y.-K. Ee, P. Kumnorkaew, R.A. Arif, H.Tong, J. F. gilchrist, and N. Tansu.** Opt. Express, Vol. 17, pP.13747-13754 (2009)

[25]. **Jongsun Lim, Seung Seok Oh, Doo Youp Kim.** Optical Express, Vol. 14, p. 14 (2006)

[26]. **Y. Sun, Stephen R. Forrest,** Nature Photonics, Vol. 2, pp. 483-487 (2008)

[27]. **Nils Reinke, Thomas Fuhrmann, Alexandra Perschke, Hilmar Franke.** J. Lumi, Vol. 110, p. 413 (2004)

[28]. **Yu Liu, Masayoshi Nishiura, Yue Wang, and Zhaomin Hou.** J. Am. Chem. Soc, Vol. 128, p. 5592 (2006)

[29]. **J. Kalinowski, M. Cocchi, G. Giro, V. Fattori, and P. Di Marco.** J. Phys. D, Vol. 34, p. 2282 (2001)

[30]. **T. Grandlund, L.A.A. Petterson, M. R. Anderson, and O. Inganas**. Vol. 81, p. 8097 (1997)

[31]. **Kafafi, Zakya H.** Organic Electroluminescence, p. 7 (2005)

[32]. **S. A. VanSlyke, et al.** Appl. Phys. Lett., Vol. 69, p. 2160 (1996)

[33]. **Tang, S. A. VanSlyke and C. W.** U. S. Patent 4, 720, 432.

[34]. **Y. Shirota, Y. Kuwabara, H. Inada, T. Wakimoto, H. Nakada, Y. Yonemoto, S. Kawami, and K. Imai.** Appl. Phys. Lett, Vol. 65, p. 807 (1994)

[35]. **Y. Hamada, T. Sano, M. Fujita, T. Fujii, Y. Nishio, and K. Shibata.** Jpn. J. Appl. Phys, Vol. 32, p. L514 (1993)

[36]. **P. E. Burrows, L. S. Sapochak, D. M. McCarty, S. R. Forrest, and M. E. Thompson.** Appl. Phys. Lett, Vol. 64, p. 2718 (1994)

[37]. **C. Adachi, T. Tsutsui, and S, Saito.** Appl. Phys. Lett, Vol. 56, p. 799 (1990)

[38]. **Y. Hamada, C. Adachi, T. Tsutsui, and S. Saito.** Jpn. J. Appl. Phys, Vol. 31, p. 1812 (1992)

[39]. **C. Hosokawa, H. Tokailin, H. Higashi, and T. Kusumoto.** J. Appl. Phys, Vol. 78, p. 5831 (1995)

[40]. **H. Spreitzer, H. Schenk, J. Salbeck, F. Weissoertel, H. Riel, and W. Reiss.** *"Organic Light Emitting Materials and Devices III"*, Edited by Z. H. Kafafi, Proc. SPIE 3797, 316.

[41]. **J. D. Anderson, E. M. McDonald, P. A. Lee, M. L. Anderson, E. L. Ritchie, H. K. Hall, T. Hopkins, E. A. Mash, J. Wang, A. Padias, S. Thayumanavan, S. Barlow, S. R. Marder, G. E. jabbour, S. Shaheen, B. Kippelen, N. Peyghambarian, R. M. Wightman, and N. R.** J. Am. Chem. Soc, Vol. 120, pp. 9646-9655 (1998)

[42]. **L. S. Sapochak, F. E. Benincasa, R. S. Schofield, J. L. Baker, K. K. C. Riccio, D. Fogarty, H. Kohlmann, K. F. Ferris, and P. E. Burrow.** J. Am. Chem. Soc, Vol. 124, pp. 6119-6125 (2002)

[43]. **C. H. Chen and J. Shi.** Coord. Chem. Rev, Vol. 171, pp. 161-174 (1998)

[44]. **McColgin, F. G. Webster and W. C.** U. S. Patent. 3,852,683 1974.

[45]. **C. Hosokawa, H. Higashi, H. Nakamura, and T. Kusumoto.** Appl. Phys. Lett, Vol. 67, pp. 3853-3855 (1995)

[46]. M. A. Baldo, s. Lamansky, P. E. Burrows, M. E. Thompson, and S. R. Forrest. Appl. Phys. Lett., Vol. 75, pp. 4-6 (1999)

[47]. **K. A. King, P. J. Spellane, and R. J. Watts.** J. Am. Chem. Soc, Vol. 107, pp. 1431-1432 (1985)

[48]. **TA Isberg, CA Jalbert, JS Staral, WA Tolbert, and MB Wolk.** December 7, 1999, Process for Preparing High Resolution Emissive Arrays and Corresponding Articles, U. S. Patent 5,998,085.

[49]. **Forrest, SR.** Chem. Rev, p. 1793 (1997)

[50]. **SA VanSlyke, A Pignato, D Freeman, N Redden, D Waters, H Kikuchi, T Negishi, H Kanno, Y Nishio, and M Nakai.** Linear Source Deposition of Organic Layers for Full-Color OLED,Proceedings of the Society for Information Display, Digest of Technical Papers, Vol. 33, p. 886 (2002)

[51]. **L.Zou, V. Savvate'ev, J.Booher, C. H. Kim, and J. Shinar.** Appl. Phys. Lett, Vol. 79, p. 2282 (2001)

[52]. **R. H. Friend, R. W. Gymer, A. B. Holmes, J. H. Burroughes, R. N. Marks, C. Taliani, D. D. C. Bradley, D. A. Dos Santos, J. L. Bredas, M. Logdlund, and W. R. Salaneck.** Nature, Vol. 397, p. 121 (1999)

[53]. **G. Gustafsson, y. Cao, G. M. Treacy, F. Klavetter, N. Colaneri, and A. J. Heeger.** Nature, Vol. 357, p. 447 (1992)

[54]. **Sergey Lamansky, Thomas R. Hoffend, Jr., Ha Le, Vivian Jones, Martin B. Wolk, and William A. Tolbert.** Organic Light-Emitting Materials and Devices IX , Proc. SPIE, Vol. 5937, p. 593702 (2005)

[55]. **Wolfgang Kowalsky, Torsten Benstem, Achim Bohler, Siegfried Dirr, Hans-Hermann Johannes, Dirk Metzdorf,, Helge Neuner, Jorg Schobel and Peter Urbach.** Phys. Chem. Chem. Phys, Vol. 1, p. 1719 (1999)

[56]. **S. M. Sze, Kwok K.Ng.** Physics of Semiconductor Devices (2007)

[57]. **Fowler, R.H. and Nordheim, L.** Proc. R. Soc., Vol. A119, p. 173 (1928)

[58]. **P. E Burrows, Z. Shen, V. Bulovic, D. M. McCarty, S. R. Forrest, J. A. Cronin, and M. E. Thompson.** J. Appl. Phys, Vol. 79, p. 7991 (1996)

[59]. **Kafafi, Zakya H.** Organic Electroluminescence, p. 71 (2005)

[60]. **Godlewski, J. and Kalinowsi, J.** Solid state commun., Vol. 25, p. 473 (1978)

[61]. **A. J. Pal, R. Osterbacka, K. M. Kallman, and H. Stubb.** Appl. Phys. Lett, Vol. 71, p. 228 (1997)

[62]. **S. Naka, H. Okada, H. Onnagawa, Y.Yamaguchi, and T. Tsutsui.** Synth. Met, Vols. 111-112, p. 331 (2000)

[63]. **Emin D.** Adv. Phys, Vol. 24, p9.305-348 (1975)

[64]. **Kalinowski, J.** Mol. Cryst. Liq. Cryst, Vol. 355, p. 231 (2001)

[65]. **Langevin, P.** Ann. Chem. Phys, Vol. 28, p. 289 (1903)

[66]. **J. C. Scott, S. Karg, and S. A. Carter.** J. Appl. Phys, Vol. 82, p. 1454 (1997)

[67]. **Ruhstaller, B.** J. Appl. Phys, Vol. 89, p. 4575 (2001)

[68]. **S. Moller, S. R. Forrest.** J. Appl. Phys, Vol. 91, pp. 3324-3327 (2002)

[69]. **Y. Sun, R. R. Forrest.** J. Appl. Phys, Vol. 100, p. 073106 (2006)

[70]. **Y. R. Do, Y. C. Kim, Y. W. Song, Y. H. Lee.** J. Appl. Phys, Vol. 96, pp. 7629-7636 (2004)

[71]. **J. Feng, T. Okamoto.** Opt. Lett, Vol. 30, pp. 2302-2304 (2005)

[72]. **M. Agrawal, Y. Sun, S. R. Forrest, P. Peumans.** Appl. Phys. Lett, Vol. 90, p. 241112 (2007)

[73]. **T. Tsutsui, M. Yahiro, H. Yokogawa, K. Kawano.** Adv. Mater, Vol. 13, pp. 1149-1152 (2001)

CHAPTER 2 INTRODUCTION TO ORGANIC SEMICONDUCTOR SOLID STATE LASERS

"Laser" is an acronym for Light Amplification by Stimulated Emission of Radiation. Laser light is usually spatially coherent and has an extremely narrow spectrum (monochromatic light). Albert Einstein laid the foundation for the invention of the laser in a ground breaking re-derivation of Max Planck's Law of Radiation, based on the concept of probability coefficients for absorption, spontaneous emission, and stimulated emission of electromagnetic radiation in his 1917s seminal paper. After 50 years of research, the first working laser was made by Theodore H. Maiman in 1960 at Hughes Research Laboratories. He used a solid state flashlamp-pumped synthetic ruby crystal to produce a red laser with a 694 nm wavelength.

There are many different types of lasers—gas laser, chemical laser, dye laser, metal-vapor laser, solid state laser, semiconductor laser, and some other types. Particularly, the semiconductor laser is the cornerstone of modern technology and science. Due to the wide spectral range of the semiconductor laser which extends from blue to infrared, its application ranges from element detection through telecommunication to entertainment. Since light emitting organic materials are also semiconductors, it is a natural step to introduce their inherent advantages into the laser field.

As an intrinsically "4-level" system, Polymers are outstanding laser materials. They have luminescence efficiencies higher than 60%, even in undiluted films. Their color spans the visible spectrum. Lasing from conjugated polymers has already been

demonstrated in MEH-PPV in 1993 by optical pumping. After this, optically-pumped lasing from many other organic materials are demonstrated. However, electrically-pumped lasing in organic materials has not been realized yet, due to different emissions and absorption mechanisms.

This chapter will thoroughly introduce the organic semiconductor laser's history, its principle, and its device structure.

2.1 History of Lasers and Organic Semiconductor Lasers

After the Einstein's Quantum Theory of Radiation, Rudolph W. Landenburg confirmed the existence of stimulated emission and negative absorption[1] in 1928. Valentin A. Fabrikant predicted the amplification of "short" waves by stimulated emission in 1939. In 1950, Alfred Kastler proposed a method of optical pumping to stimulate the gain media. Two years later, this method was experimentally confirmed by Brossel, Kastler, and Winter.[2] Stimulated emission was first realized in microwave rather than infrared or visible radiation. In 1953, the first microwave amplifier was produced by Charles H. Towens and co-workers[2]. It was called maser and only worked in a pulsed mode. Nikolay Basove and Aleksandr Prokhorove[2] produced a continuous output system by using more than two energy levels. This system could release stimulated emissions without falling to the ground state; thus, the population inversion could be maintained. In 1957, Charles Hard Townes and Arthur Leonard Schawlow began research with infrared lasers at Bell Labs. And, Gordon Gould[3] suggested using an open resonator in the device, which was important for future lasers. The term "Laser" was first introduced to the public in Gould's 1959 conference paper, "The LASER, Light Amplification by Stimulated

Emission of Radiation." Finally, the first working laser[4] was made by Theodore H. Maiman in 1960 at Hughes Research Laboratories in 1960.

The concept of the semiconductor laser diode was proposed by Basov and Javan, and demonstrated by Robert N. Hall in 1962.[5] The first laser diode was made of gallium arsenide and emitted at 850 nm in the near infrared region. The conjugated organic molecules in a host crystal were suggested as a laser media by Brock[6] in 1961. After this, numerous stimulated emissions in organic molecules/dyes or organic rare earth-based media were reported, including both singlet-[7] and triplet-based[8] emissions either in liquid or solid matrices. A cascade energy transfer from singlet to triplet of europium was also used. In 1967, B. H. Scoffer and B. B. McFarland reported solid and liquid organic dye lasers using diffraction gratings as cavity reflectors.[9] An alcoholic solution of rhodamine 6G was used as the laser material and efficient spectral narrowing was observed. Karl reported a tunable organic crystal laser in 1972, by using a 1kw nitrogen laser pumping anthracene contained in cleaved platelets of fluorine.[10] In 1974, Avanesjan optically-pumped anthracene crystals intensively, and found nonlinear fluorescence quenching due to exciton-exciton annihilation.

In 1992, the first conjugated polymer lasing was demonstrated by Moses, using a liquid dye laser configuration.[11] Poly[2-methoxy, 5-(2'ethyl-hexyloxy)-p-phenylenevinylene], MEH-PPV, was used instead of commonly used dye and was pumped by the second harmonic radiation of a Q-switched Nd:YAG laser. The first solid state lasing in conjugated polymers was demonstrated by Hide and co-workers.[12] The emission molecules were dispersed in a host matrix, and the stimulated emission was

enhanced by use of TiO2 nanoparticles.[13] Later, Tessler reported a conjugated polymer film-based microcavity laser,[14] the first organic laser based on materials that could support high current density.

More and more polymers are synthesized and reported as laser materials, as well as small molecules and single crystals. Various device configurations and structures are created to meet the requirements of the laser. The potential and advantage of organic material stimulated research to realize the electrically-pumped organic laser.

2.2 Principles of the Laser

In an atom, the energy state corresponds to the energy level of an electron with respect to the nucleus, usually found on the ground state. The absorption or emission of light can cause the transition of electrons from one energy state to another, and the frequency is related to the energy difference between the higher energy state E_2 and the lower energy state E_1 by Planck's equation:

$$hf = E_2 - E_1$$

where $h = 6.626 \times 10^{-34}\ Js$. The term "photon" has always been used to describe the discrete packets of energy released or absorbed by a system when there is an interaction between light and matter. Figure 2-1 shows a two-energy level system.[15] An electron, which initially locates at the lower energy state, may be excited to a higher energy state through the absorption of an incident photon. This process is called induced absorption as shown in Figure 2-1 (a). If an electron is initially at a higher energy level, it may jump back to the lower energy state as shown in Figure 2-1 (b), called spontaneous emission. The photons emitted from spontaneous emission have random phase and frequency.

Electron transitions from higher energy levels to lower energy levels can also be induced by an incident photon as shown in Figure 2-1 (c). This process is called stimulated emission. The emitted photons created by stimulated emission share the same frequency, phase, and polarization state with the incident photon. Thus, coherent radiation is achieved. This stimulated emission constitutes the basic condition for laser action. To create a coherent optical light and achieve significant contributions from stimulated rather than spontaneous emissions, the Boltzmann equilibrium must be disturbed in such a way the population of the upper laser transition state exceeds that of the lower state, called population inversion.

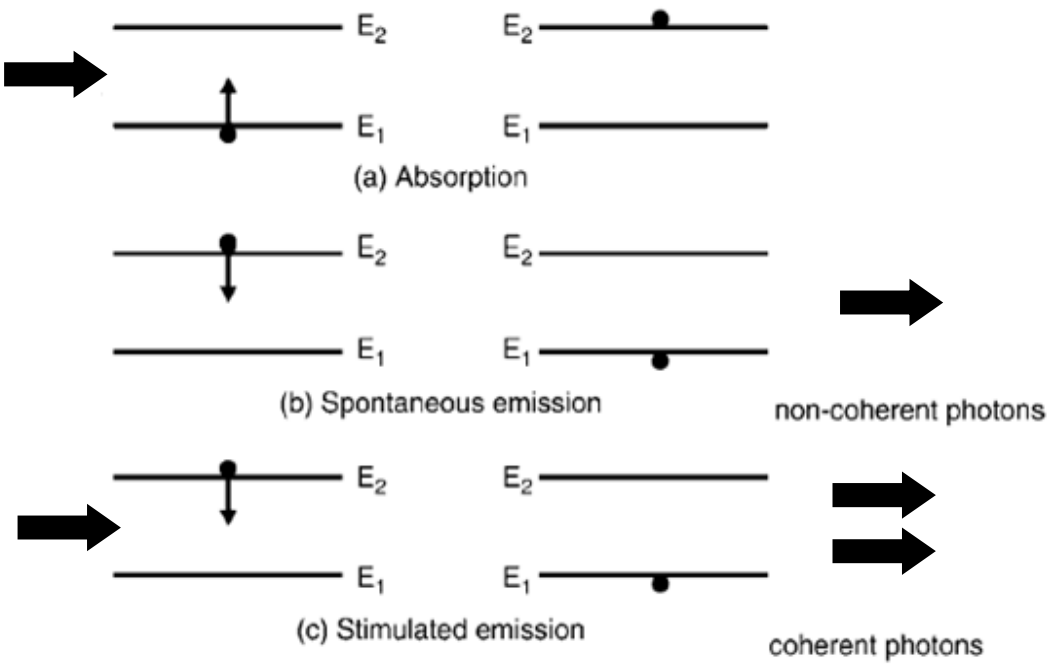

Figure 2-1 Different recombination mechanisms found in a two-energy level system

Let N_1 and N_2 be the electron populations in the lower and higher energy states of a two-level system. At thermal equilibrium, the population distribution is described by Boltzmann statistics:

$$\frac{N_2}{N_1} = e^{-(E_2-E_1)/kT}$$

And, if a uniform radiation is incident to this system, it is very easy to prove the upward and downward-induced transition rates are identical at thermal equilibrium. Therefore, the induced transition rate becomes:

$$W = \frac{A_{21}c^2}{8\pi n^2 h f^3} I$$

Here, A_{21} is the spontaneous transition rate, c is the speed of light, n is the refractive index, h is the Planck's constant, f is the light frequency, and I is the intensity of the optical wave.

Since the energy gain is associated with the downward transitions of electrons from a higher energy state to lower energy state, the net induced downward transition rate of the two-level system is $(N_2 - N_1)W$. And, without any dissipation mechanism, the power change per unit length should be:

$$\frac{dI}{dz} = (N_2 - N_1)\frac{A_{21}c^2}{8\pi n^2 f^2} I(z)$$

Thus, the general solution of the above first-order differential equation is:

$$I(z) = I_0 e^{\alpha(f)z}$$

where

$$\alpha(f) = (N_2 - N_1)\frac{A_{21}c^2}{8\pi n^2 f^2}$$

So only if $\alpha(f)$ is greater than zero, the incident wave will grow exponentially and there will be an amplification. The only method to achieve this condition is the number of electrons in a higher energy level is larger than those of the lower energy level. This shows the necessity of population inversion theoretically.

The two-level scheme is not generally feasible for laser action. The reason is the energy used to pump the particles into the upper state has an equal probability of stimulating them down. Thus, it is not possible to obtain more than half of the particles into the excited state. Figure 2-3 shows a three-level scheme. The gain media is first stimulated to an excited state higher than the upper laser state, and quickly decays into the upper laser state. It is important for the pumped state to have a short lifetime compared to the upper laser state. And, the upper laser state should have a long lifetime, long enough for the particles to be stimulated and contribute to gain.

Figure 2-2 shows a four-level scheme. The lower laser transition state is further depopulated by relaxation to the ground state, resulting in a higher population inversion and, therefore, in a more efficient stimulated amplification.

Besides the requirements of the laser material, most practical laser devices need a feedback loop called a laser cavity[16] shown in Figure 2-4. The gain medium is placed in a laser cavity, which has a mirror at either end. The mirrors are used to bounce the laser

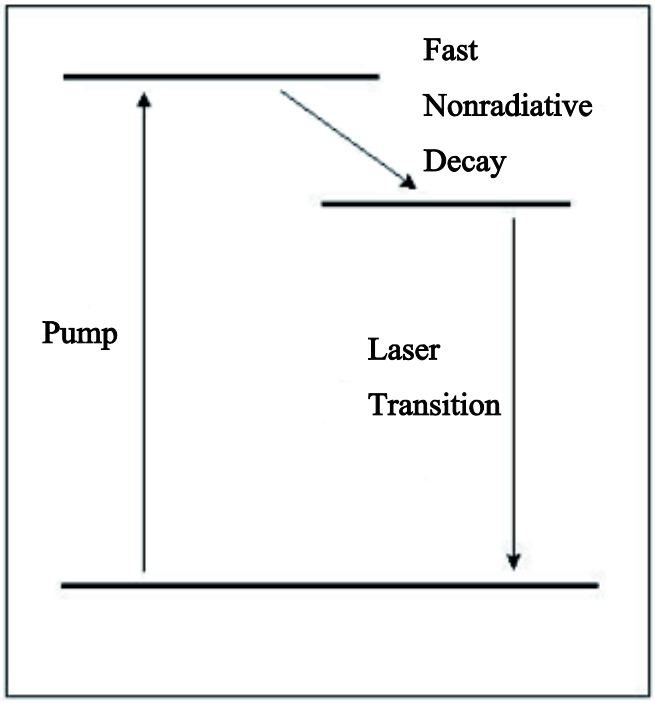

Figure 2-3 Three-Energy Level Scheme

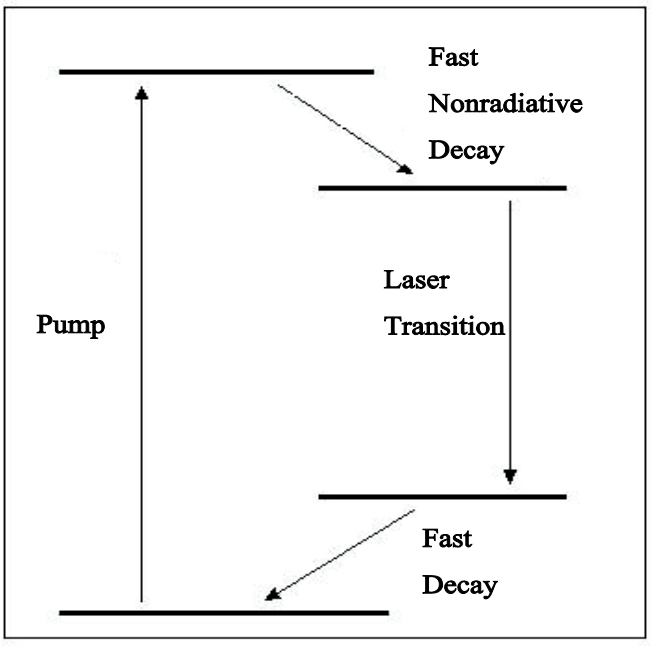

Figure 2-2 Four-Energy Level Scheme

Figure 2-4 Laser Oscillator Structure

light into the laser medium several times. The gain increases with each pass. One of the mirrors is partially reflecting, about 5% of the laser energy is transmitted to form the laser beam.

2.3 Lasing Characteristics and Experimental Determination

How to practically determine that a light is a laser? From a technological point of view, a definition derived directly from the acronym is insufficient. Therefore, laser should be associated with some stricter criteria:

i) spectrum is narrow and coincides with resonant cavity modes,

ii) spatial coherence,

iii) output light is strongly polarized, and

iv) a threshold above which a laser can be obtained.

The existence of threshold is one of the strongest evidences of laser. Different methods can be used to measure the threshold. The coherence of the light is another evidence, but is difficult to measure.

If the detector only collects the lasing mode when the laser is below threshold, the output power will show a kink at the threshold, since the lasing mode draws more power from the source at the expense of other modes. Thus, the existence of the kink in the output power versus input

power curve could be used as evidence of lasing. However, recently, micro-cavity lasers have high spontaneous emission coupling. There is no obvious threshold observed.[17]

Another strong evidence is that below the threshold, spontaneous emission is also emitted into modes other than the lasing modes; while above the threshold, the emission will show an abrupt spectral narrowing. So, the transition of spectrum from a broad spectrum to a narrow spectrum can be used as evidence for observing laser.

If the amplification gain of laser medium is homogeneously broadened, the laser above the threshold should only consist of a single mode;[18] while if it is inhomogeneously broadened, the laser will exhibit multimode operation. The pump and probe method is always used to measure the gain spectrum. By measuring and comparing the gain spectrum of different materials, the possibility of a material that could be used as a lasing medium can be determined.

If the feedback structure of the laser device contains a polarization-dependent element, the lasing should have well-defined polarization,[19] For example, a slab waveguide preferentially supports the transverse electric mode. Therefore, these laser devices with slab waveguides will emit lasing with TE polarization.

2.4 Laser Resonance Structure

As shown in Figure 2-4, a resonator structure is necessary for the laser device. Without the optical feedback structure, light still can be amplified when passing through the gain medium, but it is impossible to achieve a real laser. The resonator structure restricts the build-up laser oscillation to a few resonant modes. Conventionally, an external cavity with two end mirrors forms the resonator. On the route to an organic solid-state laser, alternative feedback structures have been proposed and proven.

2.4.1 The microcavity

Microcavity devices consist of a luminescent material placed within a Fabry-Perot resonator with a length of the order of the wavelength of emitting light. This design provides a possibility for a compact device structure. In this way, light is coupled to the cavity mode, and the output light is spectrally narrowed and directional.[20]

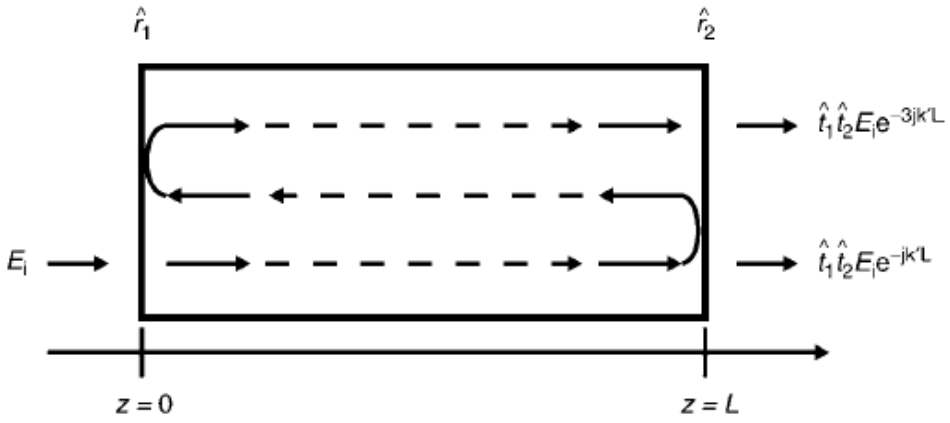

Figure 2-5 A simple Fabry-Perot structure

Figure 2-5 shows a simple Fabry-Perot structure. As an electric field bounces back and forth between the partially reflected mirrors, the wave is amplified as it passes through the laser medium. $\hat{r}_1$ and $\hat{r}_2$ are reflection coefficients of the mirrors; $\hat{t}_1$ and $\hat{t}_2$ are transmission coefficients of the mirrors. The length of the cavity is L, if the complex propagation constant of the incident wave is k'. After a series of reflections, the total transmitted wave becomes:

$$E_{out} = E_{in}\hat{t}_1\hat{t}_2e^{-jk'L}[1 + \hat{r}_1\hat{r}_2e^{-2jk'L} + \hat{r}_1^2\hat{r}_2^2e^{-4jk'L} + \cdots] ..$$

Infinite sum of the above equation will give:

$$E_{out} = \frac{\hat{t}_1\hat{t}_2e^{-jk'L}}{1 - \hat{r}_1\hat{r}_2e^{-2jk'L}}\ E_{in}$$

To obtain the self sustained oscillation, the denomination should be zero:

$$\hat{r}_1\hat{r}_2 e^{-2jk'L} = 1$$

This is the threshold condition for a Fabry-Perot laser, and the phase change after a round-trip must be an integer multiple of 2π to maintain a constructive phase interference. Theoretically, an infinite number of longitudinal modes can be supported by the cavity. Practically, it also depends on the width of the material gain spectrum. The mode having minimum threshold gain becomes the lasing mode, while others become non-lasing modes.

2.4.2 Distributed Bragg reflectors

A Distributed Bragg Reflector (DBR) laser is where its resonator is made with at least one distributed Bragg reflector outside the gain medium. A DBR is a quarter-wave mirror consisting of a stack of alternating layers of high and low refractive indices, resulting in high reflectivity over a broad spectral range. The thickness of the stacks of layers can be controlled to select several discrete modes or even a single mode.

The reflectivity (R) of the DBR is given by

$$R = \left[\frac{n_0(n_2)^{2N} - n_s(n_1)^{2N}}{n_0(n_2)^{2N} + n_s(n_1)^{2N}}\right]^2$$

where $n_0, n_1, n_{2,}$ and n_s are the refractive indices of the surrounding medium, two alternating materials, and the substrate. N is the number of the repeated sections of low/high refractive indices.. Consider only pure DBR without the substrate and the surrounding medium, air, the number of repeated layers needed to achieve a certain reflection is

$$N > \frac{ln\,(\frac{1+\sqrt{R}}{1-\sqrt{R}})}{2\,ln\,(\frac{n_2}{n_1})}$$

The band width of the DBR can be expressed as follows:

$$\Delta v_0 = \frac{4v_0}{\pi}\ arcsin\ (\frac{n_2 - n_1}{n_2 + n_1})$$

where v_0 is the central frequency of the band. From the equations above, increasing the number of repeated pairs in DBR increases the reflectivity; increasing the refractive index contrast of the alternative layers increases both refractivity and bandwidth.

Due to the advantages of DBR, it can be used as a mirror in the micro-cavity laser structure, such as vertical cavity surface emitting lasers (Figure 2-6). It is also very attractive for in-plane laser configurations (shown in Figure 2-7) for single axial mode operation.

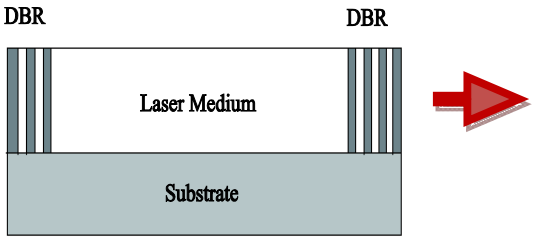

Figure 2-6 in-plane laser configuration

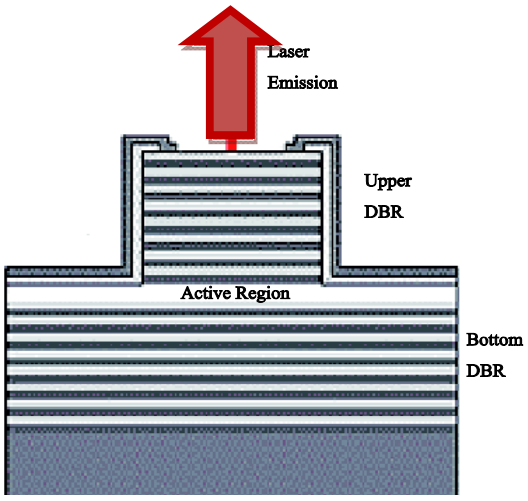

Figure 2-7 Vertical Cavity surface emitting laser

2.4.3 Slab waveguide structures

A planar waveguide consists of thin layers of optically transparent media, with a high refractive index core layer and low refractive cladding layers (shown in Figure 2-8, where n_f is larger than both n_{air} and n_s). This structure can confine part of the light in the core layer and guide certain modes of light.

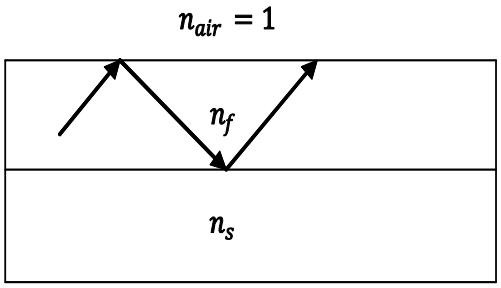

Figure 2-8 Asymmetric Slab Waveguide Structure

In the wave guiding structure, light is channeled via a series of total internal reflections between the boundaries of different refractive index media. The probability for stimulated processes can be enhanced by this light confinement and an increase of the effective interaction length. The slab waveguide structure can support transverse electric mode (TE) and transverse magnetic mode (TM). Only those lights, which satisfy constructive interference conditions, can exist and propagate in the structure. The total number of modes depends not only on the refractive indices, but also on the thickness of the waveguide region.

For a wave guided light of wavelength λ in an asymmetric structure, the thickness of the core layer must be larger than a critical thickness l_{crit} :[21]

$$l_{crit} = \frac{\lambda}{2\pi(n_f^2 - n_s^2)} \arctan\left(\frac{n_s^2 - 1}{n_f^2 - n_s^2}\right)^{1/2}$$

Otherwise, the light of wavelength λ cannot propagate in the waveguide structure. Here, $n_f, and\ n_s$ are refractive indices of film and substrate, respectively. And, if the thickness of the film is d_f , the cutoff wavelength is:

$$\lambda = \frac{2\pi(n_f^2 - n_s^2)d_f}{\arctan\left(\frac{n_s^2 - 1}{n_f^2 - n_s^2}\right)^{1/2}}$$

The first reported waveguide laser had a cylindrical geometry known as a fiber laser.[22] The primary motivation today is to reduce the cavity mode volume through optical confinement in the active host, thus exploiting the high gain and low threshold.

Waveguide lasers can be integrated with other optical elements on the same device, such as optical modulators for Q switching, active mode locking, or wavelength tuning. A waveguide laser may even be part of a complex photonic integrated circuit.

2.4.4 Distributed feedback structures

In principle, to obtain resonant oscillation, there is no need to separate the region of gain and reflection as shown in Figure 2-7. Figure 2-9 indicates schematically the concept of a

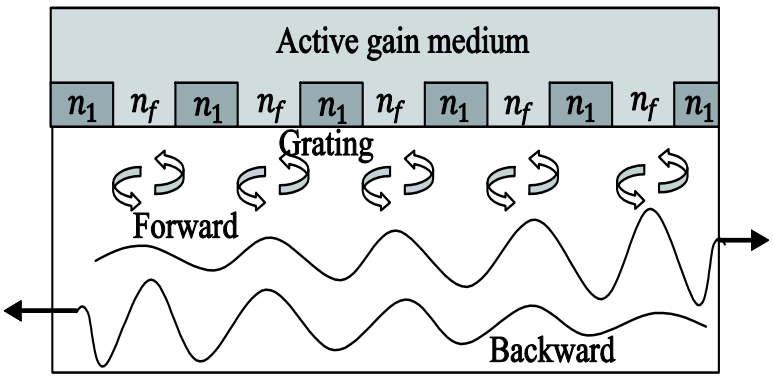

Figure 2-9 DFB Structure

uniformly- distributed feedback structure, with distributed reflections and gain within the cavity.

An optical wave travelling in one direction is continuously scattered into the optical wave in the reverse direction. Both waves grow as they travel towards their respective facets because of feedback and gain.

The feedback is strongly frequency selective and the resonant mode for laser oscillation corresponds to the wavelength that satisfies the Bragg condition:

$$m\lambda = 2n_{eff}\Lambda$$

Here, m is the integer diffraction order, λ is the free space Bragg wavelength, n_{eff} is the mean value of the refractive index of the guide, and Λ is the period of the DFB structure. The lowest order (m=1) is the more efficient condition to provide optical feedback, but it is difficult to fabricate the high resolution periodic feedback structure. Thus, high order DFB attracts interest, since the reduced spatial resolution, and could be used for laser operation.[23] Emission directions are different for different diffraction orders. The first order light resonates and emits in the plane, while for higher orders, the light will emit from the surface.

The imprinting technique with UV curing is utilized to make a feedback structure. And, the printing and molding techniques[24, 25] are very attractive for making organic DFB, as well as for organic DBR lasers.

2.4.5 Whispering-gallery-mode laser

Apart from other resonant structures, the whispering gallery mode laser has a special spherical design of microstructure resonators. It can be implemented for compact miniature laser devices. Whispering gallery mode (WGM) oscillations from micro-ring cavities have the advantage that high Q values are easily obtained in a very small mode volume and the number of modes contributing to laser oscillations can be reduced. The waves are totally reflected and

focused by the surface. Due to minimal reflection losses, these modes can reach extremely high quality factor.

Whispering gallery mode resonances correspond to light trapped in circular orbits just within the surface of the structure as shown in Figure 2-10. The modes are most strongly coupled along the equatorial plane and can be thought to propagate along zig-zag paths around the sphere. Whispering gallery modes occur at discrete frequencies that depend on the index of refraction n_s and radius R_0 of the sphere.

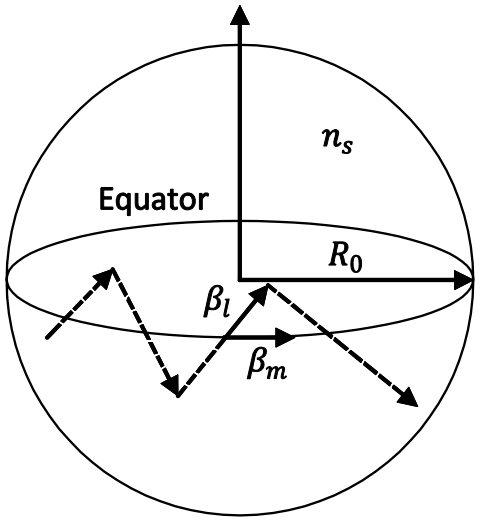

Figure 2-10 Whispering Gallery Structure

Each mode has propagation constant β_l parallel to the surface and in the direction of the zig-zag path. The propagation constant has a value:

$$\beta_l = \sqrt{\frac{l(l+1)}{R_0}}$$

At the same time, the projection of the propagation constant β_m has the value:

$$\beta_m = \frac{m}{R_0}$$

Here, l and m are both integers, so only those modes with discrete frequencies are allowed in the sphere resonance structure.

In fact, a spherical structure is a particular case. Whispering gallery mode lasers can also be fabricated as rings, discs with characteristic dimensions of 1~100 μm. Laser action will occur along these circumferences when the gain exceeds the round trip loss. It was first realized for thin III-IV semiconductors,[26] and also was demonstrated in dye-doped polymers,[27] dye solution droplets,[28] and conjugated polymers.[29]

2.5 Optical Gain Measurement Methods

Optical gain plays a critical role in evaluating the potential of a given semiconducting material. Positive gain predicates the amplification of light, and negative gain means loss or attenuation of light. The occurrence of positive gain is a necessary condition for realization of laser diodes. Thus, a simple and reliable experimental method to measure the presence or absence, and magnitude of gain is highly desired.

In semiconductor optical gain measurements, there are two main methods—pump and probe method, and variable stripe length method. They are also used to measure organic semiconductor gain.

2.5.1 Pump and probe measurement

Optical gain is defined as negative absorption; the most straightforward technique to measure gain is to detect absorption changes when pumping a sample above the threshold. The pump and probe technique consists of a strong pumping beam exciting a sample and a weak probe beam detecting signals shown in Figure 2-11. In other words, it measures the differential transmission spectrum (probe) generated by photo excitation (pump). Furthermore, because the pump and probe beams are from different light sources, in the transient measurement the probe pulse can be

temporally delayed by a delay time. Hence, the excited state population can be monitored for different delays tracing the spectral and temporal evolution of the photo induced species.

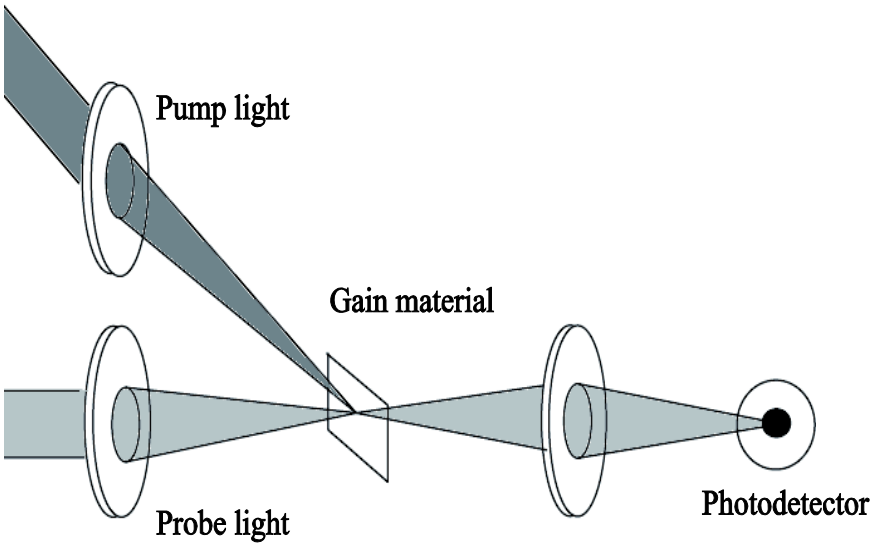

Figure 2-11 Pump and Probe experiment schematic diagram

A change of the transmission signal $(T_{pump-on} - T_{pump-off})/T_{pump-off} = \Delta T/T$ can be obtained from the pump and probe experiment. Frequently, this transmission signal is negative because the photo-induced states created by the pump pulse can absorb probe photons by transition to optically-allowed higher energy states (photo induced absorption PIA), one of the most important losses in lasers. On the contrary, a positive change of the transmission signal can be obtained, due to stimulated emissions.

The pump and probe measurement can monitor the singlet population via stimulated emission (SE) for both the regime below (spontaneous emission) and above the threshold (ASE). PIA is always in competition with SE. In a real laser, the peak emitting wavelength of the narrowing spectrum is confined close to the maximum of the gain profile to have maximum amplification.

2.5.2 Variable stripe length method

The variable stripe length (VSL) method was broadly used in measuring semiconductor gain coefficients. VSL was first proposed by Kerry L. Shaklee and co-workers from Bell Labs in 1971.[30, 31] This method is based on exciting a semiconductor sample with a laser beam focused into a narrow stripe by a cylindrical lens. The length of the pumped line can vary by a shutter and the light output intensity is measured as a function of the stripe length, *l*.

Figure 2-12 shows the VSL experiment set up schematic diagram. Photoluminescence is excited by a laser beam focused into a narrow line—typically $10\mu m \times 100\mu m$. To focus the laser beam into a stripe, a laser source similar to either excimer or N_2 laser possessing a rectangular beam cross-section is used, and a cylindrical lens is indispensible.[32] The emitted narrow beam after the cylindrical lens is not ready to be projected onto the sample. Usually, another spherical lens is used to image the stripe light beam onto the test sample. An adjustable slit is located in the focal plane of the cylindrical lens by means of the length of the stripe beam can be varied. A photo detector is placed near the edge of the test sample to collect the emitting light.

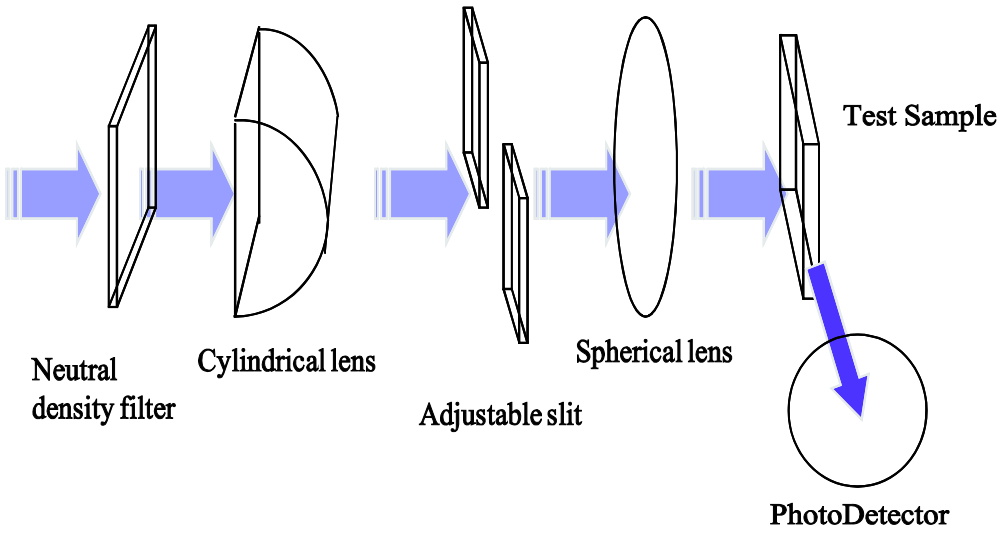

Figure 2-12 Variable Stripe Length Schematic diagram

An alternative method is exciting the sample through a fixed metal slit only $20-50\mu m$ above the test sample film. The stripe length is varied by moving a metal foil over the slit with the aid of a micro-stepping motor. This arrangement ensures the constant position of the excitation spot on the sample surface, negligible influence of light diffraction, and perfect control of the experiment geometry.[33]

Consider the stripe as a one-dimensional structure along the x-axis and population inversion is reached. The excited part of the sample acts as a single pass amplifier for any photons passing through the stripe. The net gain G is defined as a relative change of light intensity passing an infinitesimal distance dx:

$$G = \frac{dI(x,\lambda)}{dx}\frac{1}{I(x,\lambda)}$$

The total change of the detected intensity is a sum of a gain magnification of the incoming light and spontaneous emission from that infinitesimal segment:

$$dI_{out}(x,\lambda) = G(\lambda)I_{out}(x,\lambda)dx + I_{sp}(\lambda)dx$$

Solving this differential equation, we calculate the classical VSL equation:

$$I_{out}(l,\lambda) = \frac{I_{sp}(\lambda)}{G(\lambda)}(e^{-G(\lambda)l} - 1)$$

This enables us to measure the net gain from the output intensity versus stripe length curve.

Here, the VSL method in optical pumping is discussed, and the gain coefficient in electrical pumping is more interesting. Because of the injection of the charges, there are more loss channels appearing in the device. The net gain will change significantly. Thus, a VSL method in electrical pumping is invented, as will be discussed later.

2.6 Advantage of Organic Laser Materials

Photo excited solid state organic lasers have been made with a variety of gain media, including dye-doped polymers,[34, 35] dye-doped molecular single crystals,[10] diluted conjugated polymers,[36] neat films of conjugated polymers and molecular solids.[12, 14]

Organic materials and polymer laser gain media with Forster transfer can result in very low threshold power densities for both ASE and real lasing.[37, 38] One of the most important reasons is a very low optical loss at the emission wavelength, due to the large Stokes shift of the emission spectrum from absorption of the material.

The basic mechanism of laser action in organic molecules is almost the same as we mentioned in Sec 2.2.

Figure 2-13 shows the schematic diagram of the energy level of organic materials. The molecule is excited from the ground state to the first singlet excited state (S_1). Both the ground state and the first excited state consist of many levels, due to the vibronic and rotational degree of freedom that a molecule possesses. The internal relaxation from a higher level of excited state to the lowest level excited state is very rapid, less than 1ns. The energy level of organic molecules can be approximated as a four-level system. In laser action, the molecule is excited from the E1 level to the E4 level and then quickly relaxed to the E3 level. The laser transition is between levels E3 and E2.

Therefore, energy level materials, organic materials, and polymers are good candidates for laser gain medium. They integrate with resonance structures to emit actual laser by optical pumping. Electrically-pumped lasers are different from optically-pumped lasers. Especially in organic materials, there are more losses appearing when charges are injected into the devices. And, the electrically-pumped organic laser is still not realized.

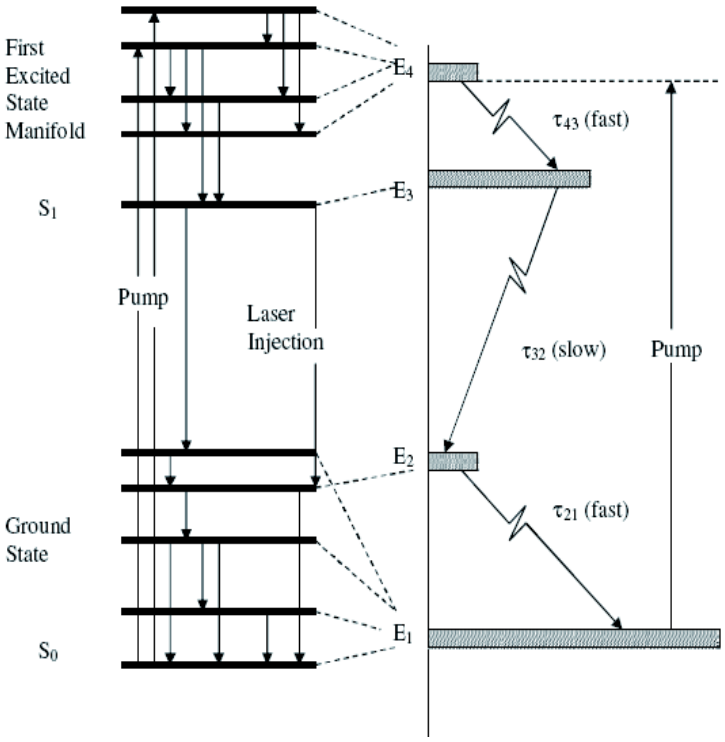

Figure 2-13 Organic molecule or polymer energy level and energy transfer

Reference

[1]. **Steen, W. M**. *"Laser Materials Processing", 2nd Ed.* (1998).

2**. Taylor, Nick.** *"LASER: The inventor, the Nobel laureate, and the thirty-year patent war"* p.56, (2000)

3. **Taylor, Nick.** *"LASER: The inventor, the Nobel laureate, and the thirty-year patent war"* pp. 66-70, (2000)

4. **Maiman. T.H.** Nature, Vol. 187, pp. 493-494 (1960)

5. **Hall, Robert N, G. E. Fenner, J.D. Kingsley, T.J. Soltys, and R. O. Carlson.** Phys. Rev. Lett, Vol. 9, pp.366-369 (1962)

6. **E. G. Brock, P. Csavinszky, E. Hormats, H. C. Nedderman, D. Stirpe, F. Unterleitner.** J. Chem. Phys, Vol. 35, p.759 (1961)

7. **A. Lempicki, H. Samelson**. Appl. Phys. Lett, Vol. 2, p.159 (1963)

8. **D. J. Morantz, B. G. White, A. J. C. Wright.** J. Chem. Phys, Vol. 37, p.2041 (1962)

9. **B. H. Soffer, B. B. McFarland.** Appl. Phys. Lett, Vol. 10, p.266 (1967)

10. **Karl, N.** Phys. Status Solidi part(a), Vol. 13, pp. 651-655 (1972)

11. **Moses, D.** Appl. Phys. Lett, Vol. 60, p. 3215 (1992)

12. **Fumitomo Hide, Maria A. Diaz-Garcia, Benjamin J. Schwartz, Mats R. Andersson, Qibing Pei, Alan J. Heeger.** Scince, Vol. 273, p. 1833 (1996)

13. **R. M. Balachandran, N. M. Lawandy, J. A. Moon.** Opt. Lett, Vol. 22, p. 319 (1997)

14. **N. Tessler, G. J. Denton, R. H. Friend.** Nature, Vol. 382, p. 695 (1996)

15. **Dr. H. Ghafouri-Shiraz.** *"Distributed Feedback Laser Diodes and Optical Tunable Filter*", p. 33 (2003)

16. **Tessler, Nir.** Adv. Mater., Vol. 11, p. 363 (1999)

17. **Y. Yamamoto, A. Machida, G. Bjork.** Opt. Quantum Electron, Vol. 24, p. S215 (1992)

18. **A. Yariv.** Optical Electronics. New York : CBS College Publishing, (1989)

19. **B. E. A. Saleh, M. C. Teich.** Fundamentals of Photonics. New York : Wiley, (1991)

20. **T. Tsutsui, N. Takada, and S. Saito.** Appl. Phys. Lett, Vol. 65, p. 1869 (1994)

21. **H. Kogelnik, I. T. Tamir. Berlin : Springer,** Integrated Optics, Topic in Applied Physics, Vol. 7. (1979)

22. **Snitzer, E.** Phys. Rev. Lett, Vol. 7, p. 444 (1961)

23. **J. E. Bjorkholm and C. V. Shank.** Appl. Phys. Lett, Vol. 20, p. 306 (1972)

24. **J. A. Rogers, M. Meier and A. Dodabalapur.** Appl. Phys. Lett, Vol. 73, p. 1766 (1998)

25. **M. Berggren, A. Dodabalapur, R. E. Slusher, A. Timko and O. Naalamasu.** Appl. Phys. Lett, Vol. 72, p. 410 (1998)

26. **S. L. McCall, A. F. J. Levi, R. E. Slusher, S. J. Pearton and R. A. Logan.** Appl. Phys. Lett, Vol. 60, p. 289 (1992)

27. **H. P. Weber and R.Ulrich.** Appl. Phys. Lett, Vol. 19, p. 38 (1971)

28. **M. Berggren, A. Dodabalapur, Bao Z and R. E. Slusher.** Adv. Mater, Vol. 9, p. 968 (1997)

29. **S. V. Frolov, M. Shkunov, Z. V. Vardeny and K. Yoshino.** Phys. Rev. B, Vol. 56, p. 56 (1997)

30. **K. L. Shaklee, and R. F. Leheny.** Appl. Phys. Letter, Vol. 18, pp. 475-477 (1971)

31. **R. Dingle, K. L. Shaklee, R. F. Leheny, and R. B. Zetterstrom.** Appl. Phys. Lett, Vol. 19, pp. 5-7 (1971)

32. **K. L. Shaklee, R. E. Nahory, and R. F.** J. Luminescence, Vol. 7, pp. 284-309 (1973)

33. **L. Pavesi.** *"Towards the First Silicon Laser."* Netherlands : Kluwer Academic Publishers, pp. 223-242 (2003)

34. **McFarland, B. H. Soffer and B. B.** Appl. Phys. Lett, Vol. 10, pp. 266-267 (1967)

35. **Shank, H. Kogelnik and C. V.** Appl. Phys. Lett, Vol. 18, pp. 152-154 (1971)

36. **F. Hide, B. J. Schwartz, M. A. Diaz-Garcia, and A. J. Heeger**. Chem. Phys. Lett, Vol. 256, pp. 424-430 (1996)

37. **M. Berggren, A. Dodabalapur, R. E. Slusher, and Z. Bao.** Nature, Vol. 389, pp. 466-469 (1997)

38. **M. Berggren, A. Dodabalapur, and R. E. Slusher.** Appl. Phys. Lett, Vol. 71, pp. 2230-2232 (1997)

CHAPTER 3 EIGHT SOURCES EVAPORATION SYSTEM DESIGN

Organic Light Emitting Diode (OLED) as a new display technology experienced a rapid development pace recently. More and more products appear in the market, and not only the quality but also the lifetime of these OLED devices has greatly increased. New organic materials were synthesized, new structures were developed, and new encapsulation methods were adopted.

The driving force behind this fast development is the advantages of the OLED:

- Low power consumption—because the efficiency of the OLEDs is basically high, especially for phosphorescent OLEDs, the internal quantum efficiency can achieve 100%.
- Faster refresh rate—because the OLED EL decay-time is less than 1 μs; for these fluorescent OLEDs, the excition lifetime is typically ≤ 10 ns.
- Better contrast—because OLED is a self-luminous device, there is no need for backlight and polarizer as other LCD displays. Like the Sony OLED TV XEL-1 commercialized in 2007, the contrast ratio is 1,000,000:1.
- Great brightness—because OLED is a thin device, at low operating voltages brightness can achieve thousands or even tens of thousands cd/m^2.
- Lighter weight—without the necessity of a backlight as needed for LCD devices, OLED devices can be much lighter.
- Wide viewing angle—OLED emission is lambartian, thus the viewing angle is as high as 160 degrees.
- Flexibility—as a type of thin film organic device, it can be fabricated on any flexible plastic substrate.

- Low cost and easy fabrication—as mentioned in Chapter 1, many fabrication methods are used in OLED production, especially roll-to-roll and inkjet printing, possible for polymer OLEDs and interest shown by the industry.

Although it appears trivial to fabricate OLED, actually, there are many details that need consideration. One component is OLED fabrication entails depositing layers of thin films; but in addition, other components include thickness must be monitored, substrate's temperature must be carefully considered, contamination must be eliminated, and concentration must be controlled.

In the academic field, most of the labs use the thermal evaporation method to fabricate OLED devices for research. Thus, a vacuum chamber is the base of the OLED fabrication system, with the heating element at the bottom of the chamber and substrate holder at the top. Of course, a powerful vacuum pump is connected to the chamber to maintain the chamber's vacuum around$10^{-7}\ torr$.

Our laboratory has a thermal evaporation system, with two heating elements located on the bottom of the chamber and a substrate holder on the top. With a sliding shutter, a combinatorial fabrication can be operated. The system is installed in an Argon-filled glove box.

Advantages of this system include:

- Two heating elements—two materials can be evaporated and deposited in series without breaking the vacuum; two materials co-deposition can be achieved.
- Thickness monitor—the thickness of the thin film deposited can be monitored in real time.
- Sliding shutter—1D combinatorial fabrication can be achieved; 2D combinatorial fabrication can be operated by breaking the vacuum.

- Installed in a glove box filled with Argon—reduces air contamination, particularly oxygen and water.

Disadvantages of this system include:

- Two heating elements—for OLED devices, typically, there are four layers of thin film, including hole injection layer, hole transport layer, electron transport layer, and metal cathode. Thus, the vacuum must be broken after depositing two layers.
- One shutter to cover the heating elements—opening or closing the shutter can control deposition or stop deposition. When evaporating one material, the vapor of this material could deposit on the surface of another material and contamination can occur.
- Pole holds the thickness monitor—when such a pole exists in the evaporation chamber, the evaporated molecules are adsorbed on the surface of the pole or bounce back. Thus, the distribution of the molecules in the chamber is more difficult to predict and the film deposited on the substrate is no longer uniform.
- No heat insulator between heating elements—without heat insulators, when depositing one material, the second material will become heated at the same time, due to the radiation heat. This a hidden source of contamination.
- One-dimensional sliding shutter—for optimization of OLEDs, thickness of organic thin film layers is changed to find the optimized structure by comparing OLEDs in one batch with a different structure. However, for two-dimensional fabrications, the vacuum must be broken once.
- Back fill—the back fill valve is installed near the turbo pump. However, it may introduce turbo oil into the chamber with back flow and contaminate the device.

Since the deposition system is one of the keys to fabricate high quality OLEDs, it is necessary to have an excellent evaporation chamber with finely designed features. Thus, an Eight Source Evaporation System shown in Figure 3-1 is designed to meet this demand.

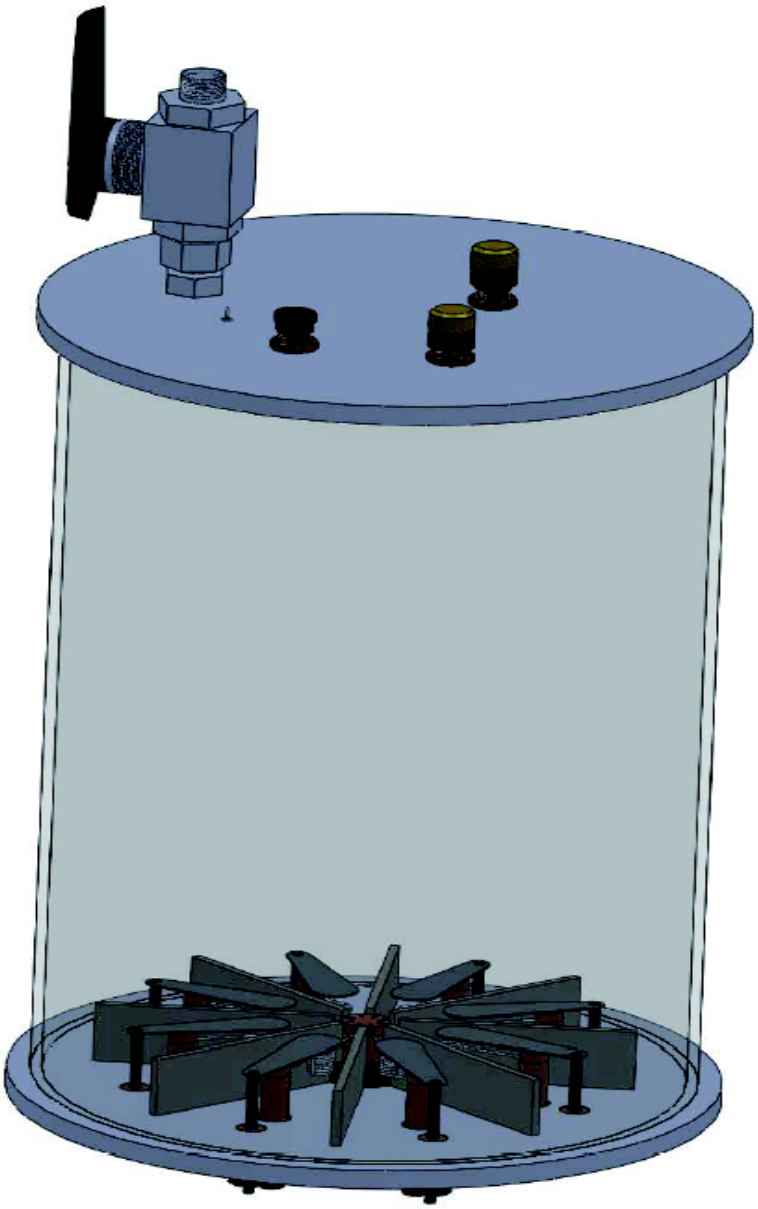

Figure 3-1 Eight Source Evaporation System

3.1 Bottom Plate Design

Eight-Source Evaporation System, as the name suggests, is a system with eight sources. Thus, the first request is eight sources should be located on the bottom of the system. Typically for a more complicated OLED structure, there are around 8 thin film layers—hole injection layer, hole transport layer, electron blocking layer, emission layer, hole blocking layer, electron transport layer, electron injection layer, and metal cathode. So, with eight sources, there is no need to break the vacuum during the entire process when fabricating OLEDs.

Figure 3-2 shows the bottom plate of the eight-source evaporation system. In the center of the plate, there is a common cathode with eight grooves on the top used for installing heating coils. Around this center cathode, eight anodes are arranged uniformly in a circle. Then, the eight heating coils can connect to the common cathode and individual anode. They are distributed uniformly around the center and as far away as possible to reduce interference between the heating elements.

Considering the radiation heat of the operational coil, which is usually higher than several hundred degrees Celsius, heat insulating walls are inserted between each source. These insulating walls cannot only prevent side heating effects, but it also help reduce material contamination. With this blocking wall, the material in one source is not able to transport to the nearest sources; thus, contamination is prevented as shown in Figure 3-3.

For each heating source, there is an individual small shutter covering the top. Each shutter can be opened and closed individually. From Figure 3-3, we can see eight knobs located in the backside of the bottom plate connect to the shutters, and Swageloks are used to seal the feedthrough. These small shutters can thoroughly prevent contamination when depositing organic materials. he shutter is open only for the source, which is in use for evaporating material,

otherwise, it always keeps closed. Figure 3-4 shows the view of the bottom plate from different directions.

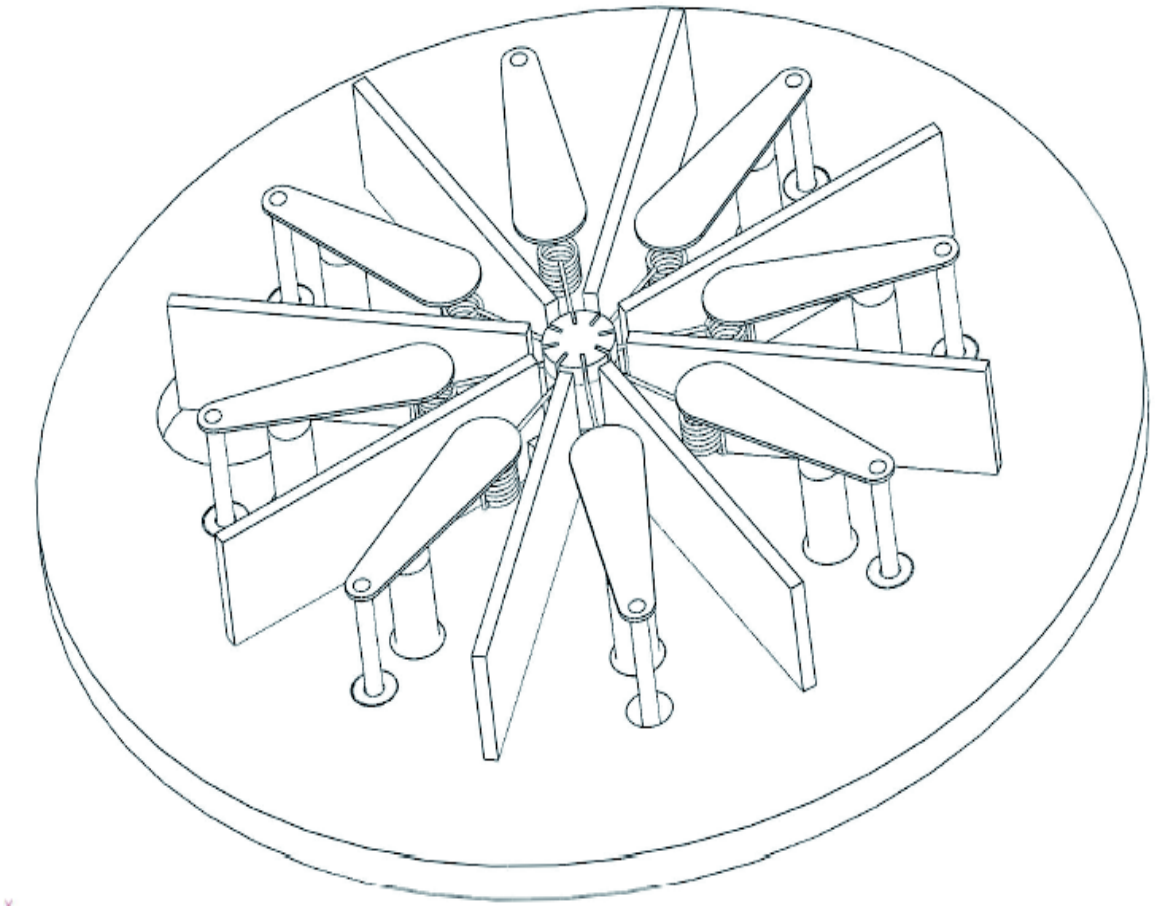

Figure 3-2 the bottom plate of the Eight Sources Evaporation Chamber

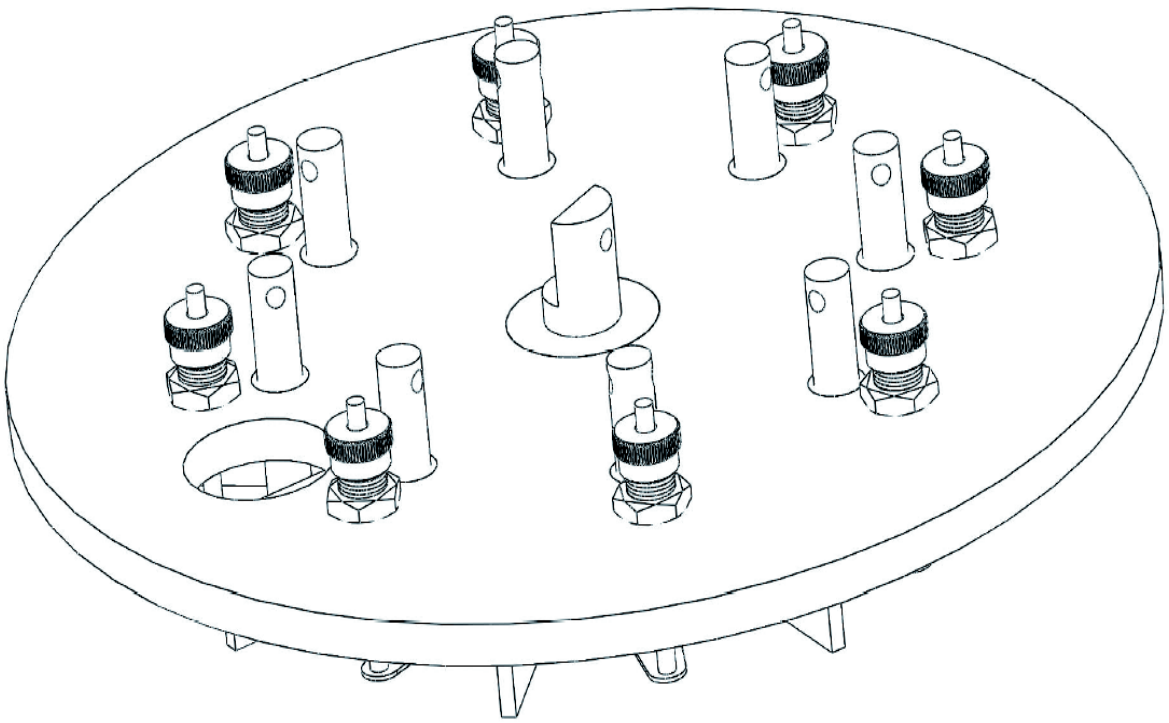

Figure 3-3 Back side of Eight Sources Evaporation System bottom plate

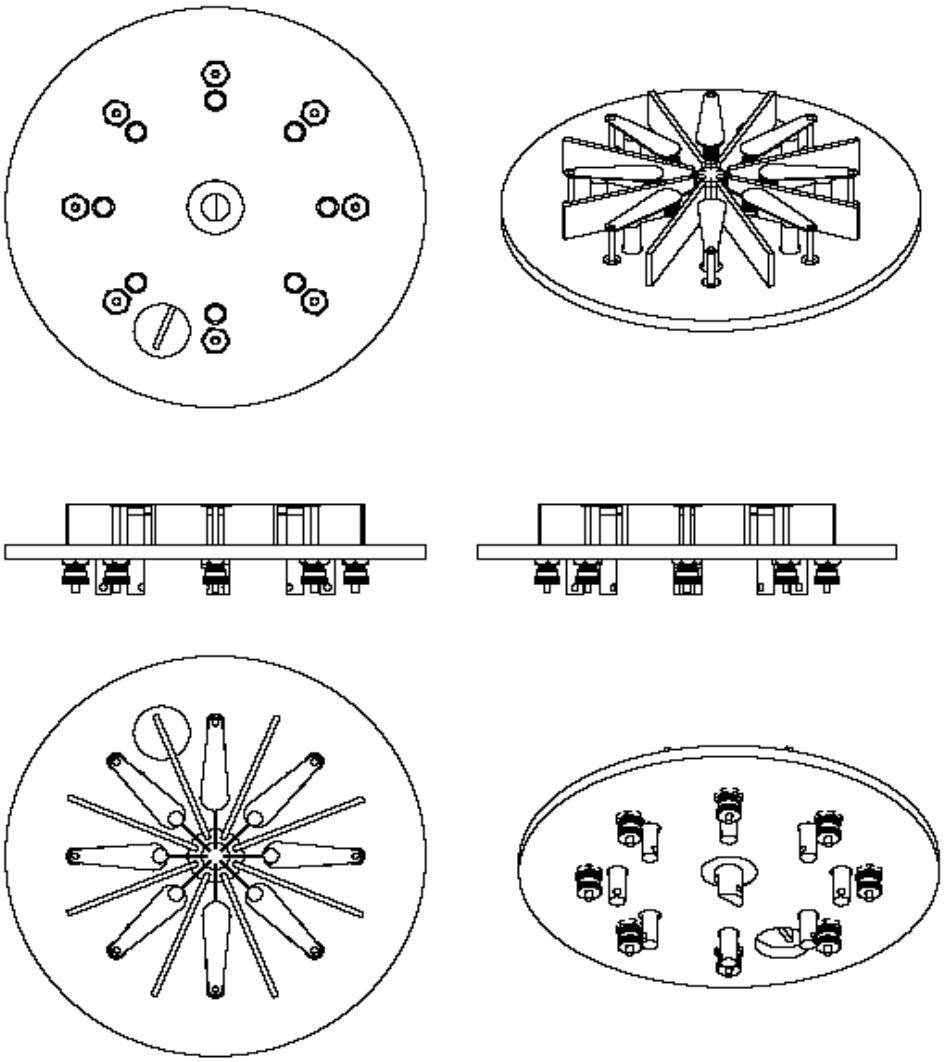

Figure 3-4 Bottom plate 3D sketch

3.2 Top Plate Design

The top plate is an important component for the evaporation system. The first function is to cover the top of the chamber and to form a sealed environment. Besides, there are always some intricate designs (such as sliding shutter, thickness monitor, etc.) on the top plate to fully use this spare space. Unlike industry's deposition systems, these have a much larger chamber, are highly auto-controlled, more complicated but include precise transportation mechanical systems.

To eliminate the side effect of the thickness of the monitor holder, which results in un-uniform distribution of evaporation particles, the pole used to sustain the monitor is removed. Instead, two thickness monitors are installed on the top plate as shown in Figure 3-5. These monitors are connected to a microdot feedthrough on the top plate from which data can be

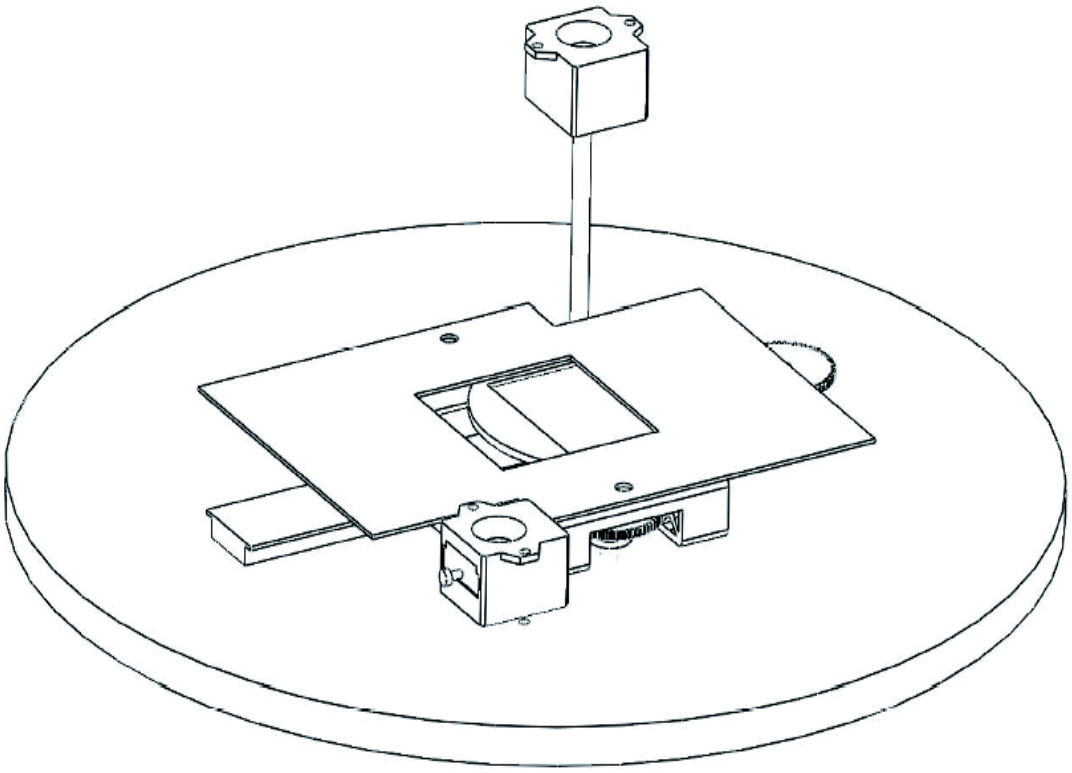

Figure 3-5 Two thickness monitors installed on the top plate

transmitted to the controller. One monitor is tightly fixed on the base plate. The height of the oscillate crystal surface is the same as the substrate surface, thus the monitor can measure the thickness of the deposited thin film. The other monitor is installed on a pole, which can change the height of the thickness monitor. Usually, this thickness monitor will be at the same height as the substrate surface. Comparing with the readings from the other monitor, uniformity of the thin film is determined. On the other hand, to co-dope two materials, the second monitor is lowered to the middle position between the substrate and the evaporation source. Thus, theoretically, the monitor could give a four times higher resolution. This assists to precisely control the doping ratio and the depositing speed.

The previous top plate can provide a one-dimensional series change to the thin film's thickness. However, the vacuum must be broken and the device rotated. Therefore, a two-dimensional structure can be designed in one substrate. While the interface of organic thin films is very important to the quality of the device, breaking the vacuum introduces an unknown effect to the interface of thin films. Thus, if the substrate is rotated without breaking the vacuum, the device quality will be better, and also enhance the experiment's efficiency. Following this idea, a substrate holder with gear as shown in Figure 3-6 is designed and mounted on a rack, which can move freely in one dimension. The rack pinions fit together with the gear on the top plate as shown in Figure 3-7. Rotating the knob on the other side of the plate controls the position of the rack and the substrate holder. With a fixed mask above the substrate, the thickness of the deposited film can be changed in a one-dimension series. When the position of the rack moves to one end of the track, the gear on the substrate holder attaches the gear on the top plate (Figure 3-8). Therefore, the substrate holder can be rotated 90 degrees. Then, moving the rack again, the second dimension of the thin film can be deposited. So, this mechanical gear design can help the

system fabricate two-dimensional structure OLED devices and greatly enhance the experiment's efficiency.

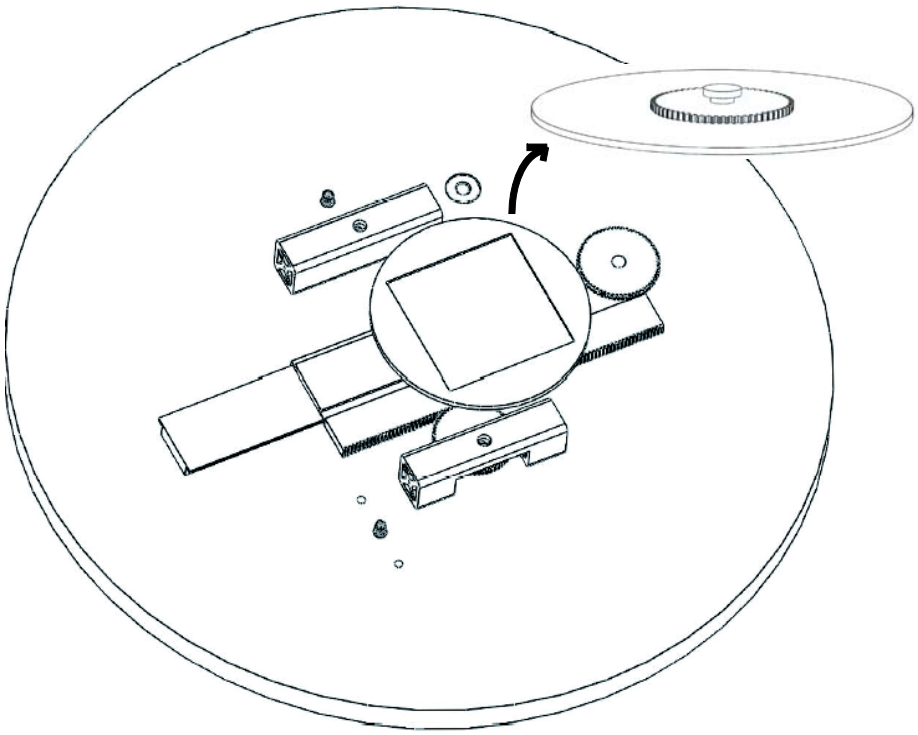

Figure 3-6 Rotating substrate holder is installed on the top plate

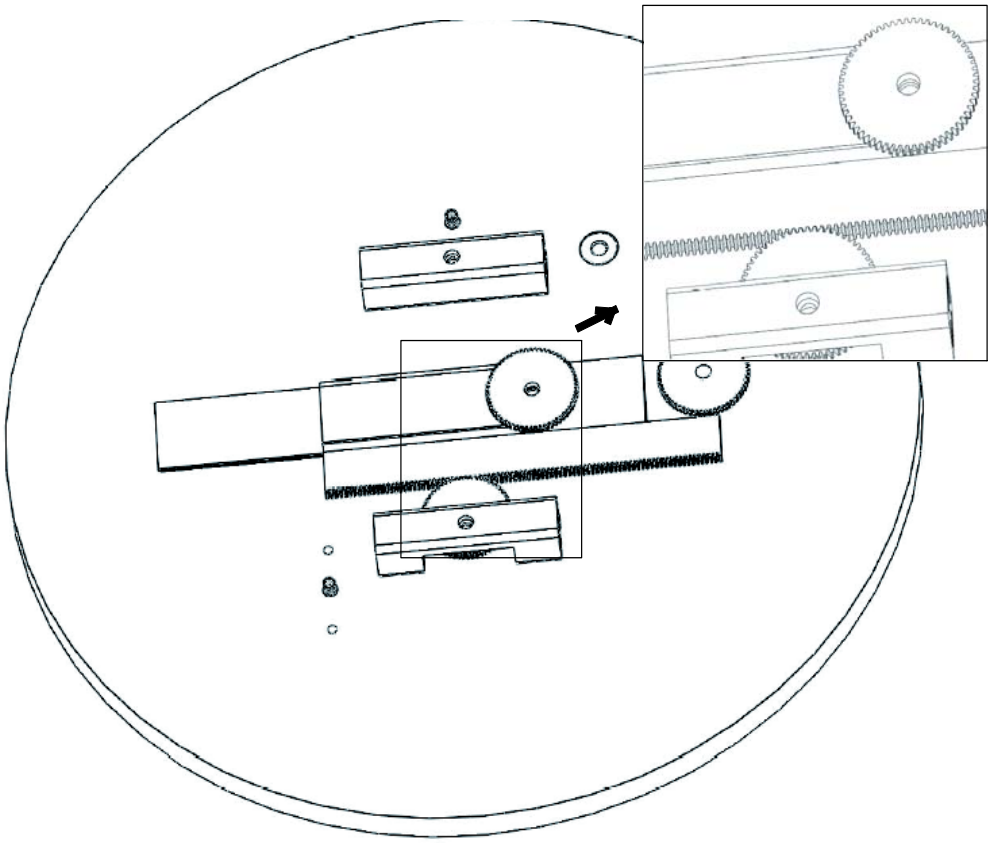

Figure 3-7 The position of the rack and the substrate are controlled by the gear, which fits together with the rack pinion

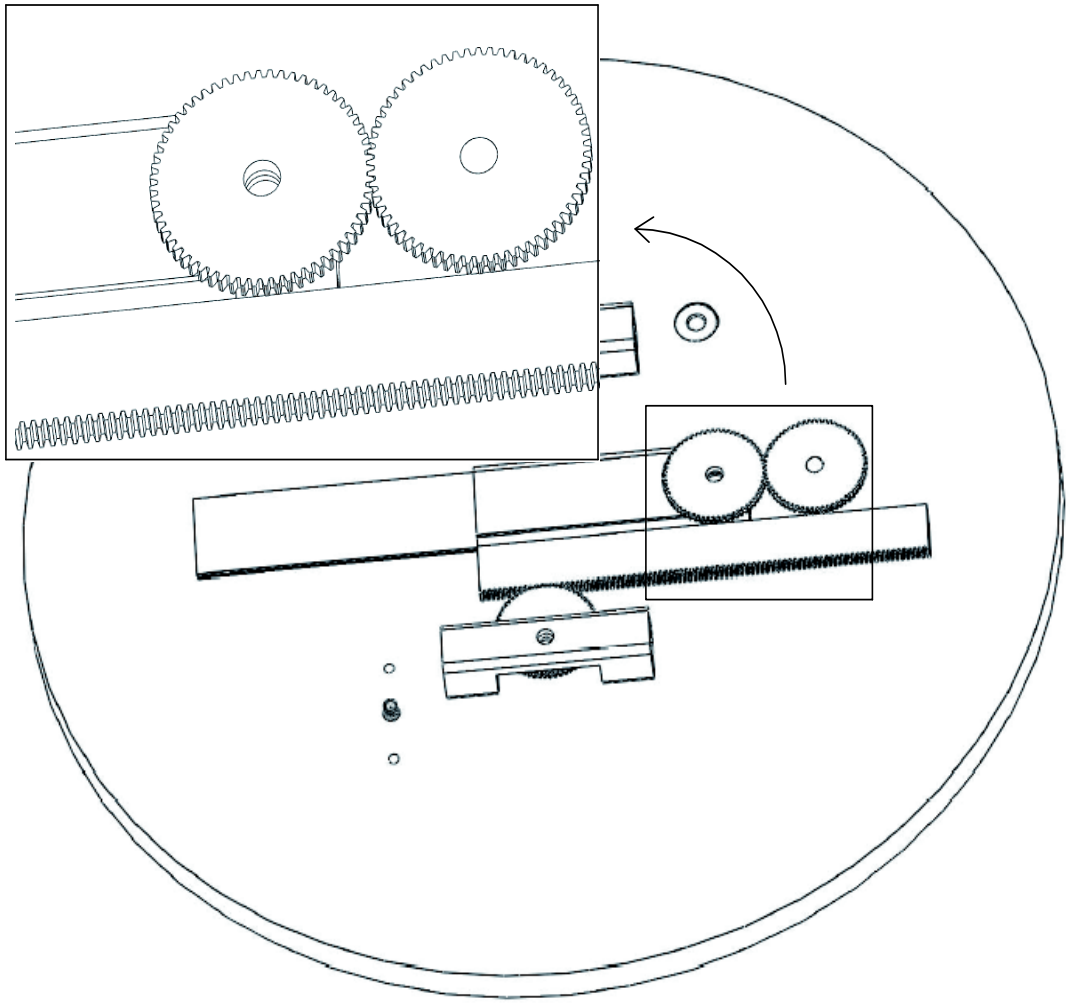

Figure 3-8 Gear on the substrate holder attaches to the gear on the top plate

When depositing the metal cathode on the devices, another patterned mask can be attached to the fixed shutter mask as shown Figure 3-9. The shape of the cathode can be determined by windows on the patterned masks.

On the top plate, an extra vacuum valve is installed (shown in Figure 3-10) to back fill the chamber after deposition. The argon in the glove box can flow into the vacuum system directly from the top plate, excluding the possibility of pump oil contamination.

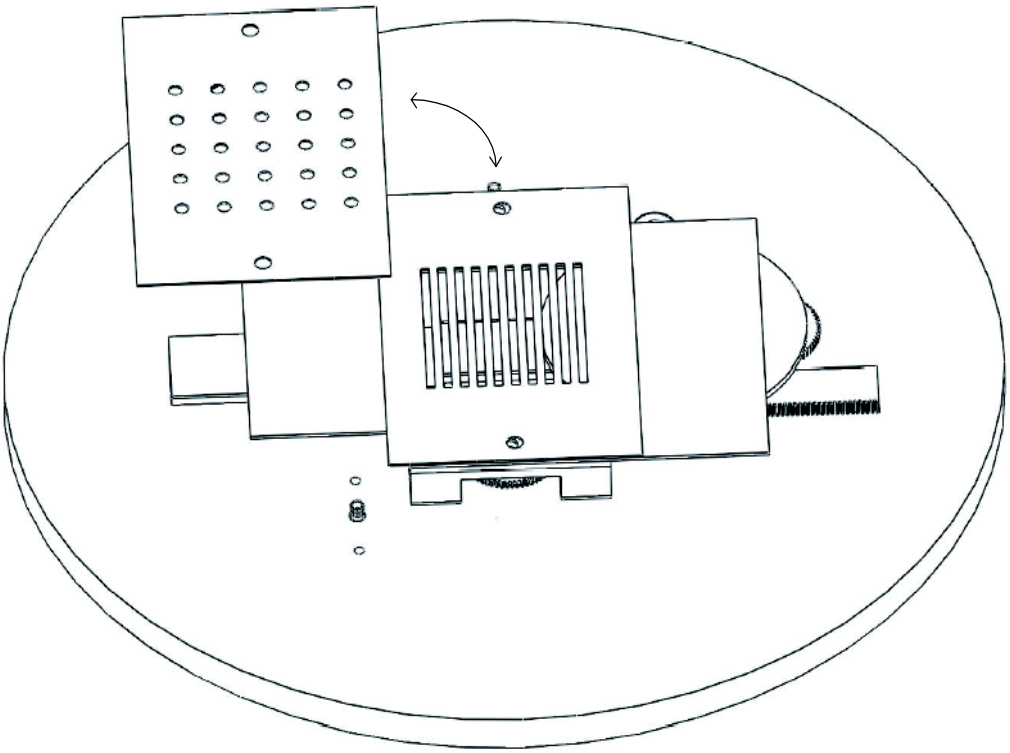

Figure 3-9 Different patterned masks attached on the fixed shutter to determine cathode shape

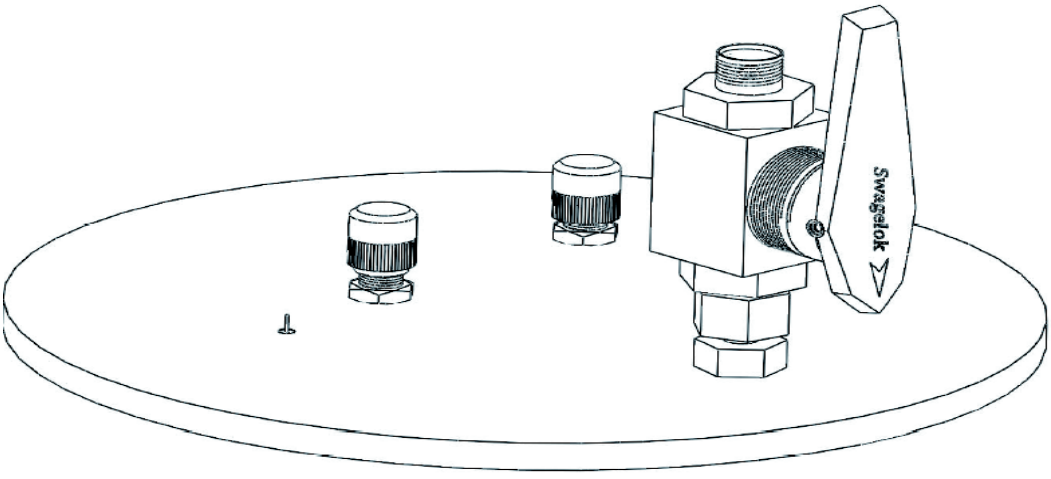

Figure 3-10 a swagelok vacuum valve installed on the top plate

Below, Figures 3.11-3.13 show the top plate's components and their relative position.

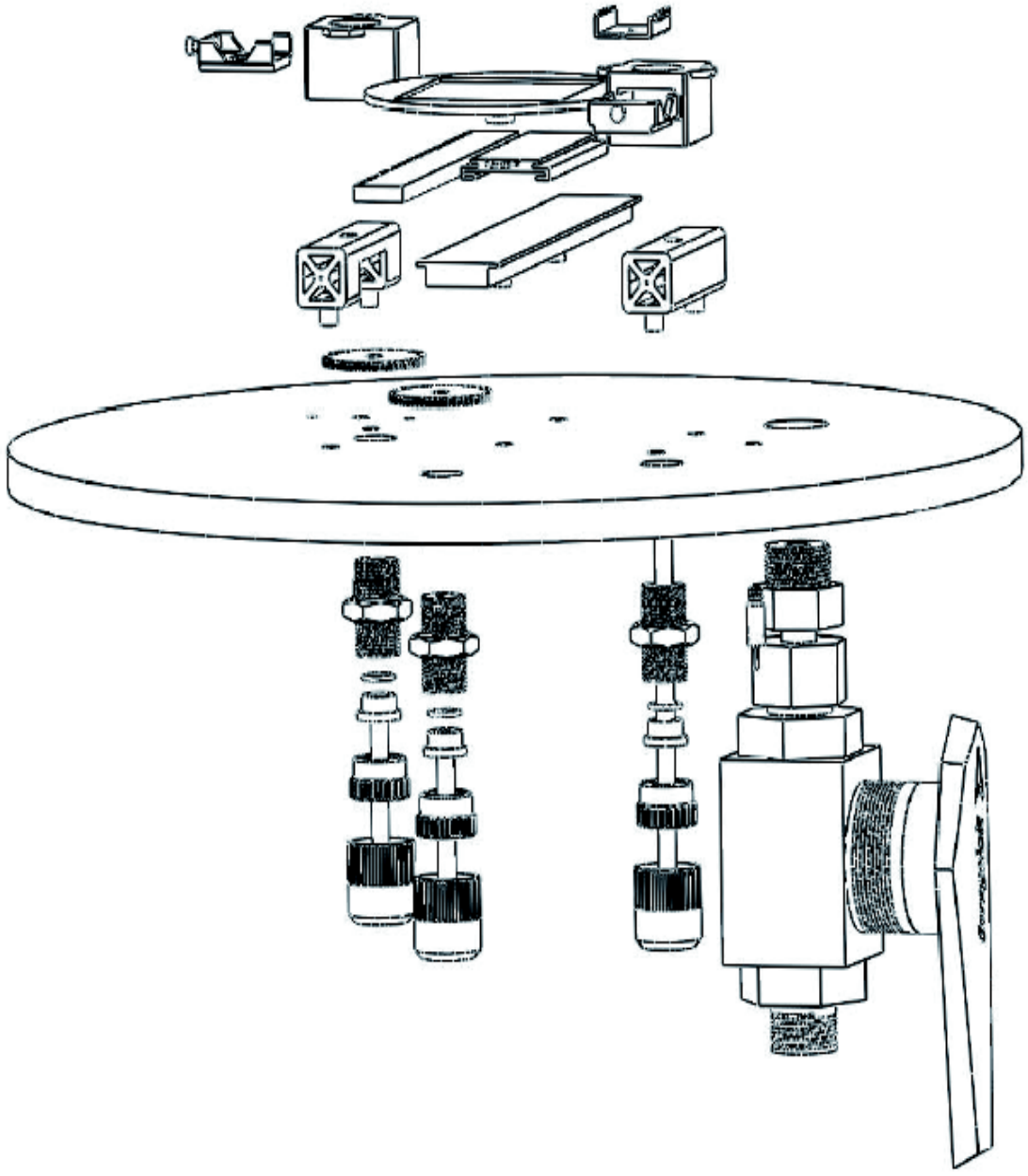

Figure 3-11 Components of the top plate

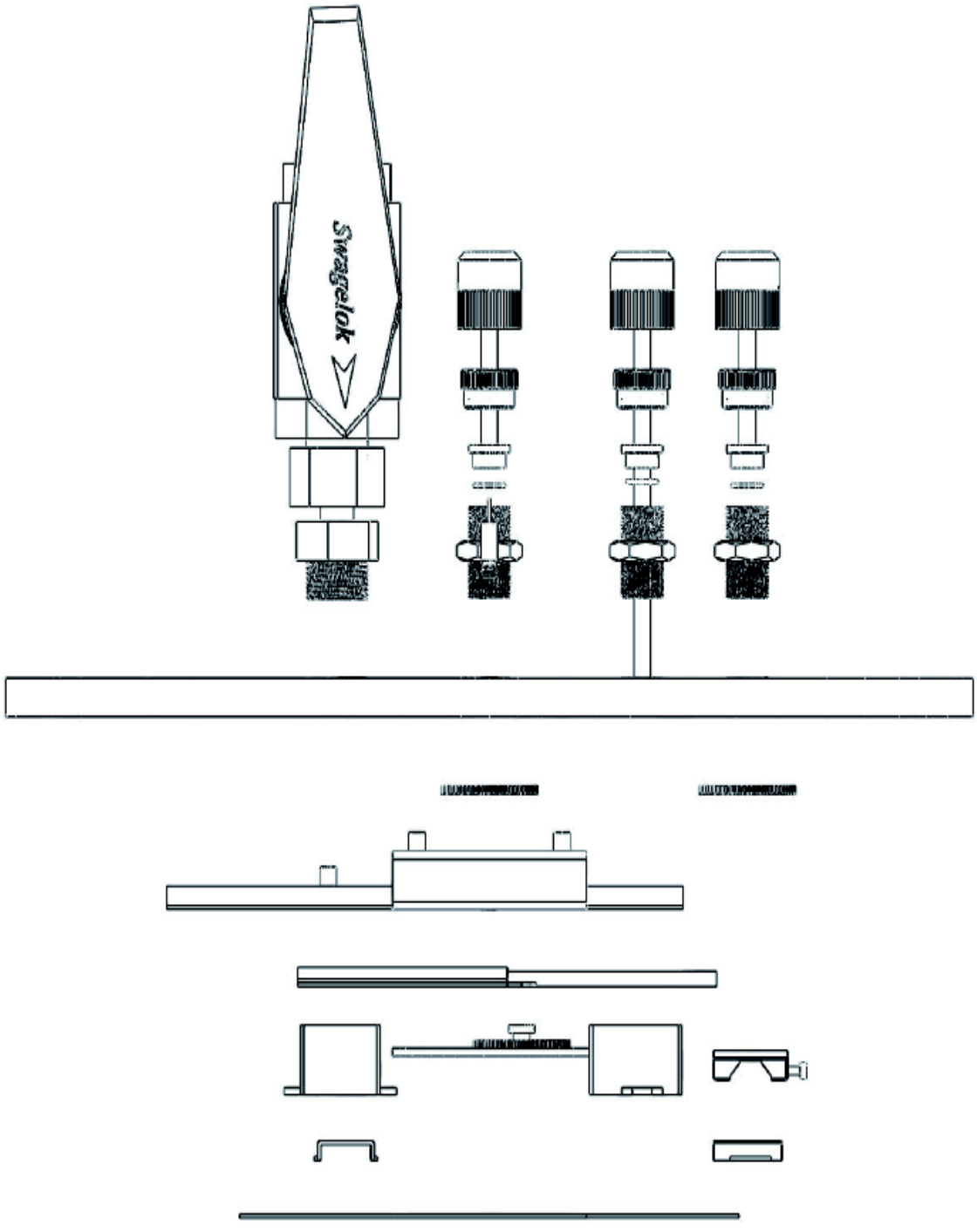

Figure 3-12 Side view of the top plate components

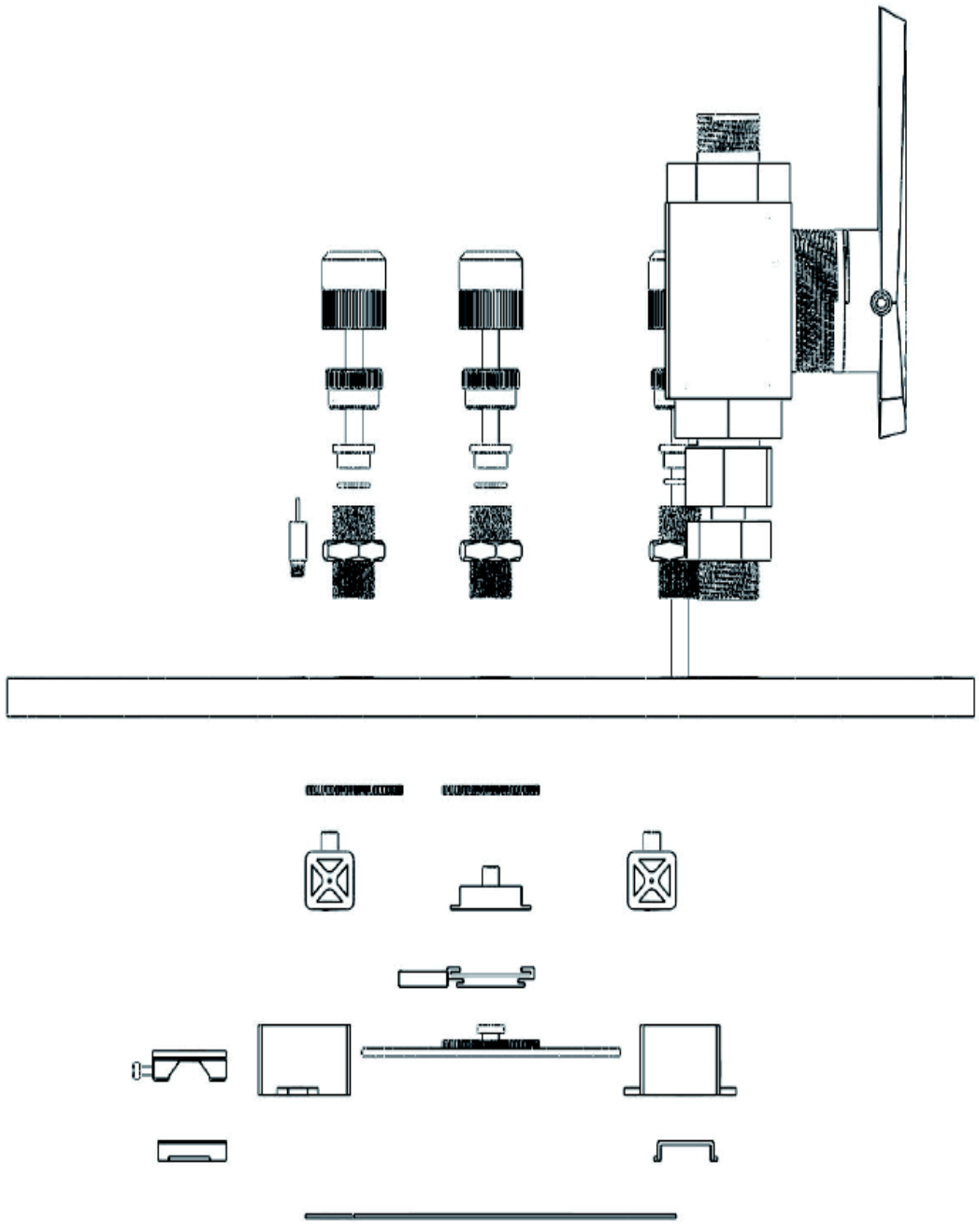

Figure 3-13 Side view of the top plate components

CHAPTER 4 SPECTRALLY NARROWED EDGE EMISSION FROM LEAKY WAVEGUIDE MODES IN OLEDS

Zhengqing Gan,[1] Yun Tian,[1] David W. Lynch,[1] Ji-hun Kang,[2] Q-Han Park,[2] and Joseph Shinar[1]*

[1]*Ames Laboratory-USDOE and Department of Physics and Astronomy*

Iowa State University, Ames, IA 50011, USA.

[2]*Department of Physics, Korea University, Seoul 136-701, Korea.*

A dramatic spectral line narrowing of the edge-emission, at room temperature, from tris(quinolinolate) Al (Alq_3), N,N'-diphenyl-N,N'-bis(1-naphthylphenyl)-1,1'-biphenyl-4, 4'-diamine (NPD), 4,4'-bis(2,2'-diphenyl- vinyl)-,1'- biphenyl (DPVBi), and some guest-host small molecular organic light-emitting diodes (OLEDs), fabricated on ITO-coated glass, is described. In all but the DPVBi OLEDs, the narrowed emission band emerges above a threshold thickness of the emitting layer, and narrows down to a full width at half maximum of only 5 - 10 nm. The results demonstrate that this narrowed emission is due to irregular waveguide modes that leak from the ITO to the glass

substrate at a grazing angle. While measurements of variable stripe length *l* devices exhibit an apparent weak optical gain $0 \leq g \leq 1.86$ cm^{-1}, there is no observable threshold current or bias associated with this spectral narrowing. In addition, in the phosphorescent guest-host OLEDs, there is no decrease in the emission decay time of the narrowed edge emission relative to the broad surface emission. It is suspected that the apparent weak optical gain is due to misalignment of the axis of the waveguided mode and the axis of the collection lens of the probe. However, it is not clear if such a misalignment can account for all the effects of the observed evolution of the edge emission spectra with *l*.

PACS number: 85.60.Jb, 78.60.Fi, 85.65.+h, 78.66.Qn

*Corresponding author. E-mail address shinar@ameslab.gov

4.1. Introduction

The demonstration of optically pumped organic lasers[1] has inspired intense efforts to achieve lasing via electrical injection in organic light-emitting diodes (OLEDs). This goal, however, has remained elusive. Under optical pumping, a singlet exciton (SE) is directly generated on a single molecule or conjugated segment of a polymer. The main optical losses competing with laser action are spontaneous emission, various SE quenching mechanisms, and propagation dissipation in wave-guided structures. Electrical excitation is a different process, where the electron and hole are injected separately into the active region to recombine to either a SE or a triplet exciton (TE). Additional strong losses arise from the presence of absorbing species such as polarons[2,3] and the incorporation of absorbing metal electrodes.[4] Moreover, the electroluminescence (EL) quantum efficiency is reduced substantially at high current density due to quenching of SEs by other SEs, by TEs, and by polarons.[5,6] This presents a major obstacle in reaching the lasing threshold.

This paper describes striking spectrally narrowed edge emission (SNEE) from small molecular OLEDs (SMOLEDs)[7,8] and measurements on these devices with variable stripe length (VSL),[9,10] which exhibit an apparent weak optical gain. These are two key features of amplified spontaneous emission (ASE), i.e., mirrorless lasing. However, no threshold bias or current for this spectral narrowing is observed. The results demonstrate that the SNEE results from irregular leaky waveguide modes propagating in the lateral

direction along the OLED/glass substrate interface, which are consequently quite different from the regular waveguide modes that are confined entirely within the OLED layers.

4.2. Experimental Procedure

Various multilayer SMOLEDs were fabricated on Colorado Concept Coatings (formerly Applied Films Corp.) ITO-coated glass substrates. The R ~ 20 Ω/ , 140 nm-thick ITO coated 2"×2" glass substrates were cleaned by detergent and organic solvents and then treated in a UV/ozone oven to increase the ITO work function and facilitate hole injection, as described elsewhere.[11-13] The organic layers, CsF buffer layer,[14,15] and Al cathode were deposited in a thermal vacuum evaporation chamber (background pressure < 5×10^{-6} Torr) installed in an Ar-filled glove box. The organic layers typically included a copper phthalocyanine (CuPc) hole injecting layer, an N,N'-diphenyl-N,N'-bis(1-naphthylphenyl)-1,1'-biphenyl-4,4'-diamine (NPD) hole transport layer (HTL), the emitting layer of variable thickness, and a tris(quinolinolate) Al (Alq_3) electron transport layer (ETL) or 2,9-dimethyl-4,7-diphenyl-1,10-phenanthroline (bathocuproine (BCP)) ETL and hole-blocking layer. The emitting layer was either Alq_3, NPD, 4,4'-bis(2,2'-diphenylvinyl)-1,1'-biphenyl (DPVBi) or *fac* tris(2-phenylpyridine) iridium [Ir(ppy3)]- or Ir(III)bis[4,6-di-fluorophenyl-pyridinato-N,C2']picolinate (FIrpic)-doped

4,4'-bis(9-carbazolyl)biphenyl (CBP). The Al cathode was deposited through a shadow mask containing 21×21 1.5 mm-diameter circular holes, yielding a 21×21 matrix array of OLED pixels. By using a combinatorial sliding-shutter technique, the thickness of two of the organic layers could be varied systematically across the 21×21 matrix array, as described elsewhere.[7,11]

For VSL measurements, 1 mm-wide striped OLEDs, up to 20 mm long, were fabricated by evaporating the Al through a mask with appropriate slits. Such measurements are typically conducted to provide evidence for optical gain, and consequent ASE in inorganic semiconductors and optically-pumped organic films.[9,10] To our knowledge, our preceding paper[8] and this paper describe the first detailed VSL measurements in electrically pumped organic devices. When conducting the VSL measurements, the length of the Al cathode was shortened for each step, by either 1 or 0.5 mm. In other words, the VSL measurements described in this work were destructive. In some cases, however, the ITO was photolithographically etched to yield stripes with lengths varying systematically from 100 to 1400 μm, i.e., the VSL measurements were carried out on a series of OLEDs.

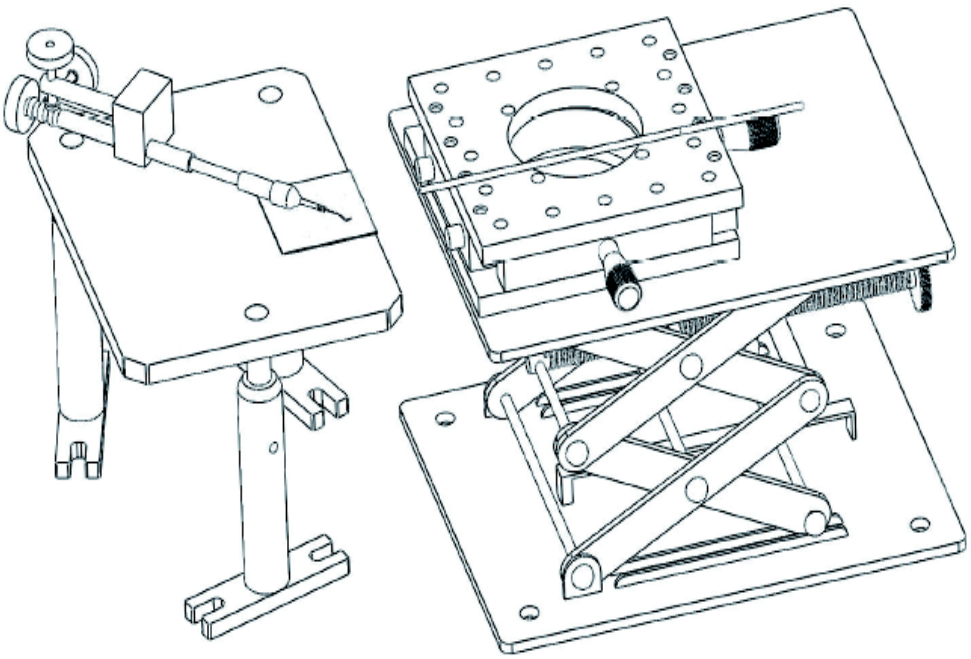

Figure 4-1 Edge emission detection system

Figure 4-1 shows the experimental setup for measuring the edge emission. It included an optical bench and an Ocean Optics Chem 2000 spectrometer. A metal probe installed on the platform was connected to the device cathode; 0 – 38 V DC was provided by a Kepco DPS-40-2M programmable power supply, and the current was measured using a Keithley 2000 multimeter. The optical fiber of the spectrometer was fixed on an *xyz* micropositioner, and oriented perpendicular to the edge of the device, collecting ~2^{o} of the emitted light around that direction. The position of the fiber tip was adjusted to maximize the EL intensity and minimize its linewidth. For polarization-dependent

measurements, a linear polarizer was placed in front of the probe. To measure surface and edge emission spectra simultaneously, two spectrometers and two computers were used. This ensured that the surface and edge emission spectra were monitored simultaneously at the same current density, enabling a reliable comparison between them.

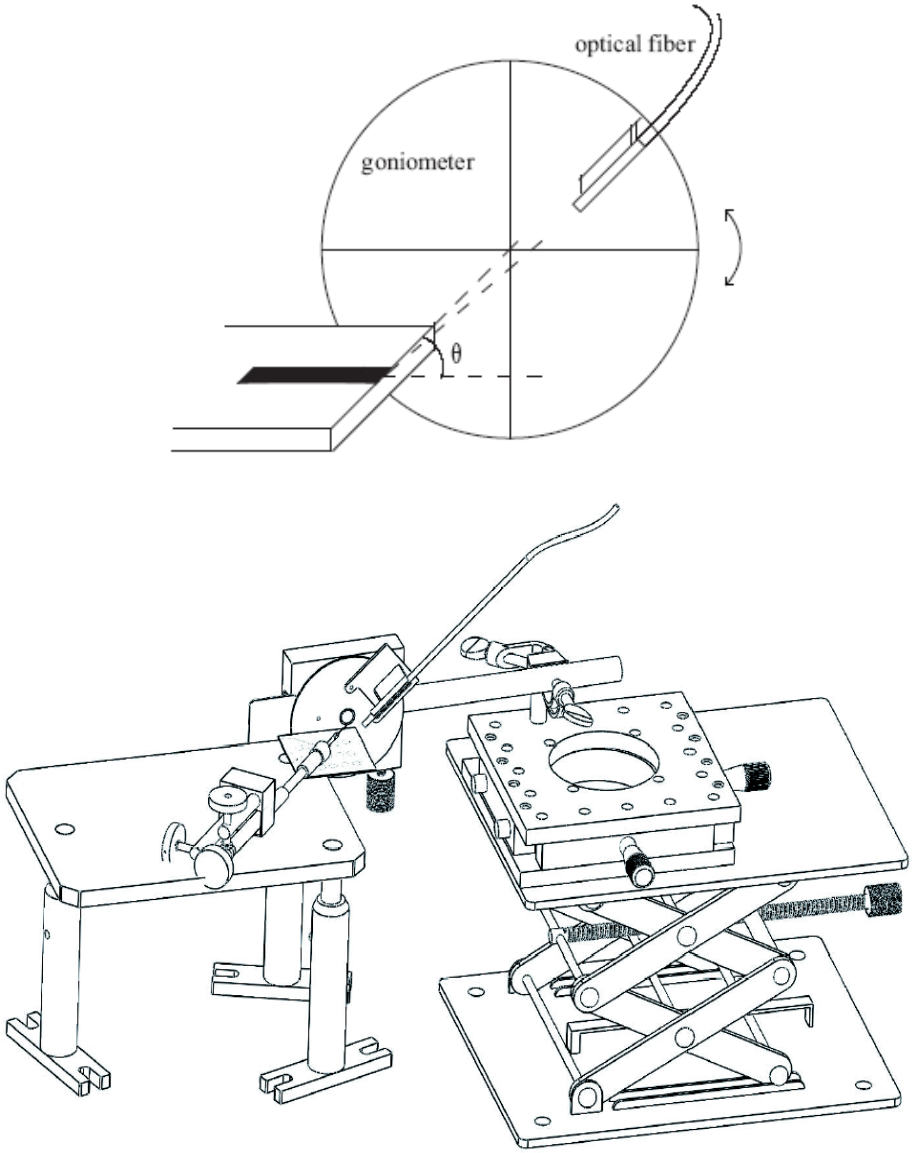

Figure 4-2 The sketch of the angle-dependent VSL measurement setup

To measure the angle dependence of the SNEE, instead of fixing the optical fiber on a micropositioner, it was held in a homemade holder which was fixed on a goniometer that could change the detection angle (see Figure 4-2). This total assembly was fixed on the *xyz* micropositioner, and the OLED was fixed on the edge of a stage. The edge of the device was placed at the center of the goniometer. Hence we could ensure that regardless of the angle θ, the optical fiber was always directed towards the edge of the device.

For optical pumping experiments, the set-up was the same, with the exception that a laser beam was guided to the surface of the organic film. The laser intensity was controlled by either the laser power supply or a neutral density filter. The laser beam diameter was ~1 mm, and its direction was controlled by a mirror.

The lifetime of the surface and edge EL of phosphorescent OLEDs were also measured. The EL was guided into a photomultiplier tube (PMT) that had a response time < 10 ns.

4.3. Results And Discussion

4.3.1. Alq_3 OLEDs

Figure 4-3 shows the behavior of the (a) edge emission and (b) surface emission from glass/[~100 nm ITO]/[5 nm CuPc]/[45 nm NPD]/[*x* nm Alq_3]/[1 nm CsF]/Al OLEDs, fabricated combinatorially as described above. As clearly seen, the surface emission is

the expected broad EL spectrum peaking at ~530 nm. However, for x = 65 and 85 nm, the edge emission exhibits a narrower emission band at 590 and 600 nm, respectively. Such a narrow transverse magnetic (TM)-polarized edge emission was described by Bulovic et al.[16] However, they did not describe the edge emission from devices with thicker Alq_3 layers. As Figure 4-3 shows, a narrow transverse electric (TE) edge-emission band peaking at ~440 nm emerges at $65 \leq x \leq 85$ nm. With increasing x, this band intensifies and red-shifts, and the TM band weakens until it is no longer observable at x = 125 nm.

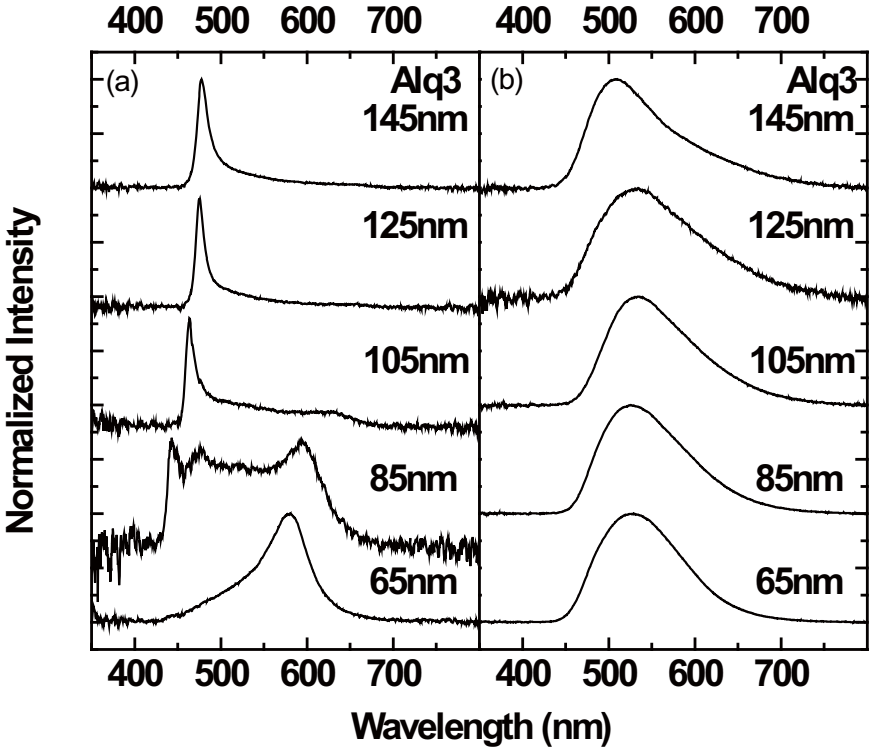

Figure 4-3 (a) Edge and (b) surface emission from glass/[~100 nm ITO]/[5 nm CuPc]/[45 nm NPD]/[x nm Alq3]/[1 nm CsF]/Al OLEDs, where x = 65, 85, 105, 125, and 145nm.

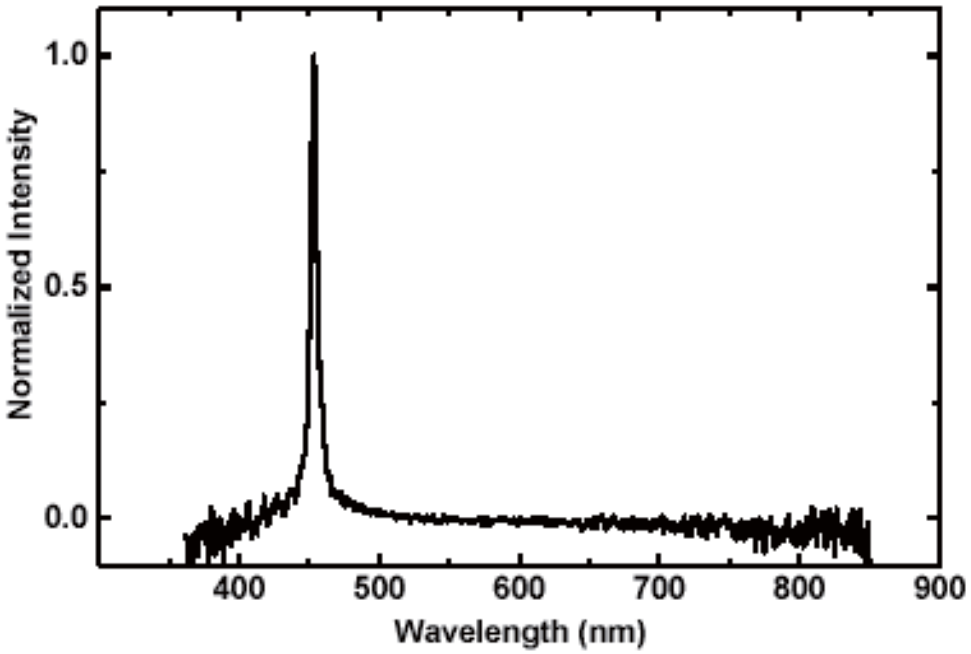

Figure 4-4 Edge emission spectrum of a glass/[~100 nm ITO]/[5 nm CuPc]/ [45 nm NPD]/[120 nm DPVBi]/[7 nm Alq3]/[1 nm CsF]/Al OLED.

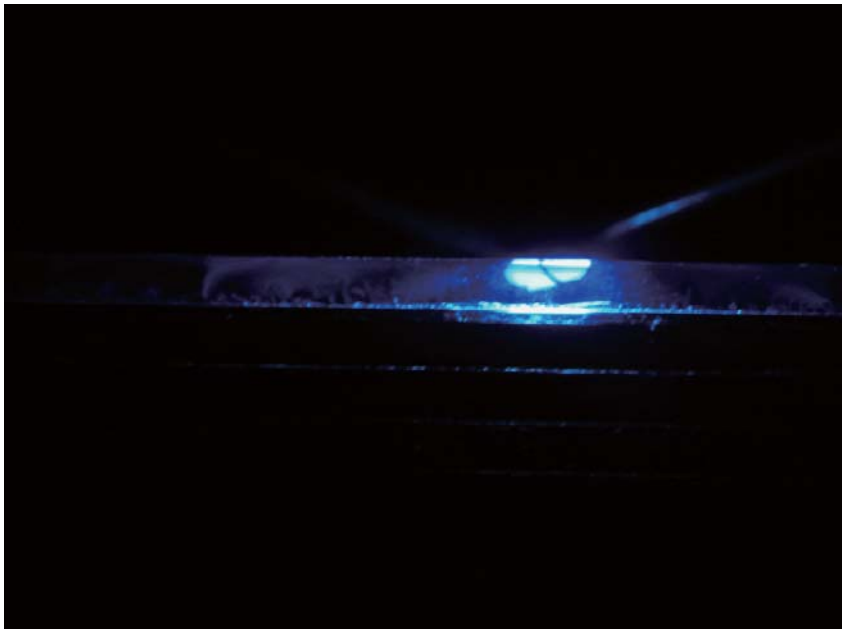

Figure 4-5 The photograph of the edge emission from the DPVBi device.

4.3.2. DPVBi OLEDs

Figure 4-4 shows the edge emission spectrum from glass/[~100 nm ITO]/[5 nm CuPc]/[45 nm NPD]/[120 nm DPVBi]/[7 nm Alq_3]/[1 nm CsF]/Al OLED. The full width at half maximum (FWHM) is $\Delta\lambda_{1/2} \approx 5$ nm. We note that this $\Delta\lambda_{1/2}$ was independent of the driving voltage, so, in particular, there was no apparent threshold voltage or current density above which the edge emission spectrum narrowed.

Figure 4-5 shows an image of the DPVBI OLED edge emission. From the image it is obvious that the edge emission includes two parts: the upper part and the lower part. We will demonstrate that the upper part results from waveguide modes that leak from the ITO + organic layers into the glass substrate. The bright spot which is under the upper part emission is due to scattering by the edge facet which is not polished. The lower part of the emission is due to reflection of the light at the glass/air interface; we suspect this part of the emission is identical to the surface emission.

4.3.3. NPD:Spiro-DPVBi OLEDs

Figure 4-6 shows the edge EL spectra of ITO/[5 nm CuPc]/[40 nm NPD]/[*x* nm 1:1 NPD:spiro- DPVBi]/[40 nm spiro-DPVBi]/[8 nm Alq_3]/[1 nm CsF]/Al OLEDs, for x = 10, 30, 50, 70, and 90 nm. Addition of this blend layer is believed to increase the width of the recombination zone,[17,18] which, in turn, might increase the waveguide core thickness.

This effect is evident in Fig. 6 by the systematic progression of different waveguide modes: When the mixed layer is relatively thin, the spectrum is dominated by a strong TE_0 mode and a weak TM_0 mode. With increasing blend layer thickness, the peak of the TM_0 mode becomes stronger, and the third peak, which is the TE_1 mode, emerges. Especially interesting is the spectral evolution of the TE_0 mode, which becomes nearly negligible in the device with the 90 nm-thick blend layer. On the other hand, the TE_1 mode shows a strong and sharp peak with a FWHM of only 7 nm.

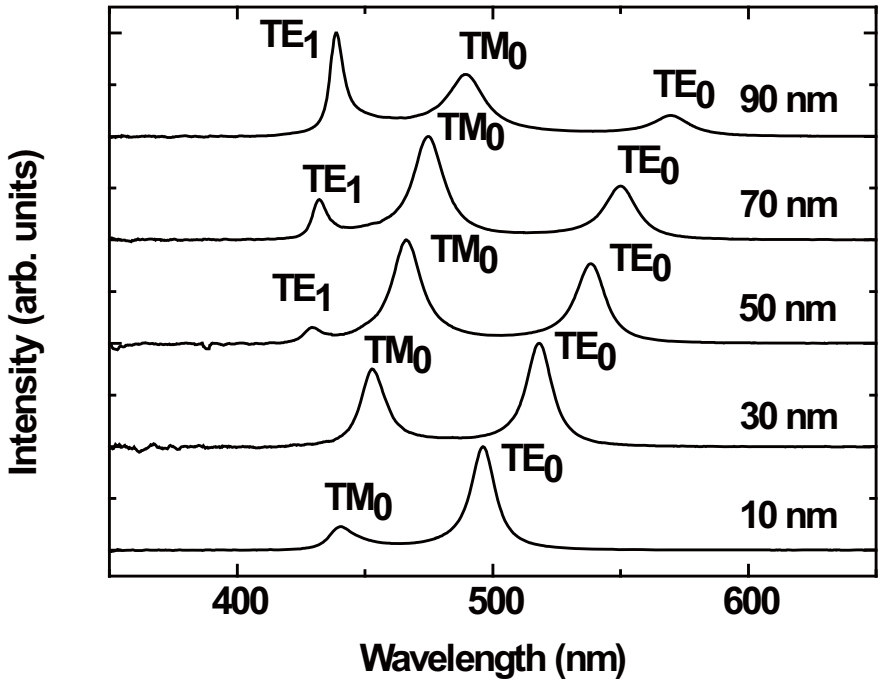

Figure 4-6 Edge emission EL spectra of ITO/[5 nm CuPc]/[40 nm NPD]/[x nm 1:1 NPD:spiro- DPVBi]/[40 nm spiro-DPVBi]/[8 nm Alq3]/[1 nm CsF]/Al OLEDs, x = 10, 30, 50, 70, 90 nm.

4.3.4. Leaky vs regular waveguide modes

The alternating appearance and disappearance of the TE and TM modes seen in Figure 4-6 is characteristic of waveguide modes. Yet, as previously shown,[16] light that propagates in the organic + ITO waveguide, with the glass and Al cladding, would be subject to losses of the order of 1000 cm^{-1}, due primarily to the strong absorption of the evanescent tail of the optical field that penetrates the Al cathode. In addition, the ITO is also lossy,[16] particularly at $\lambda < 450$ nm. Consequently, the wave-guided light would be completely absorbed before it contributes to any far-field edge emission. Therefore the SNEE is not due solely to the regular waveguide modes, which are trapped in the organic and ITO layers, and cannot escape unless there is enough optical gain. This conclusion is supported by edge emission measurements on patterned OLEDs in which the organic and ITO layers at the edge of the glass substrate were etched off and replaced by a tape, thus blocking the emergence of the waveguide modes from the edges of those layers: The resulting spectral shape, polarization and intensity were almost identical to those of the SNEE from OLEDs whose ITO layers remained unpatterned, demonstrating that the SNEE exits from the edge of the glass substrate and cannot be attributed to regular waveguide modes.

4.3.5. Polarization of the edge emission

The behavior of the SNEE clearly shows that it is related to a waveguide effect. Since the refractive indices of the organic layers $n \sim 1.7$ and the ITO's $n \sim 1.9$ are greater than that of the glass where $n \sim 1.5$, the combined organic and ITO layers constitute a dielectric slab waveguide core, with the glass and Al as the waveguide claddings, resulting in a three-slab asymmetric waveguide structure. This structure preferentially supports the TE polarization.[19]

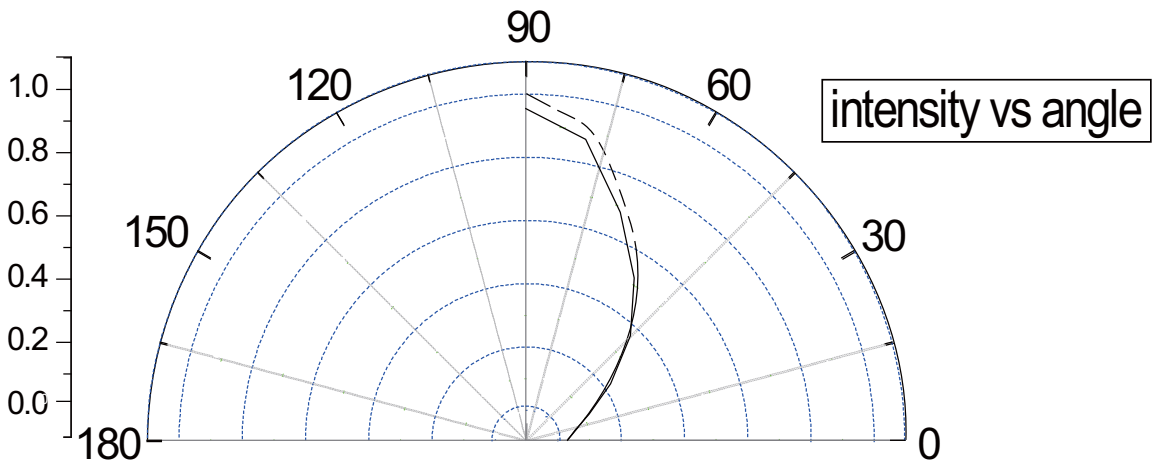

Figure 4-7 The edge emission intensity versus polarization angle in polar coordinates: the solid line is the experimental data, the dashed line is the theoretical data fitting by Eq.(1).

Figure 4-7 demonstrates the polarization of the edge emission. The solid line is the normalized experimental spectrum; the dashed line is the curve with the relation

$$I = \cos^2\theta \qquad (1)$$

where θ is the polarization angle (the angle between the polarizer and the substrate surface). The overlap of these two curves shows that the edge emission is almost totally TE polarized. It might be argued, however, that such high TE polarization arises because the planar DPVBi and NPD molecules lie preferentially in the plane of the substrate, so more light is emitted with a TE polarization due to the preferential orientation of the SE dipoles in the plane of the substrate. Yet the SNEE from OLEDs based on spiro-DPVBi and Alq_3, which are intrinsically nonplanar, was also fully TE polarized. Additionally, in SMOLEDs fabricated by thermal evaporation, where the organic layers are amorphous, the dipoles are most likely randomly oriented.

4.3.6. Photoexcitation measurements

To better understand the nature of the SNEE, thin films and similar OLEDs structures were optically pumped by an Ar^+ laser at 363 nm, with the laser beam perpendicular to the organic layer surface. Because the difference in the refractive indices of most of the organic materials used in this study is marginal, a single layer, with a thickness equal to that of the multilayer OLEDs, should form a slab waveguide configuration similar to that of the OLEDs.

To distinguish between the leaky and regular waveguide modes, we note that the two have a different dependence on the refractive index difference Δn at the surface.[20] Δn can

be changed by placing drops of various liquids on a photo-excited spot of the emitting film shown in Figure 4-8.

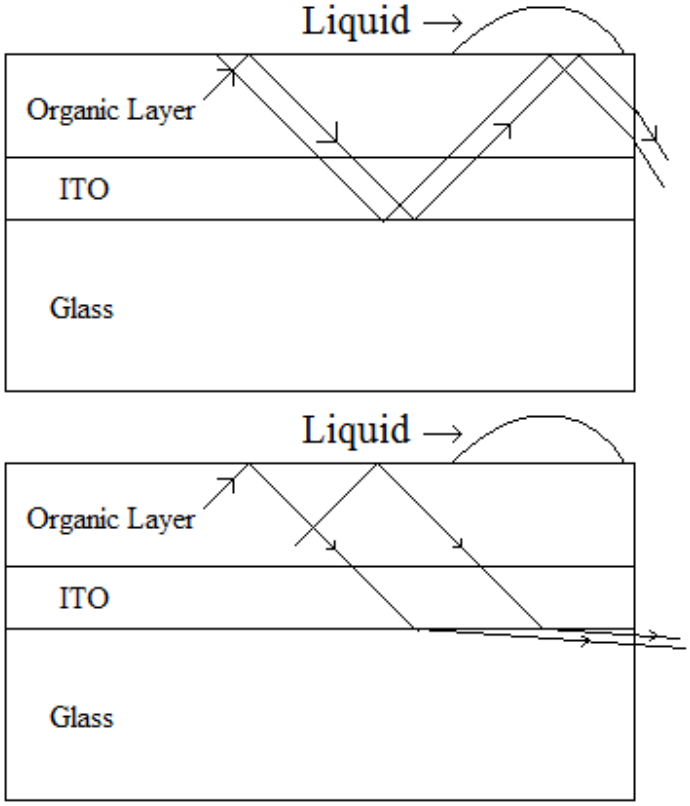

Figure 4-8 A drop of various liquids is placed on a photo-excited spot of the emitting film. If the edge emission is due to waveguide modes in the organic and ITO layers (top figure), then the change in the index of the cladding layer will strongly distort the edge emission spectrum, since reflections on the upper boundary control the phase condition for mode selection. If the edge emission is due to the leaky modes in the glass substrate (bottom figure), the change in the cladding layer index will have no effect on the mode, because all energy flux has leaked into the substrate.

If the edge emission is due to waveguide modes in the organic and ITO layers, then the change in the index of the cladding layer will strongly distort the edge emission spectrum, since reflections on the upper boundary control the phase condition for mode

selection. However, if the edge emission is due to the leaky modes in the glass substrate, the change in the cladding layer index will have no effect on the mode, because all energy flux has leaked into the substrate. Therefore, a DPVBi film was deposited on the surface of the ITO-coated glass substrate. It was optically pumped by the 363 nm line of an Ar^+ laser. No change in the edge emission spectrum was observed with drops of different liquids, providing clear evidence that the edge emission is due to leaky modes. For comparison, the surface emission spectrum varied significantly with the drops, since at the excitation region, most of the energy is still confined in the core layer, and the light still interacts with the upper boundary.

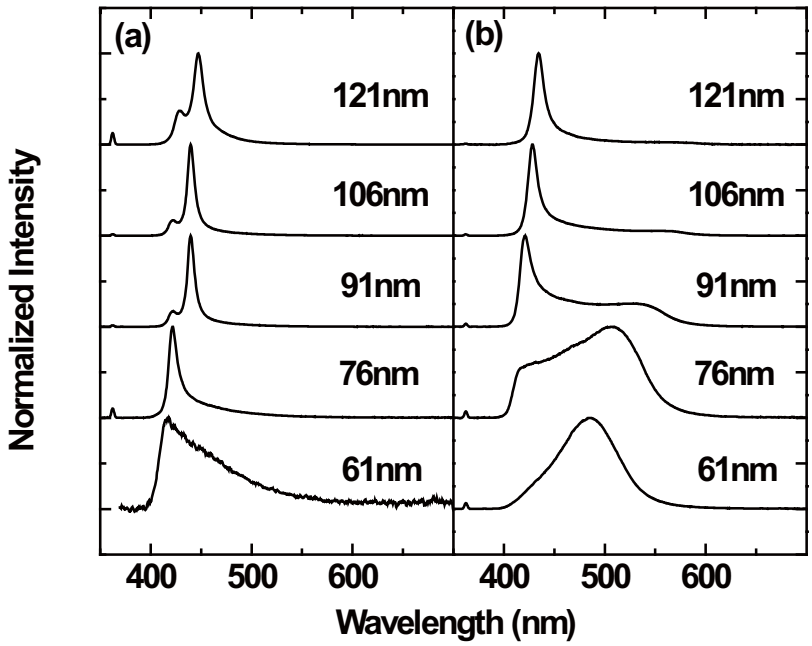

Figure 4-9 PL Edge emission spectra of (a) glass/ITO/[x nm DPVBi] and (b) glass/ITO/[x nm DPVBi]/Al, with x = 61, 76, 91, 106 and 121 nm, photoexcited at 363 nm (see the small peak at that wavelength) by an Ar+ laser.

Next, DPVBi films with varying thicknesses were deposited on ITO-coated glass, and their edge emission was compared to those of similar films on which an Al layer was also deposited. Figure 4-9 shows the edge emission spectra of these photo-excited DPVBi layers; the spectra shown in Figure 4-9b are consistent with the SNEE from the OLEDs shown in Sec. 3.1 – 3.3 above. As clearly seen, in the 61 nm layer without Al, the emission is rather broad, but it narrows with increasing *x*, implying that the waveguide core thickness plays a crucial role. In the samples with Al, the edge emission is quite different: The emission from the 61 nm thick layer is broad and red-shifted relative to the spectrum from the layer without Al. This is indicative of the additional absorption induced by the Al layer. Indeed, the Al layer clearly increases the threshold thickness for the SNEE, and it quenches the TM-polarized modes in the spectra of the 106 nm and 121 nm-thick layers, in agreement with the preferential absorption of TM modes in the metal-clad optical waveguides noted above. In addition, the FWHM of the narrowed spectra with Al is slightly larger than that without Al, providing additional evidence for the absorption by Al.[21]

4.3.7. SNEE from OLEDs with a Ag cathode

To confirm the role of absorption by the metal cathode, DPVBi OLEDs with Al cathodes were compared to those with Ag cathodes, as the latter's absorption coefficient

is much smaller.[21] Figure 4-10 shows that for 20 mm long striped OLEDs, the FWHM of the Al devices is 25.3 nm, while that of the Ag devices is only 9.7 nm. In addition, the TM mode of the Ag devices is stronger than that of the Al cathode, as expected since the TM mode is more strongly affected by the metal cathode than the TE mode.

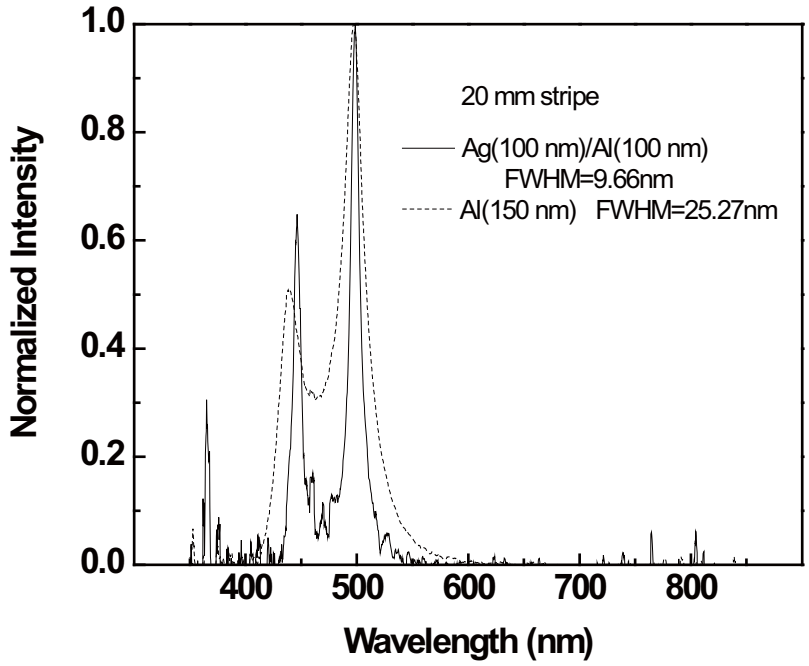

Figure 4-10 Glass/[~100 nm ITO]/[5 nm CuPc]/[40 nm NPD]/[60 nm DPVBi]/[6 nm Alq3]/[1 nm CsF]/[100 nm Ag (solid line) or Al (dotted line)]/Al. Note that the FWHM of the device with a Ag cathode is half that of the device with an Al cathode.

4.3.8. Leaky waveguide mode simulations

To confirm the leaky waveguide mode nature of the SNEE, we now describe their simulation, which assumed that the indices of the refraction of the glass, ITO, and organic layers are $n_G \sim 1.44$, $n_{ITO} \sim 1.90$, and $n_O \sim 1.7$, respectively. To simplify the

simulation, the ITO and organic layers were treated as a single layer (I) with $n_I \sim 1.9$. Thus, the glass and air are the cladding layers of the waveguide, and the organic + ITO is the core layer.

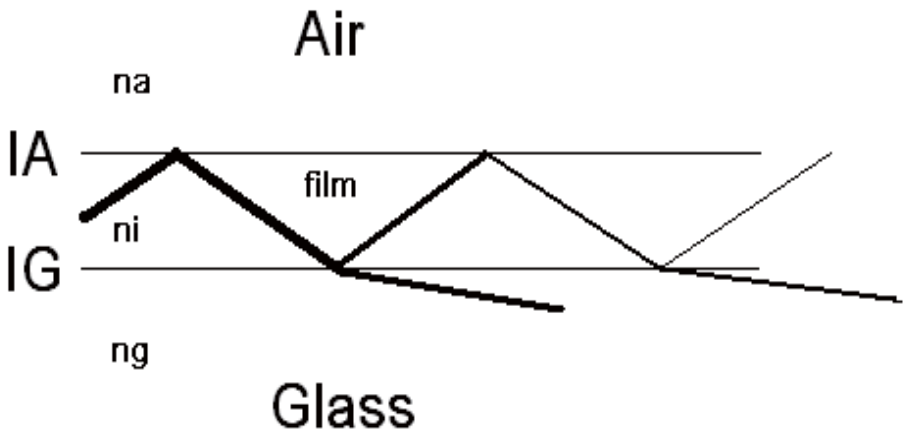

Figure 4-11 The simulated asymmetric slab waveguide modes

Figure 4-11 shows a schematic drawing of the leaky waveguide modes. The light is emitted from the organic film, and reflected or refracted at the film/air (IA) and film/glass (IG) interfaces.[22] The light that is confined in the core layer is subject to the large losses mentioned above, and does not reach the edge. However, the light that is refracted into the glass propagates in the glass with very low losses since the glass's absorption coefficient is negligible. As a consequence, the constructive and destructive interference among the rays that are refracted into the glass at grazing angles results in the observed SNEE.

The Fresnel equations for the amplitudes of the reflected TE and TM waves (r^p and r^s, respectively) and transmitted TE and TM waves (t^p and t^s, respectively) at the IG interface are

$$r_{i,g}^{p} = \frac{n_i \cos(\varphi_i) - n_g \cos(\varphi_g)}{n_i \cos(\varphi_i) + n_g \cos(\varphi_g)} \tag{2a}$$

$$r_{i,g}^{s} = \frac{n_g \cos(\varphi_i) - n_i \cos(\varphi_g)}{n_g \cos(\varphi_i) + n_i \cos(\varphi_g)} \tag{2b}$$

$$t_{i,g}^{s} = \frac{2n_g \cos(\varphi_i)}{n_g \cos(\varphi_i) + n_i \cos(\varphi_g)} \tag{2c}$$

$$t_{i,g}^{p} = \frac{2n_g \cos(\varphi_i)}{n_i \cos(\varphi_i) + n_g \cos(\varphi_g)} \tag{2d}$$

$$\phi_{path} = \frac{2d}{\cos(\varphi_i)} \times \frac{2\pi n_i}{\lambda} - 2d \tan(\varphi_i)\sin(\varphi_g)\frac{2\pi n_g}{\lambda}, \tag{2e}$$

where ϕ_{path} is the phase change between wave fronts of a directly refracted ray at the IG interface, and a ray refracted at the IG interface after reflections at the IA and IG interfaces (see Figure 4-11).

The total electric field transmission at the IG interface is

$$t = \sum_{m=0}^{\infty} t_{i,g}^{p} (r_{i,g}^{p} r_{i,a}^{p} \exp(i\phi_{path}))^m = \frac{t_{i,g}^{p}}{1 - \exp(i\phi_{path}) r_{i,g}^{p} r_{i,a}^{p}}; \tag{3}$$

Therefore, the transmitted intensity from core to glass is

$$T = \frac{n_g \cos(\varphi_g)}{n_i \cos(\varphi_i)} |t|^2 \tag{4}$$

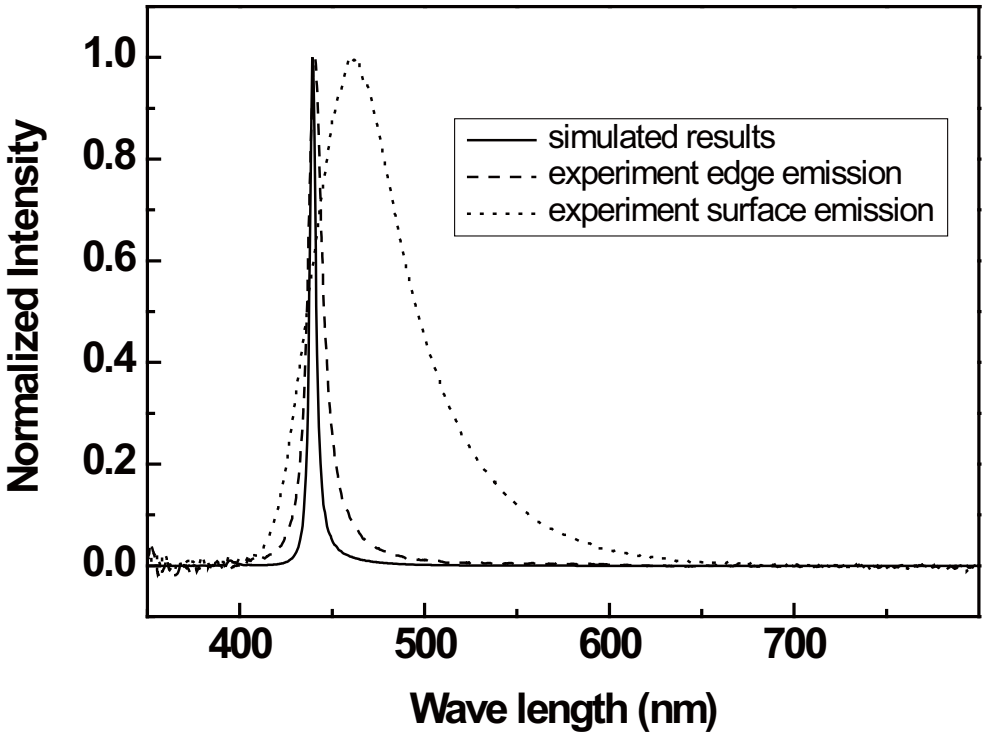

Figure 4-12 Dotted line: The surface emission spectra, which is assumed to be the spectrum of the light emitted in the organic film. Dashed line: The observed SNEE. Solid line: the simulated leaky waveguide mode spectrum.

Figure 4-12 compares the simulated spectrum with the SNEE spectrum of glass/[150 nm ITO]/[5nm CuPc]/[45 nm NPD] /[76 nm DPVBi]/[6 nm Alq3]/[2 nm CsF]/Al, assuming a grazing angle of 89°, a device length of 1 mm, and a film thickness of 284 nm. As clearly seen, the agreement is very good; the observed SNEE is slightly broader than the simulated spectrum, likely due to absorption and scattering by the Al cathode. In addition,

we note that the simulations also yield the red-shift of the peak emission with increasing film thickness. We note that the simulated spectrum broadens with device lengths below 50 μm.

4.3.9. Variable stripe length (VSL) OLED measurements of optical gain

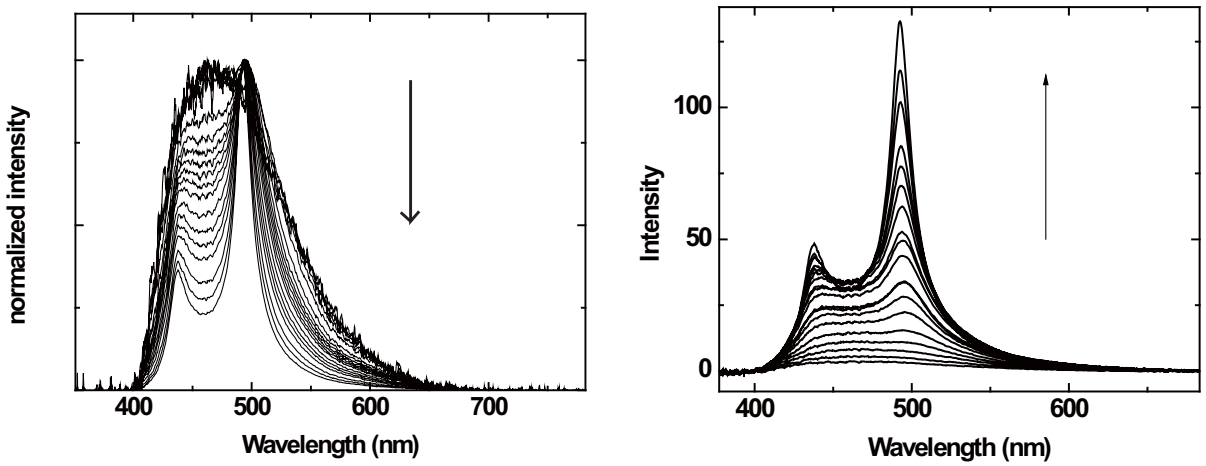

Figure 4-13 The normalized (left) and un-normalized (right) edge emission spectra from DPVBi OLEDs with stripe length from $1.5 < l < 11$ mm. The arrows indicate increasing stripe length.

Since no threshold bias or current for the SNEE could be detected, VSL measurements[9,10] of the emission were conducted on various DPVBi OLEDs, where the DPVBi layer was sandwiched between 45 nm NPD as the HTL and 8 nm Alq_3 as the ETL, to determine whether the SNEE exhibited any optical gain with increasing stripe length *l*. The Al stripe, which determined the dimensions of the OLED, was 1 mm wide and initially 11 mm long. It was subsequently cut repeatedly by 0.5 mm, and the SNEE

spectrum was measured at a constant voltage after each cut. Figure 4-13 shows all the spectra, on a normalized (left) and un-normalized (right) scale. As seen, the FWHM increases from 20 nm at 11 mm stripe length, to 122 nm at 1.5 mm stripe length. In addition, the spectrum of long stripes is much more polarized than that of short stripes, since the short-wavelength TM mode intensity increases relative to the long-wavelength TE mode as the stripe length decreases.

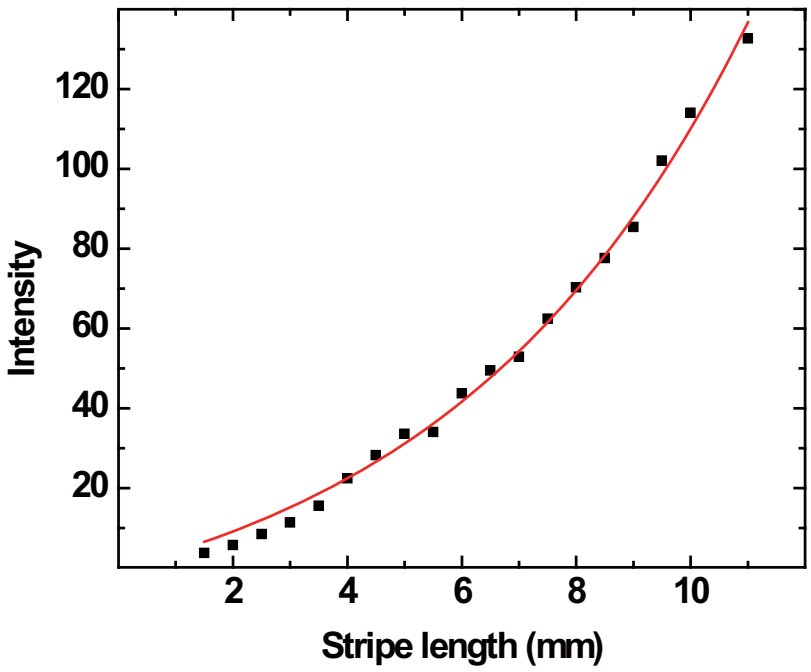

Figure 4-14 the intensity of the peak of the TE mode versus the OLED stripe length. The black squares are the experiment data, and the red curve is the fit of Eq. (5) to the data.

Figure 4-14 shows the peak intensity vs *l*. The observed agreement with the optical gain equation

$$I = \frac{A(\lambda)}{g(\lambda)}(e^{gl} - 1) \qquad (5)$$

where *A* is a constant related to the spontaneous emission coefficient. Fitting Eq. (5) to the data in Figure 4-14 yields a small gain factor g = 1.86 cm^{-1}. This small value of *g* is expected since in a low mobility device the charge-induced absorption dominates the spectral range of the optical gain profile.[4] In addition, losses due to the metal cathode also reduce the net gain.[21]

In comparing the observed VSL results to those expected under amplified spontaneous emission (ASE), we note that the latter will saturate at long *l*, because when the coherent photon density increases, the excited state population becomes increasingly exhausted and the intensity ultimately varies linearly with the stripe length.[10] Yet Figure 4-14 does not exhibit this saturation.

Figure 4-15 shows the results from another DPVBi device which was 500 μm wide and 9 mm long, and was shortened step-wise. **Figure 4-15**(a) shows the normalized edge emission spectrum for 1mm ≤ *l* ≤ 9 mm. The TM mode weakens relative to the TE mode as the stripe length increases from 1 mm to 9 mm. **Figure 4-15**(b) shows the TE mode intensity versus *l*. Fitting Eq. (5) to the data results in *g* values of 1.105, 1.596 and 1.587

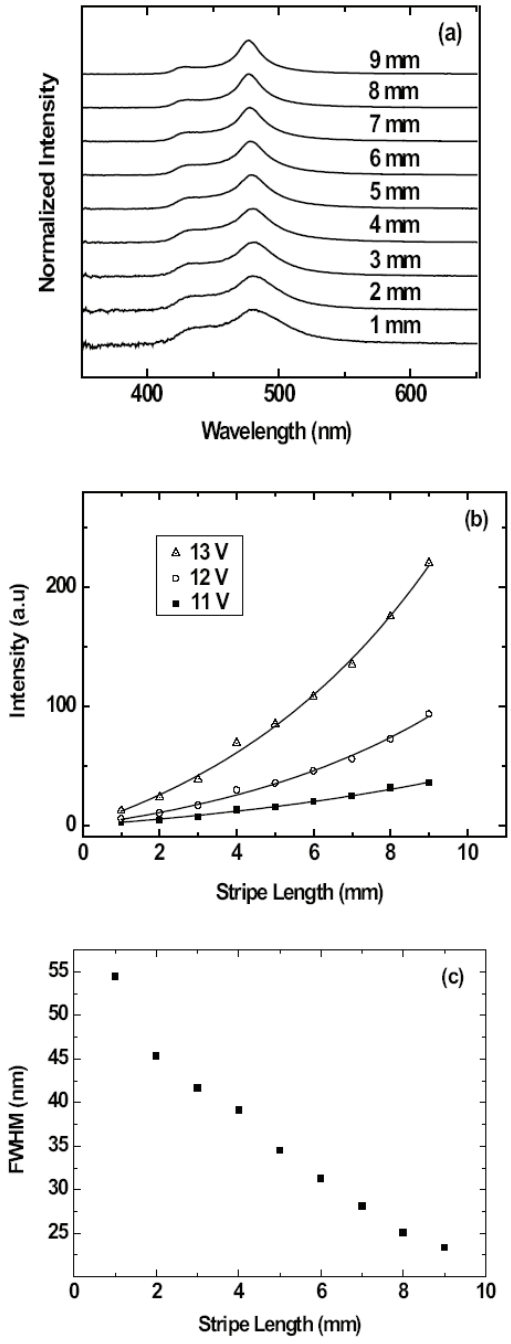

Figure 4-15 (a) Edge emission spectra vs stripe length *l*. (b) The peak TE mode edge emission intensity vs *l*. (c)The FWHM of the TE mode edge emission spectrum vs *l*.

cm^{-1} at 11 V, 12 V, and 13 V, respectively. **Figure 4-15**(c) shows the dependence of the FWHM of the TE mode on *l*. The FWHM decreased from 54.48 nm at a stripe length of 1 mm to 23.36 mm at a stripe length of 9 mm.

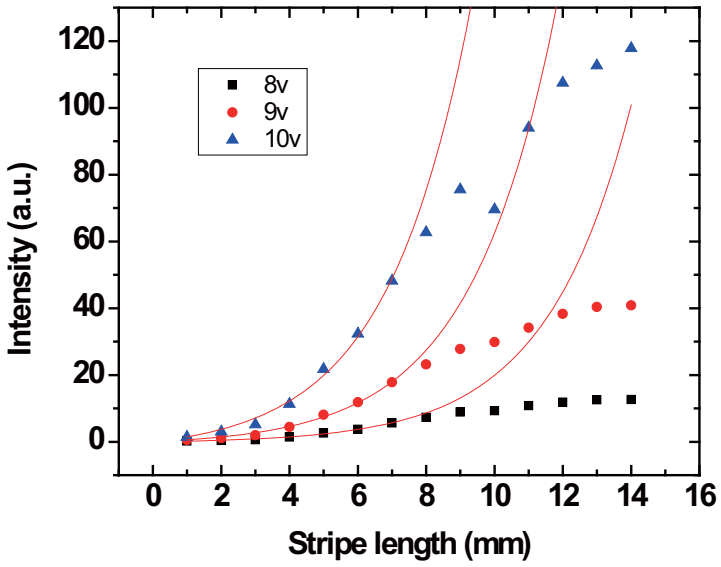

Figure 4-16 The peak edge emission intensity vs the stripe length at different voltages, the lines are the best fits of the function y = (*A*/*g*)[exp(-*g***l*)-1].

Although the saturation effect was not observed in the two OLED batches described above, that was probably due to an insufficient *l*. Figure 4-16 shows the TE mode intensity in a third OLED batch versus *l* up to *l* = 14 mm. A clear saturation phenomenon is exhibited for *l* > 9mm. Fitting Eq. (5) to the data results in *g* values of 0.403, 0.4, and 0.41 cm^{-1} at 8, 9, and 10 V, respectively. Figure 4-17 shows the dependence of the FWHM on

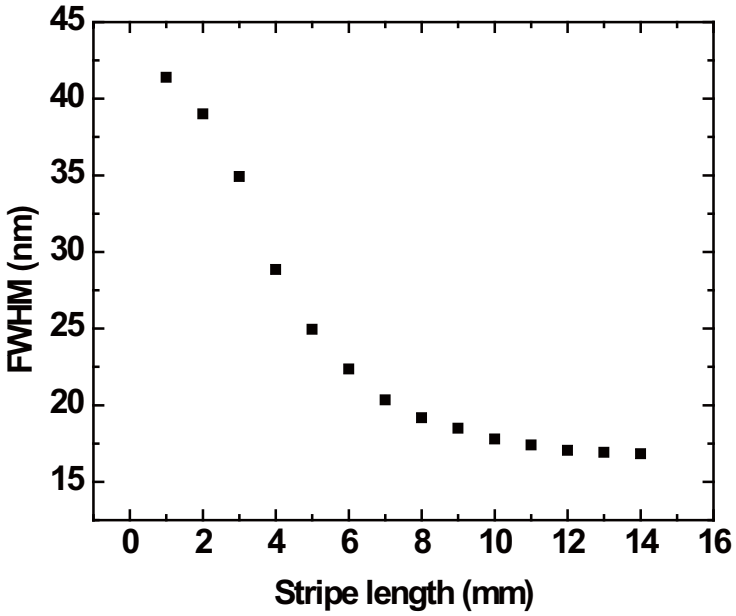

Figure 4-17 The FWHM of the TE mode edge emission spectrum vs the stripe length *l*.

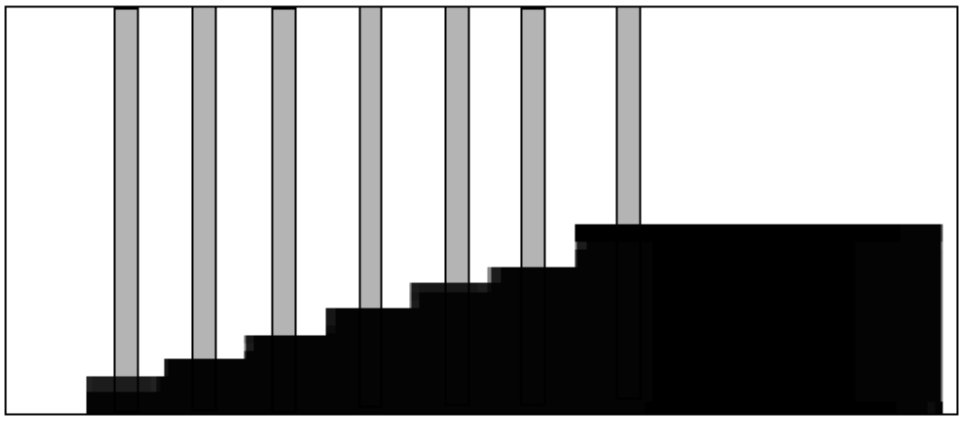

Figure 4-18 ITO layer (black area) is patterned into a staircase-type in 100 μm steps. Rectangular Aluminum cathodes (grey area) are deposited. The overlapped area defines OLED devices.

l. As clearly seen, the FWHM ~ 43 nm when the stripe length is 1 mm, and it decreases to 17.5 nm when l increases to 14 mm.

We also patterned the ITO layer into a staircase-type pattern in 100 μm steps shown in

Figure 4-18 by photolithography and wet etching. The top Al cathode was deposited through a shadow mask, which produces a rectangular Al film that overlaps with the patterned ITO to define an OLED with a certain stripe length. Figure 4-19 shows the edge emission spectra of the DPVBi OLEDs, where l is varied systematically from 100 to 600 μm. The l-dependence of these spectra is in good agreement with ASE theory in that the spectra are broad when $l \leq 400$ μm, but the FWHM decreases rapidly to only 6 – 7 nm at higher l.

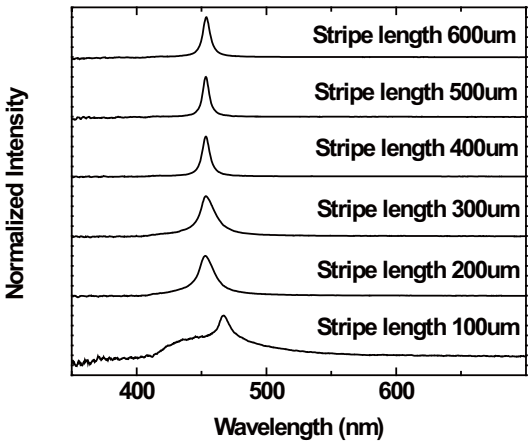

Figure 4-19 Edge emission spectra of an OLED with the device structure: glass/ITO/[5 nm CuPc]/[45 nm NPD]/[61 nm DPVBi]/[9 nm Alq3]/[1 nm CsF]/Al, the excitation stripe length *l* is varied from 100 to 600 μm.

4.3.10 Angle dependent VSL measurement

We observed the weak gain in the lateral direction. For ASE, the light emitted from the facet should be very directional, as it is from inorganic semiconductor lasers. In a vertical micro-cavity laser the light is confined in less than 1°; in a conventional diode laser, it radiates an elliptical beam, with divergence angles of 30°×10°.[23] Hence, these angle dependent VSL measurements were used to check the directionality of the light.

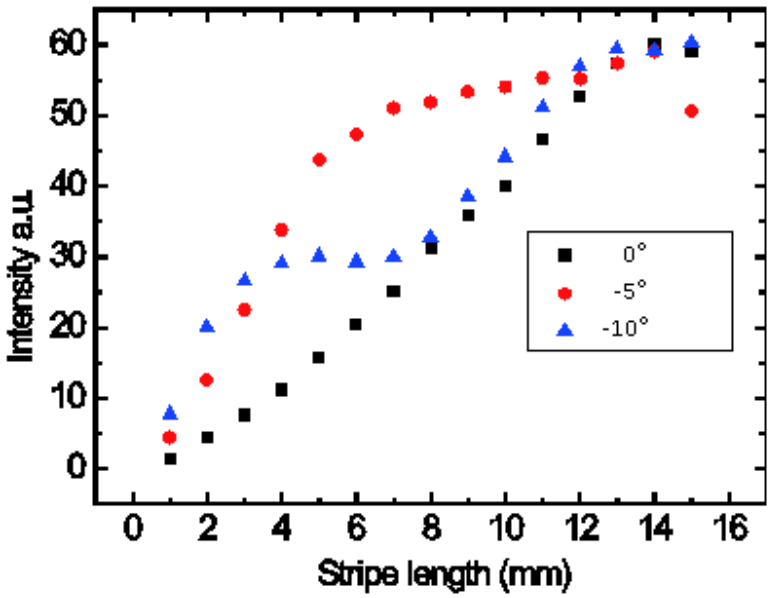

Figure 4-20 The intensity versus stripe length l at detection angles of 0°, -5°, and -10°.

The OLEDs' structure was glass/[~100 nm ITO]/[5 nm CuPc]/[45 nm NPD]/[50 nm DPVBi]/[7 nm Alq_3]/[1 nm CsF]/Al. The detection setup was shown in Figure 4-2; the resolution of the goniometer was ~0.1°. **Figure 4-20** shows that at 0°, a weak gain still appears in the superlinear curve. When the detector rotates to -5°, the intensity saturates

at about 6 mm, and at l < 6 mm, the curve appears nearly linear. At -10°, saturation occurs at shorter l. To confirm this result, a new batch of OLEDs was fabricated, and the edge emissions were detected at 0°, -2°, and -5°. The results are shown in Figure 4-21. As clearly seen, the curve at 0° was nearly identical to that shown in **Figure 4-20**. At other angles, the saturation appears at a different l, and the gain coefficient changes. In other words, the detection method and detector position affect the resulting apparent gain.

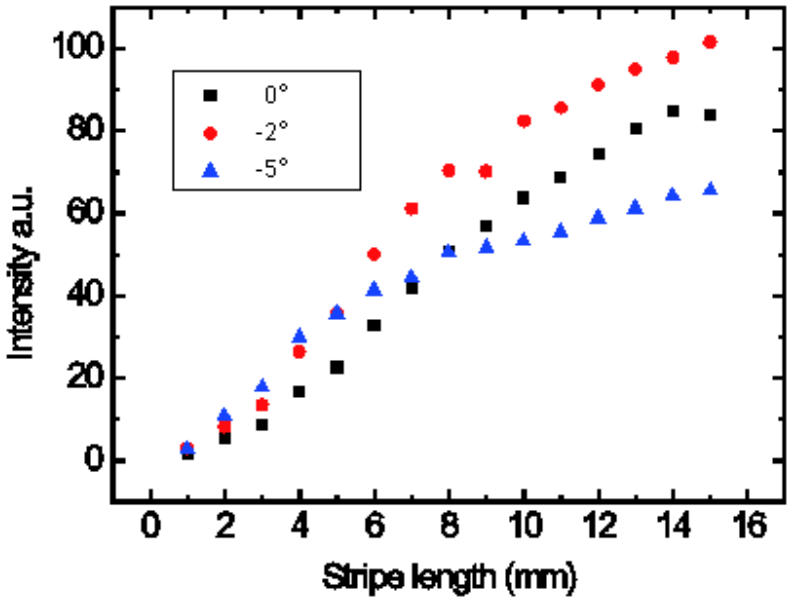

Figure 4-21 The intensity versus stripe length l at detection angles of 0°, -2°, and -5°.

Figure 4-22 shows the FWHM of the edge emission spectrum at detection angles from -25° to 60°. We note that the light emitted at a viewing angle close to 0° has a narrowed spectrum; it is attributed either to cavity effects, a leaky waveguide mode, or a cutoff waveguide mode[24].

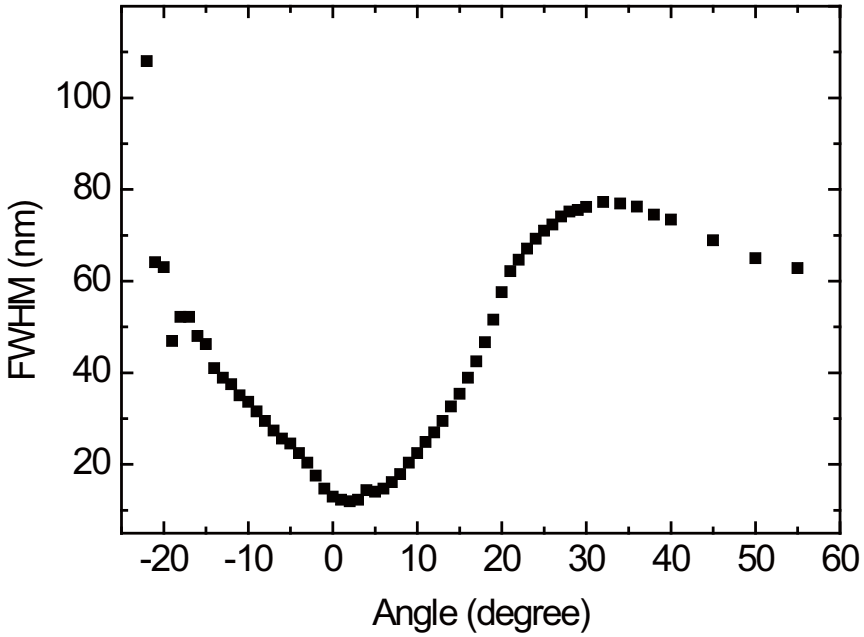

Figure 4-22. The FWHM of the edge emission spectrum at detection angles from -25° to 60°.

4.3.11. Finite difference time domain (FDTD) simulations of VSL measurements

To assess the possibility of ASE in the edge emission of the foregoing OLEDs, FDTD simulations of VSL measurements were conducted. ASE theory mandates that the spectra should be broad at short *l* and become narrower with increasing *l*, and that the intensity versus *l* should exhibit the supralinear behavior given by Eq. (5). In contrast, if a mechanism other than ASE dominates, the emission spectrum should not be affected by *l* and the intensity should increase linearly or sublinearly with *l*. Notwithstanding the effects of the emission angle demonstrated above, the observed behavior is very intriguing, since it suggests that the SNEE cannot be attributed to interference or waveguiding effects alone. The FDTD method was used to solve Maxwell's equations

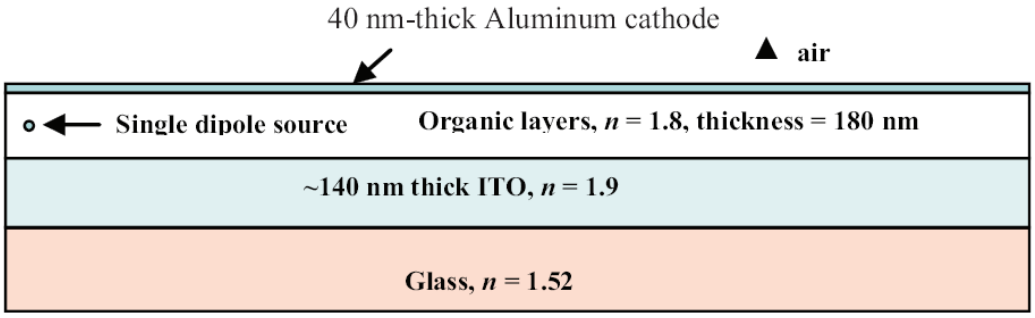

Figure 4-23 Sample geometry used in FDTD calculations.

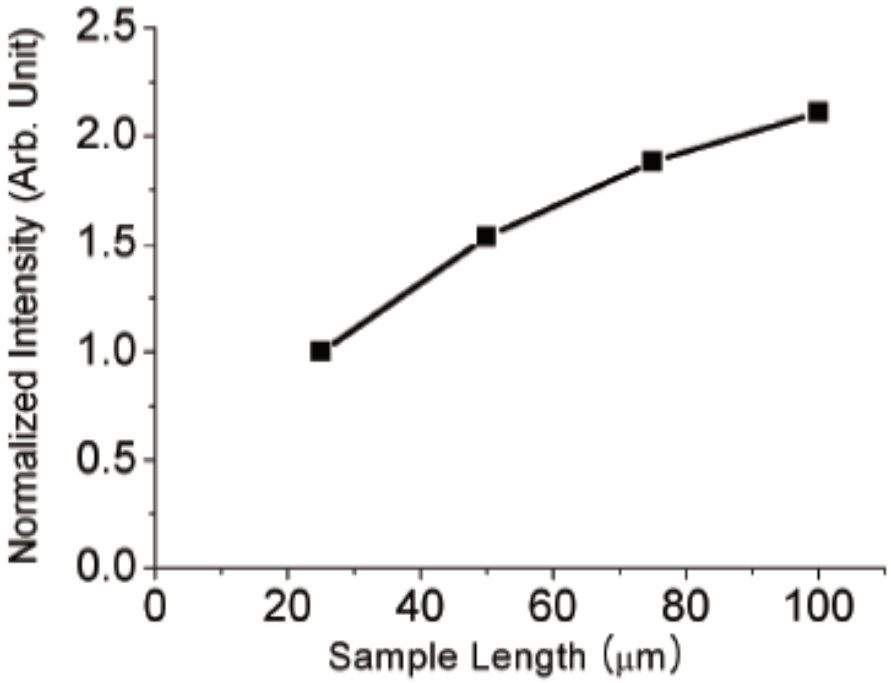

Figure 4-24 FDTD-predicted intensity of edge emission for various sample lengths.

directly in the time domain for the OLED waveguide structure.

Figure 4-23 shows the geometry used in FDTD calculations, which was [glass (n = 1.52, 0.7 mm thick)]/[ITO (n = 1.9, 140 nm thick)]/[organic layers (n = 1.8, 180 nm thick)]/[Al cathode (40 nm thick)]. Since the thickness of the glass substrate was ~0.7 mm, in the simulations we attached a perfectly matched layer (PML) below a thin (360 nm) glass to completely absorb any incident light so that the glass is effectively infinitely thick. We used a single TE polarized (E field pointing out of the sheet) dipole source, and pulsed excitation, and collected the time trace of the edge emission, to obtain the emission spectrum by taking the fast Fourier transform (FFT) of the time trace. The simulation focused on the edge emission from the glass edge near the ITO/glass interface. We calculated the edge emission spectrum, assuming no optical gain, by setting the distance between the dipole source and the measuring position to be 25, 50, 75, and 100 μm. Figure 4-24 clearly demonstrates that without optical gain, the behavior is sublinear. The observed behavior also rules out the possibility of superfluorescence and biexcitonic spontaneous emission. To uncover the nature of the emission spectra, we ran the FDTD simulations with a monochromatic cw dipole excitation at λ= 493, 448, and 372 nm. The electric field intensity profiles of the three cases are shown in

Figure **4-25**. It clearly demonstrated that the mode causing the SNEE is a leaky mode: away from the peak, the modes are confined to the organic and ITO regions.

Figure **4-26** is a zoomed image of

Figure **4-25**, where black horizontal lines divide the polymer, ITO, and glass regions. The simulation also indicated that the waveguiding effect can induce a SNEE with certain device sizes, in agreement with the interference simulations described in Sec. 3.8 above.

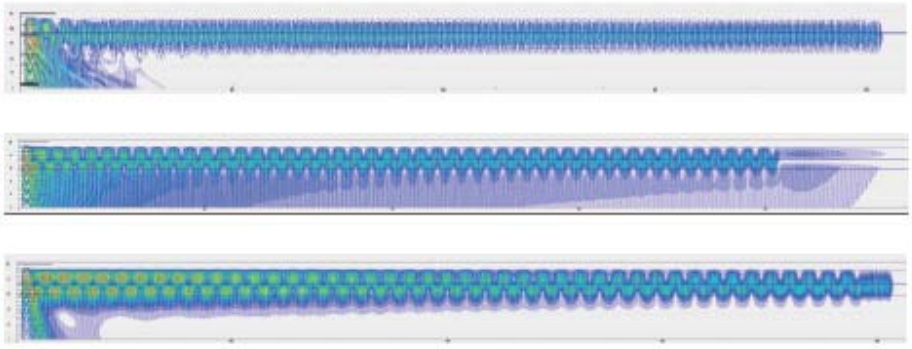

Figure 4-25 Intensity profiles of modes excited at (a) top: λ= 493 nm, (b) center: λ= 448 nm, and (c) bottom: λ=372 nm.

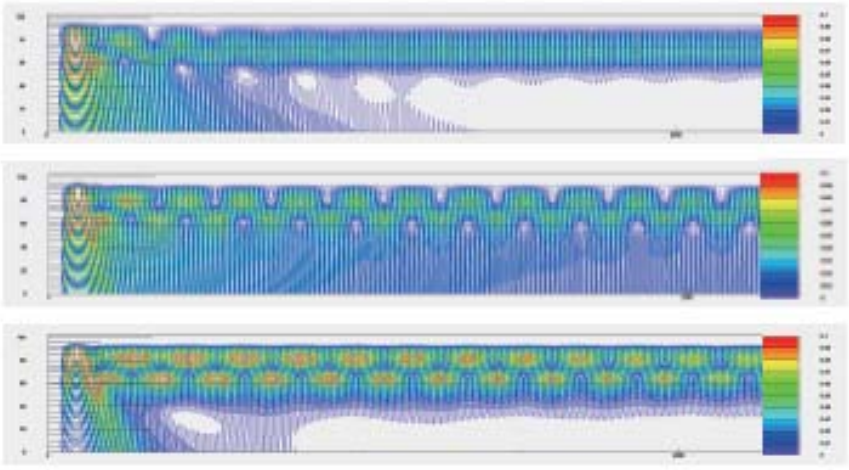

Figure 4-26. Zoomed images of the left (origin) side of **Figure 4-25**

4.3.12. Issues related to the analysis of VSL measurements

Although VSL measurements are a powerful method to demonstrate optical gain, some critical points must be considered.[9,10] When g is low, this method is valid only if (a) the gain and pump intensity are homogeneous over l and (b) the detector collection efficiency η is independent of l. While condition (a) was likely satisfied in these VSL measurements, it is not clear if condition (b) was satisfied as well: In this work, η of the emitted light was limited by the numerical aperture of the optical fiber.[25] It can be argued that when the optical axis of the waveguide is not aligned with respect to the optical axis of the collecting lens, or when the focal plane of the objective is positioned well within the sample, a supralinear curve can be observed in VSL measurements without an actual optical gain. As we saw in Sec. 3.10, the direction angle of the detector does have an effect on the gain. And since we cannot determine if the axes were adequately aligned, it is not clear that the strong dependence of the TE and TM modes (see Figure 4-13) on l is or is not due to misaligned axes.[26]

4.3.13 EL Decay time τ measurements of Phosphorescent OLED

In a laser gain medium, amplification is associated with the population of an excited state, from which stimulated emission can occur. Without the stimulated emission, the lifetime of the upper level population is finite due to spontaneous emission or additional quenching effects. Typically the upper state population decays exponentially with a

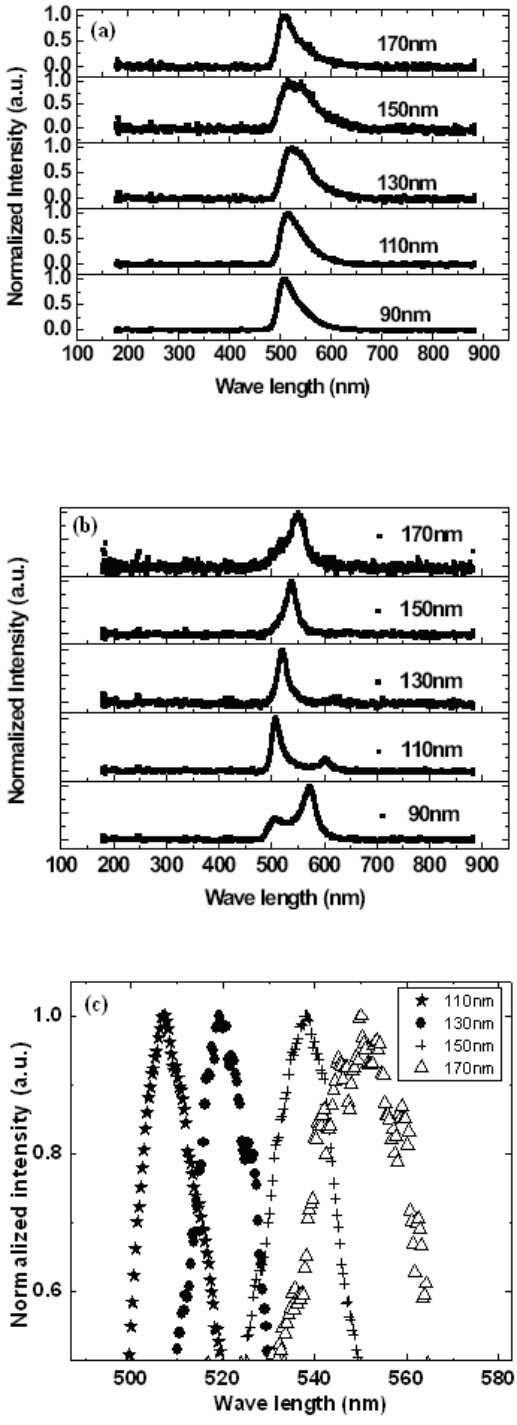

Figure 4-27 (a) Surface and (b) edge emission spectra of Ir(ppy)3 OLEDs with various emitting layer thicknesses. (c) The magnification of the edge emission spectra

certain decay time τ, and τ will decrease significantly if stimulated emission occurs. Thus a decrease in τ provides strong evidence for ASE.

For fluorescent materials and OLEDs, $\tau \sim 1$ ns, so the stimulated emission decay time will be shorter. Since our temporal resolution was > 20 ns, we fabricated phosphorescent OLEDs, where τ is much longer. For example, for PtOEP $\tau \sim 100$ μs; for $Ir(ppy)_3$ $\tau \sim 0.5$ μs when doped into 4,4'-bis(9-carbazolyl)biphenyl (CBP); for other phosphorescent dyes, τ is generally in the ~0.1 to ~1000 μs range.

In light of the foregoing considerations, an $Ir(ppy)_3$ phosphorescent OLEDs were fabricated and studied. Their structure was glass / [150 nm ITO] / [5nm CuPc] / [60 nm NPD] / [90, 110, 130, 150, or 170 nm CBP doped with $Ir(ppy)_3$] / [50 nm BCP] / [1 nm CsF] / Al. These devices were relatively thick, because, as mentioned above, the critical thickness for a device emitting at longer wavelength is thicker than for that emitting at shorter wavelength.

Figure 4-27(a) shows the surface emission spectra of $Ir(ppy)_3$ OLEDs. The peak positions and the shape of the spectra are almost the same regardless of thickness. The minor changes in the shape result from the weak vertical microcavity effect as discussed above.

Figure 4-27(b) shows the edge emission spectra. As clearly seen, their behavior is similar to those from the fluorescent OLEDs: Their spectral narrowing, the alternation of the TE TM modes, and the red shift of the narrow peak are all similar to those of the fluorescent devices.

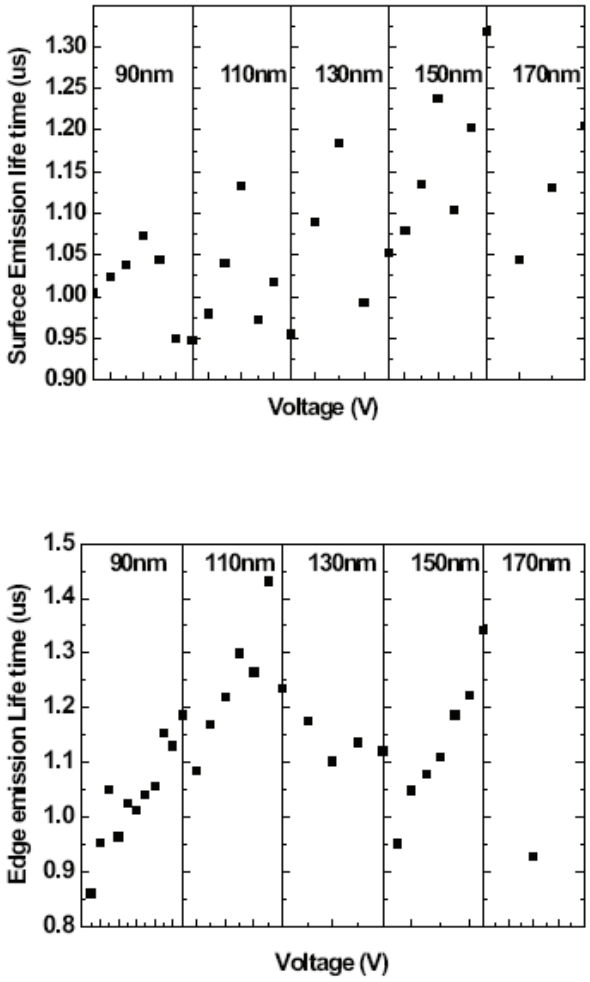

Figure 4-28 (a) Surface and (b) edge emission decay time of Ir(ppy)3 OLEDs with different emitting layer thicknesses at different bias.

Figure 4-27(c) is a magnification of

Figure 4-27(b). The red shift of the narrowed peak above the critical thickness is clear, and the FWHM of the peaks is ~20 nm. Although the narrowed emission bands are not as narrow as fluorescent OLEDs, their FWHM is only about half of the surface emission bands.

The phosphorescent OLEDs' τ was measured using a PMT. Figure 4-28(a) shows τ of the surface emission from 35 to 55 V; it clearly "oscillates" around 1 μs. Figure 4-28(b) shows τ of the edge emission, and it is also ~1 μs. In other words, no clear reduction in τ from the surface to the edge emission, or vs voltage, is observed. However, in the devices with 90, 110, and 150 nm emission layer, τ slightly *increases* with increasing voltage, i.e., contrary to the behavior expected with the onset of ASE.

Iridium(III)bis[4,6-di-fluorophenyl-pyridinato-N,$C^{2'}$]picolinate (FIrpic) is another widely used phosphorescent material.[27] Its τ is ~1 μs, and its emission peaks at ~470 nm, i.e., close to that of the fluorescent material DPVBi. We therefore fabricated Firpic-based OLEDs as well, with the structure Glass / [150 nm ITO] / [5nm CuPc] / [35 nm NPD] / [50, 60 , 70 , 80 nm FIrpic-doped CBP] / [30 nm BCP] / [6 nm Alq_3] / [1 nm CsF] / Al. Figure 4-29(a) shows the surface emission of the devices. It peaks at 480 nm, i.e., slightly longer than the intrinsic peak of the material; this is due to a weak microcavity effect.

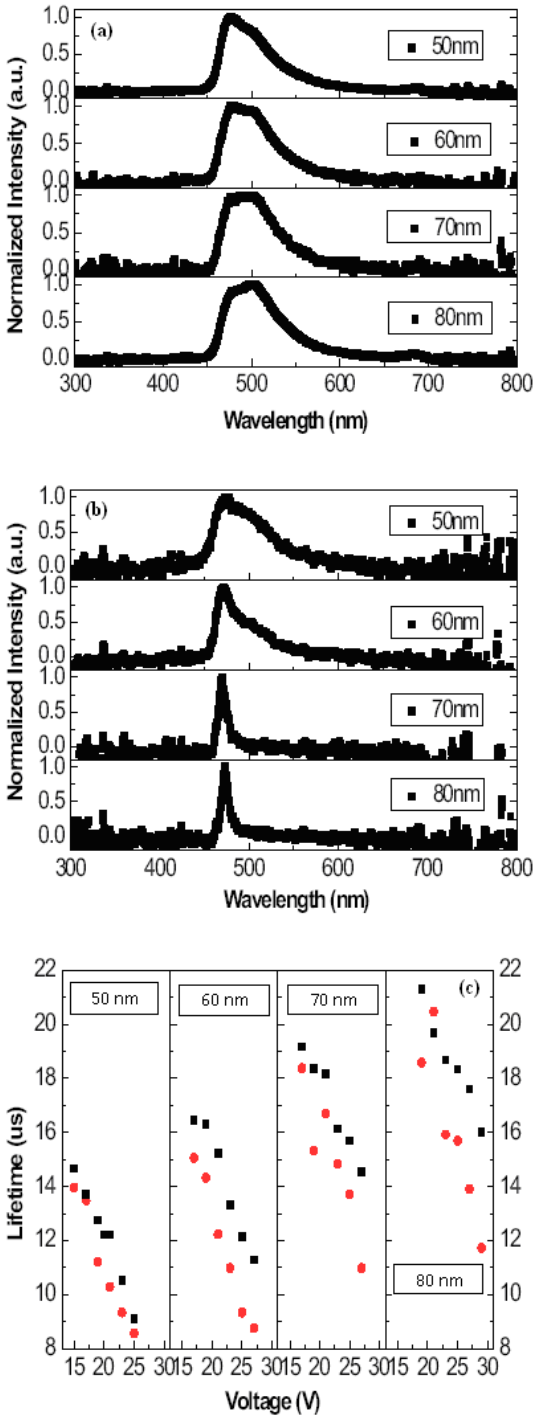

Figure 4-29 (a)Surface and (b) edge emission spectra of FIrpic OLEDs with different thicknesses. (c) The lifetime of the edge (dot) and surface (square) emission.

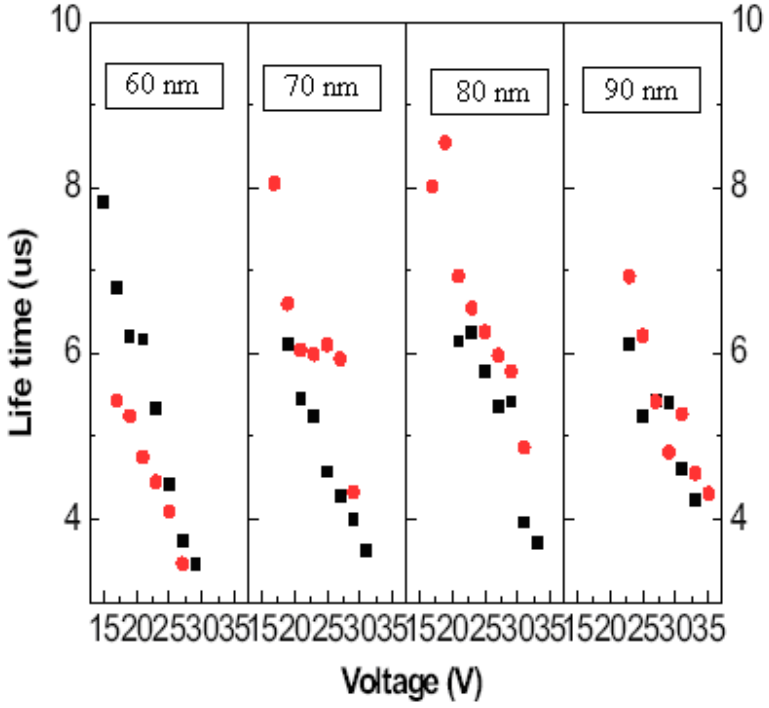

Figure 4-30 The lifetime of the surface (square) and edge (dot) emission of OLEDs with the same nominal structures as those of
Figure 4-29.

Figure **4-29**(b) shows the edge emission of these devices. The critical thickness required for the narrow edge emission is ~70 nm. The FWHM of the narrow edge emission is ~15 nm, which is less than half of the surface emission.

Figure 4-29(c) shows the τ of the devices. For all of them, τ decreases with increasing voltage, and the values for the edge emission are slightly lower than those for the surface emission. While this behavior is consistent with an ASE contribution, it should not occur in the surface emission. However, since we were not able to measure the τ of the surface and edge emission simultaneously (the edge emission was measured after the surface emission), the degradation of the devices may have affected τ. Thus, a new batch of

OLEDs with the same structure was fabricated, and this time the edge emission was measured first. Figure 4-30 compares the surface and edge emission of this batch. As clearly seen, there is no significant difference between the τ's, and in most of them, the edge emission τ is actually slightly longer than the surface emission. This confirms that the differences in τ are due to the degradation of the devices.

4.4. Summary

In summary, the SNEE from SMOLEDs was described, and shown to result from leaky waveguide modes that leak into the glass substrate and propagate out of the glass edge at a grazing angle; the threshold thickness for the SNEE was shown to depend on absorption by the metal cathode. VSL measurements of the SNEE yielded some key features of ASE, but no threshold bias or current. Interference and FDTD simulations confirmed the leaky waveguide mode nature of the SNEE, but could not account for the apparent weak optical gain. The possibility that the apparent weak optical gain is due to misalignment between the optical axes of the waveguide and that of the collection lens of the detector was also considered, but it is not clear if it can account for the observed evolution of the SNEE spectra with l. The EL decay times τ of the surface and edge emission of phosphorescent OLEDs were also measured, and were also consistent with the absence of any significant ASE.

Acknowledgements

Ames Laboratory is operated by Iowa State University for the US Department of Energy (USDOE) under Contract No. DE-AC 02-07CH11358. The work in Ames was supported by the Director for Energy Research, Office of Basic Energy Sciences, USDOE. The work in Korea was supported in part by q-Psi/KOSEF and the Seoul R&BD Program.

REFERENCES

1. G. Kranzelbinder and G Leising, Rept. Prog. Phys. **63**, 729 (2000).
2. V. G. Kozlov, P. E. Burrows, G. Parthasarathy, and S. R. Forrest, Appl. Phys. Lett. **74**, 1057 (1999).
3. N. Tessler, D. J. Pinner, V. Cleave, D. S. Thomas, G. Yahioglu, and P. Le Barny, Appl. Phys. Lett. **74**, 2764 (1999).
4. N. Tessler, Adv. Mater. **11**, 363 (1999).
5. M. A. Baldo, R. J. Holmes, and S. R. Forrest, Phys. Rev. B **66**, 035321 (2002).
6. H. Yamamoto, T. Oyamada, H. Sasabe, and C. Adachi, Appl. Phys. Lett. **84**, 1401 (2004).
7. Yun Tian, Zhengqing Gan, Zhaoqun Zhou, Ji-hun Kang, Q-Han Park, David W. Lynch, and Joseph Shinar, arXiv.org: cond-mat/0701312 (2007).
8. Y. Tian, Z. Gan, Z. Zhou, D. W. Lynch, J. Shinar, J.-h. Kang, and Q.-H. Park, Appl. Phys. Lett. **91**, 1 (2007).
9. K. L. Shaklee and R. F. Leheny, Appl. Phys. Lett. **18**, 475 (1971).
10. M. D. McGehee, R. Gupta, S. Veenstra, E. K. Miller, M. A. Diaz-Garcia, and A. J. Heeger, Phys. Rev. B **58**, 7035 (1998).
11. L. Zou, V. Savvate'ev, J. Booher, C. H. Kim, and J. Shinar, Appl. Phys. Lett. **79**, 2282 (2001).

12. K. O. Cheon and J. Shinar, Appl. Phys. Lett. 81,1738 (2002).

13. G. Li, C. H. Kim, Z. Zhou, J. Shinar, K. Okumoto, and Y. Shirota, Appl. Phys. Lett. **88**, 253505 (2006).

14. G. E. Jabbour, B. Kippelen, N. R. Armstrong, and N. Peyghambarian, Appl. Phys. Lett. **73**, 1185 (1998).

15. M. Y. Chan, S. L. Lai, M. K. Fung, C. S. Lee, and S. T. Lee, J. Appl. Phys. **95**, 5397 (2004).

16. V. Bulovic, V. B. Khalfin, G. Gu, and P. E. Burrows, Phys. Rev. B **58**, 3730 (1998).

17. M. D. McGehee and A. J. Heeger, Adv. Mater. **12**, 1655 (2000).

18. T. D. Visser and H. Blok, IEEE J. Quant. Elec. **33**, 10 (1997).

19. Ogusu, Kazuhiko, Miyagi; Mitsunobu, Nishida, Shigeo, J. Opt. Soc. Am 70,48 (1980)

20. I. Pelant, T. Ostatnicky, J. Valenta, K. Luterova, K. Luterova, E. Skopalova, T. Mates, and R. G. Elliman, Appl. Phys. B **83**, 87 (2006).

21. N. Tessler and R.H. Friend, Syn. Met. **102**, 1122 (1999).

22. F. Li, O. Solomesch, P. R. Mackie, D. Cupertino, and Nir Tessler, J. Appl. Phys **99**, 013101 (2006).

23. D. K. Mynbaev and L. L. Scheiner, *Fiber-Optic Communications Technology* (Prentice Hall, New Jersey, 2001).

24. D. Marcuse, Theory of Dielectric Optical Waveguides, 2nd ed. (Academic, San Diego, 1991)

25. L. Dal Negro, P. Bettotti, M. Cazzanelli, D. Pacifici, and L. Pavesi, Optics Comm. **229**, 337 (2004).

26. L. Pavesi, S. Gaponenko, and L. D. Negro, *Towards the First Silicon Laser* (Kluwer Academic Publishers, Netherlands, 2003).

27. C. Adachi, R. C. Kwong, P. Djurovich, V. Adamovich, M. A. Baldo, M. E. Thompson, and S. R. Forrest, Appl. Phys. Lett. **79**, 2082 (2001).

CHAPTER 5 TRANSIENT ELECTROLUMINESCENCE DYNAMICS IN SMALL MOLECULAR OLEDS

Zhengqing Gan,[1] Rui Liu,[1] Ruth Shinar,[2] and Joseph Shinar[1*]

[1]*Ames Laboratory – USDOE and Department of Physics and Astronomy, Iowa State University, Ames, IA 50011*

[2]*Microelectronics Research Center and Department of Electrical and Computer Engineering, Iowa State University, Ames, IA 50011*

*Corresponding author: jshinar@iastate.edu

Organic light emitting diodes (OLEDs), photodetectors, and solar cells are attracting extensive interest due to attributes such as low-cost and flexible size and design. These attributes, and the continued expansion in organic electronics R&D, have resulted in interest in novel devices such as OLED- and transistor-based (bio)chemical sensors and biotechnology.[1,2] Small molecular OLEDs (SMOLEDs) dominate OLED applications, but fundamental processes that affect their performance, e.g., carrier dynamics and electroluminescence (EL)-quenching processes, are not adequately understood. This communication addresses these processes via transient EL studies of SMOLEDs based on materials and designs used in cutting-edge devices.[3-6]The results shed new light on the strong role of materials and device architecture in charge trapping, field-induced quenching, and carrier drift within and beyond the recombination zone (RZ). This role is

manifest in the strong dependence of EL "spikes" and tails extending to several μs, following a pulsed bias, on the materials and device architecture.

A typical SMOLED consists of amorphous thermally-evaporated layers sandwiched between two electrodes.[1,3-5] When a bias is applied to the device, holes h^+ and electrons e^- are injected from the electrodes into the h^+ and e^- injection layers (HIL and EIL, respectively), from which they drift into the h^+ and e^- transport layers (HTL and ETL, respectively) and into the RZ. Most then recombine to excitons, a fraction of which decays radiatively.

Previous studies focused almost exclusively on OLEDs under DC voltage.[7-9] A few transient EL studies of polymer LEDs (PLEDs)[10-12] and 4,4'-bis(2,2'-diphenylvinyl)-1,1'-biphenyl (DPVBi)-based SMOLEDs,[13-15] reported intriguing EL spikes following a bias pulse. Other studies, e.g., on anthracene-based SMOLEDs, reported no such spikes.[16,17]

This communication details the major processes, following a voltage pulse, that appear to be universal in SMOLEDs. Depending on the materials and the SMOLED's structure, these processes may result in EL spikes at 100–300 ns,[18] and, in any case, an EL tail extending over several μs. Experiments and simulations show that trapped carriers generate correlated charge pairs (CCPs) that are the major contributor to the spikes. The recombination of initially unpaired charges, generates the μs-long emission tail; emission due to triplet-triplet annihilation is detected in and beyond the μs range.[16,17] The strong effect of the HIL, whether copper phthalocyanine (CuPc), molybdenum oxide (MoO_3), or absent, and of the ETL, whether DPVBi, tris(8-hydroxyquinoline) Al (Alq_3), or 4,7-diphenyl-1,10-phenanthroline (BPhen), and the behavior under reverse bias and at low temperatures, are central to understanding the spikes.

Arrays of 21×21 OLED pixels (pixel diameter ~1.5 mm) were fabricated combinatorially.[19] Figure 5-1 shows the room temperature (RT) transient EL of various Alq_3-based devices. As seen, the strongest spikes (Figure 5-1(a)) were observed in a Coumarin 6 (C6)-doped device devoid of an HIL, i.e., ITO/*N,N*'-bis(naphthalen-1-yl)-*N,N*'-bis(phenyl)benzidine (α-NPB)/doped-Alq_3/Alq_3/LiF/Al. A strong spike is also seen in ITO/CuPc/α-NPB/doped-Alq_3/Alq_3/LiF/Al (Figure 5-1(b)). Similar spikes and tails were also observed in rubrene-doped Alq_3, *fac* tris(2-phenylpyridine) Ir [Ir(ppy3)]-doped 4,4'-Bis(9-carbazolyl) biphenyl (CBP), and Ir(III)bis[4,6-di-fluorophenyl)-pyridinato-*N*,$C^{2'}$]picolinate (FIrpic)-doped CBP SMOLEDs, with a CuPc HIL.[20] However, adding BPhen as a h^+ blocking layer (HBL) (i.e., ITO/CuPc/α-NPB/doped-Alq_3/Alq_3/BPhen/LiF/Al) strongly reduced the spike (Figure 5-1(c)). Also, undoped ITO/CuPc/α-NPB/Alq_3/LiF/Al devices exhibited very weak spikes (Figure 5-1(d)). Additionally, the spike is eliminated when CuPc is replaced by MoO_3 (Figure 5-1(e)), as is also the case when BPhen is added (Figure 5-1(f)). In summary, Figure 5-1 shows that the necessary conditions for strong RT spikes are (i) a high h^+ injection barrier (e.g., no HIL or a CuPc HIL), (ii) an RZ with a carrier-trapping dopant (e.g., C6, $Ir(ppy)_3$, or FIrpic), and (iii) the absence of a HBL such as BPhen.

Figure 5-2 shows the RT transient EL at reverse, 0, and forward bias (-4, 0, and 4 V). As seen, the spike narrows and shifts from 110 to 70 ns as the bias reverses from 0 to –4 V.

Figure 5-3 shows the transient EL of undoped and C6-doped Alq_3 in ITO/CuPc/α-NPB/Alq_3/LiF/Al devices at temperatures $40 \leq T \leq 300$ K. As seen, the spike amplitude

increases strongly with decreasing temperature, but the peak shifts only slightly to longer times.[18]

This communication indicates that the following processes are largely responsible for the observed transient EL:

1) Carriers are still injected into the device during the falling edge of the pulse, which lasted for ≤50 ns, depending on the time constant of the measurement.[18] The decaying external field also continues to drive the preexisting carriers (i.e., those present at t=0) towards the RZ. The exciton formation rate $(dN_{exc}/dt)_J$ due to these carriers is proportional to the injection-limited current density J,[3,5]

$$(dN_{exc}/dt)_J \propto J \propto V(t)^2 \exp(-b/V(t)). \quad (1).$$

The observed EL amplitude generated from these excitons, as well as from preexisting excitons and CCPs, is similar to the DC level (not shown). This ~50 ns period is indeed comparable to the electrode-to-RZ carrier transit time.[21]

2) CCPs present at t~50 ns ("initial CCPs") continue to recombine to excitons at a rate $R_{ccp}(t)$. It is simulated as a random walk, subject to Coulomb attraction, of the untrapped carrier toward the trapped carrier (localized on the guest):[22]

$$R_{ccp}(t) = \frac{\sqrt{4\pi}}{\sqrt{D_{ccp}}} \frac{r_c}{t^{3/2}} \int_0^\infty g(r_0) \exp\left(-\frac{r_0^2}{4D_{ccp}t}\right) \exp\left(-\frac{r_c}{r_0}\left(1 - \mathrm{erf}\left(\frac{r_0}{\sqrt{4D_{ccp}t}}\right)\right)\right) r_0^2 \, dr_0 \quad (2).$$

where

$$g(r_0) = \frac{\exp\left(-\frac{(r_0-\bar{r})^2}{\sigma^2}\right)}{4\pi^{3/2}\sigma\bar{r}^2}, \quad (3).$$

D_{ccp} is the diffusivity within the CCP, $r_c \approx 19$ nm is the RT Onsager radius[15] (neglecting screening by other charges; <<19 nm if not), r_0 is the e^--h^+ separation within the CCP, $\bar{r}$ is the average of r_0, and σ is the r_0 distribution width. *Eq. (2) yields the spikes*.

After the bias pulse, the CCPs continue to recombine to excitons, and simultaneously, carriers detrapped from shallow host traps with rate R_{detrap} (discussed later) form CCPs whose-recombination rate also follows Eq. (2). Thus the overall CCP rate equation is

$$dN_{ccp}(t)/dt = N_t(E_t,t)R_{detrap} - N_{ccp0}R_{ccp}(t) - \int_0^t N_t(E_t,t')R_{detrap}R_{ccp}(t-t')dt \quad (4).$$

where N_{ccp0} is the initial CCP density. The first term is the source of new CCPs; the second and last terms are due to the recombination of the initial CCPs and those created by detrapped carriers at $t=t'$, respectively.

3) The HOMO and LUMO tail states are due to impurities and structural disorder, believed to result in an e^- tail state density[23,24]

$$N_t(E_t) = (\frac{N_{tot}}{kT_c})\exp(\frac{E_t - E_{LUMO}}{kT_c}), \quad (5).$$

with a similar expression for h^+ tail states. N_{tot} is the total trap density and kT_c is the characteristic trapping energy. The detrapping probability per second is then given by [25]

$$p(E_t) = \theta \exp(-(E_{LUMO} - E_t)/kT) \quad (6).$$

where θ is the attempt frequency. Hence,

$$R_{detrap} = \frac{dN_t(E_t,t)/dt}{N_t(E_t,t)} = -\frac{N_t(E_t,t)p(E_t)}{N_t(E_t,t)} = -1/\tau_t(E_t) \quad (7).$$

Here $\tau_t(E_t) \equiv 1/p(E_t)$ is the characteristic residence time in trap level E_t. The density of trapped charges $N_t(E_t,t)$ is then

$$N_t(E_t, t) = N_t(E_t, 0)\exp\left(-\frac{t}{\tau_t(E_t)}\right). \quad (8).$$

In the typical host there is a broad distribution of trap levels ranging from ~0.06 eV to > 0.5 eV.[26] Hence, the total density of trapped charges is given by a stretched exponential:[27,28]

$$N_t(t) = N_t(0)\exp\left(-(t/\tau_{ucc})^{\beta}\right) \quad (9).$$

β is the stretching factor that quantifies the distribution width of the occupied trapping energies, and τ_{ucc} is the total time the carrier remains uncorrelated. The excitons generated from these charges yield the observed μs-long EL tails.

The observed EL decay is due to the exponential radiative decay of the singlet excitons (SEs) at a rate $1/\tau_{SE}$. The preexisting SEs can be neglected as their lifetime is <10 ns. New SEs are produced by CCP recombination at t>0. This SE formation rate is thus given by combining Eqs. (1) and (4)

$$\frac{dN_{SE}}{dt} \propto \left(\frac{dN_{exc}}{dt}\right)_J + N_{ccp0}R_{ccp}(t) + \int_0^t N_t(E_t, t')R_{detrap}R_{ccp}(t-t')dt' - \frac{N_{SE}}{\tau_{SE}} \quad (10).$$

Solving this differential equation yields

$$N_{SE}(t) = exp\left(-\frac{t}{\tau_{SE}}\right)\int_0^t \left(\frac{dN_{exc}}{dt}\right)_J exp\left(\frac{t'}{\tau_{SE}}\right)dt' + N_{ccp0}\, exp\left(-\frac{t}{\tau_{SE}}\right)\int_0^t R_{ccp}(t')\, exp\left(\frac{t'}{\tau_{SE}}\right)dt' + exp\left(-\frac{t}{\tau_{SE}}\right)\int_0^t exp\left(\frac{t'}{\tau_{SE}}\right)\left[\int_0^{t'} N_t(E_t, s)R_{detrap}R_{ccp}(t' - s)ds\right]dt' \quad (11).$$

The first, second, and third terms are due to excitons generated from the carriers injected at $0 \le t \le 50$ ns, to initial CCPs, and to uncorrelated carriers at $t > 50$ ns, respectively. Therefore, in the second and third terms the $t=0$ lower limit of integration corresponds to $t=50$ ns in the experiments.[18,29] Due to the fast decay of the SEs and the recombination of CCPs, the third term of Eq. (11) is approximated by Eq. (9).[30]

As seen in Figures.5-1~5-3, the model is in good agreement with the observed behavior. In particular, the agreement is better than that obtained previously using a CCP+Langevin recombination model.[15]

Fitting Eq. (11) for ITO/CuPc/α-NPB/C6-doped Alq_3/Alq_3/LiF/Al devices yielded the SE decay time τ_{SE}=8.7 ns, consistent with the C6 radiative lifetime τ_{rad}<10 ns;[11,31] this value was then used in all other fits. The other fitting parameters ranged over the following values: D_{ccp}~(7×10^{-13}-5×10^{-11} m^2/s), σ~(0.9-4.6 nm), $\bar{r}$~(0.9-3 nm), τ_{ucc}~(1–5 μs), depending on the doped-layer thickness, the bias, and the temperature. Their behavior will be detailed elsewhere.[20]

It has been suggested that a ms-long transient EL tail is due to triplet-triplet annihilation to SEs.[16] However, the tail's microsecond component is dependent on the

bias following the pulse (Figure 5-2), consistent with recombination of uncorrelated charges.

The occurrence of spikes with amplitudes exceeding the DC EL level is intriguing and its understanding remains a challenge. The observation that a carrier-trapping guest is required for a RT spike (Figure 5-1(a)–Figure 5-1(c) vs Figure 5-1(d) and unpublished[20]) indicates that the density of carriers trapped in the RZ must be sufficiently high. As the temperature is lowered, more carriers become trapped in shallow traps in the RZ, and indeed the spike amplitude increases (Figure 5-3). However, Figure 5-1 also shows that this requirement is not sufficient. We suggest that the spike results from either or both of the following mechanisms after the bias is turned off: (*i*) reduced field-induced SE and CCP dissociation[32] and/or (*ii*) increased fraction of h^+ that, after drifting beyond the RZ, "turn back" towards it.

In a simplistic picture, mechanism *(i)* can be visualized as field-induced separation of the opposite charges comprising the exciton and CCP.[1,32] Indeed, it has been shown that this process may reduce the EL by up to 60%.[32] This scenario is in qualitative agreement with modeling of CuPc/α-NPB/Alq_3 devices that showed that under constant bias, carrier densities peak at ~10^{23} cm^{-3} in the RZ, decaying to <10^{20} cm^{-3} in the HTL and ETL, thus generating high internal fields.[9,33,34] In addition, the high barrier for h^+ injection in devices with no HIL or with CuPc obviously results in a high h^+ density at the ITO/α-NPB or ITO/CuPc interface, respectively, under bias. This high h^+ density increases the internal field. As the bias is turned off, this h^+ accumulation layer rapidly dissipates as the h^+ drift back to the anode or towards the RZ. Under reverse bias applied after the end of the bias pulse, this process becomes faster and the spike appears earlier (Figure 5-2).

Mechanism *(ii)* was invoked previously to explain the spikes in some PLEDs.[12] The spike's shift to shorter times under reverse bias (Figure 5-2) supports this mechanism. The drop in the spike amplitude upon replacement of the Alq_3 ETL with BPhen (Figure 5-1(c) vs Figure 5-1(b)) is also in qualitative agreement with this mechanism: As the BPhen is an HBL, its presence very few holes reach the cathode. Turning off the bias at t=0 then makes a smaller difference in the current of h^+ turning back to the RZ than when the BPhen is absent. Yet, if the drop in the spike is due to a smaller difference in the current of holes turning back to the RZ, then we conclude that with no BPhen there is a very poor charge balance and a very strong h^+ leakage into the cathode. Although this may indeed be the case in the Alq_3 OLEDs with no HBL, it has been widely believed that even in these devices, charge injection into the typical Alq_3 OLEDs is reasonably balanced. This point therefore deserves further attention.

In conclusion, following a bias pulse, ITO/CuPc/α-NPB/doped-Alq_3/Alq_3/LiF/Al and other guest-host SMOLEDs exhibit EL spikes at 100-300 ns and μs EL tails. The spikes narrow and shift to shorter times under a reverse bias applied after the pulse. At low temperature they are much stronger, and appear after a slightly longer time. However, they are significantly weaker in devices where the h^+ blocking BPhen is added between Alq_3 and LiF, and absent from devices where MoO_3 replaces CuPc. Good agreement is found between a model based on recombination of CCPs and charges that are initially unpaired, and the observed behavior. The strong amplitude of the spikes, which exceeds the DC EL level is intriguing. It is suspected to result from decreased field-induced quenching of SEs and CCPs following the bias pulse and/or an increased current of h^+

that have drifted beyond the RZ and "turn back" towards the RZ after the applied field is turned off.

Experimental

Arrays of 21×21 OLED pixels, with the general structure ITO/no HIL, CuPc, or MoO_3/α-NPB/doped Alq_3/Alq_3 or BPhen/LiF/Al, were fabricated combinatorially.[19] The dopant in the thin ($0 \leq x \leq 5$ nm) layer of Alq_3 was 1 wt% C6. All depositions were performed in a conventional thermal vacuum evaporation chamber (base pressure ~10^{-6} Torr; the organic layers' deposition rate was ~1 Å/s) installed inside a glove box with <20 ppm O_2.

The 100 μs bias pulses were generated by an Avtech Model AV-1011 with nominal rise and fall times of ~10 ns. The EL was monitored by a Hamamatsu R6060-02 photomultiplier tube with a 50 Ω external load resistance connected to a 350 MHz oscilloscope.

Acknowledgements

Ames Laboratory is operated by Iowa State University for the US Department of Energy (USDOE) under Contract No. DE-AC 02-07CH11358. This work was supported by the Director for Energy Research, Office of Basic Energy Sciences, USDOE.

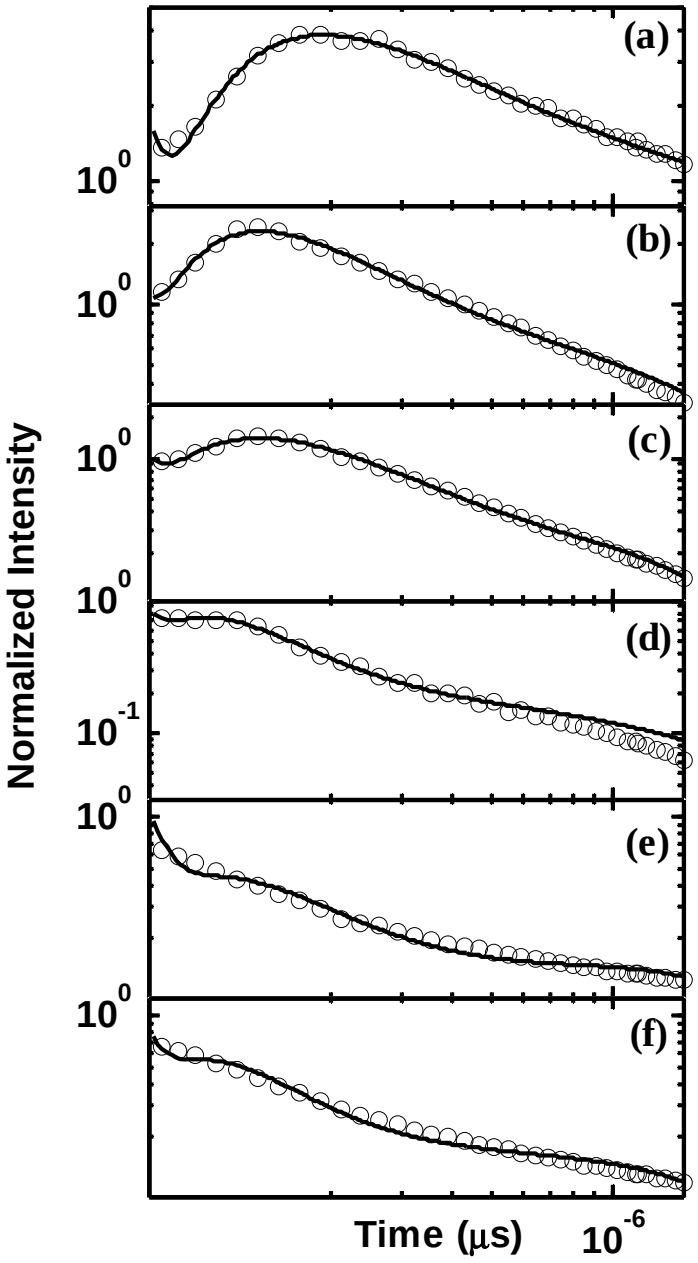

Figure 5-1 The room-temperature transient EL following a 100 μs bias pulse for six devices with different structures, normalized to the DC level. (a) ITO/α-NPB/doped-Alq_3/Alq_3/LiF/Al. (b) ITO/CuPc/α-NPB/doped-Alq_3/Alq_3/LiF/Al. (c) ITO/CuPc/α-NPB/doped-Alq_3/Alq_3/BPhen/ LiF/Al. (d) ITO/CuPc/α-NPB/Alq_3/LiF/Al. (e) ITO/MoO_3/α-NPB/doped-Alq_3/Alq_3/LiF/Al. (f) ITO/MoO_3/α-NPB/doped-Alq_3/Alq_3/BPhen/LiF/Al. The lines are the simulated fittings based on Eq. 11.

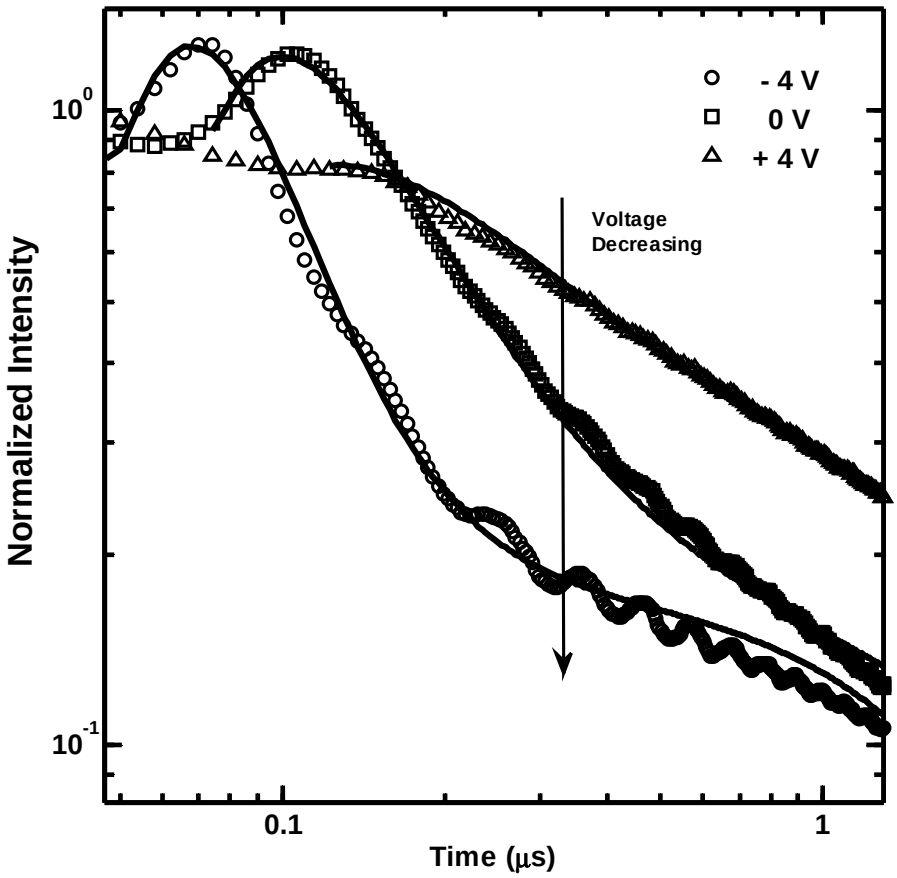

Figure 5-2 The experimental (data points) and simulated (lines) RT normalized transient EL at -4, 0, and 4 V applied at the end of the bias pulse.

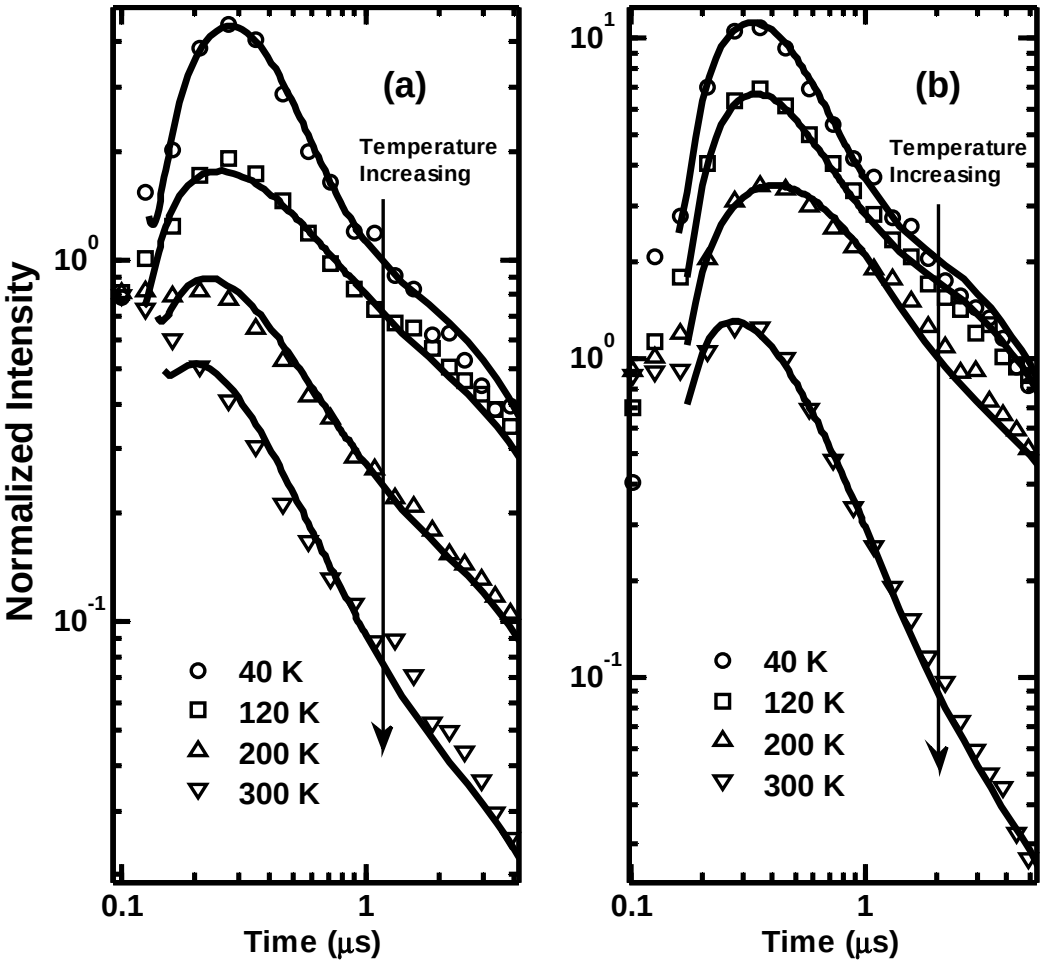

Figure 5-3 The experimental normalized (data points) and simulated (lines) EL of (a) undoped and (b) C6-doped Alq_3 in ITO/CuPc/α-NPB/Alq_3/LiF/Al devices at temperatures $40 \leq T \leq 300$ K.

REFERENCES

1. J. Shinar, R. Shinar, *J. Phys. D* **2008**, *41*, 133001.
2. *Organic Electronics in Sensors and Biotechnology* (Eds: Ruth Shinar, Joseph Shinar), McGraw Hill, NY, **2009**.
3. J. Shinar, V. Savvate'ev, in *Organic Light Emitting Devices: A Survey* (Ed: J. Shinar) Springer Verlag, NY, **2004**, Ch. 1.
4. *Organic Electroluminescence* (Ed: Z. Kafafi), Taylor & Francis, CRC Press, Boca Raton, FL **2005**.
5. J. Kalinowski, *Organic Light-Emitting Diodes: Principles, Characteristics, and Processes,* Marcel Dekker, NY, **2005**.
6. R. F. Service, *Science* **2005**, *310*, 1762-1763.
7. J. Staudigel, M. Stößel, F. Steuber, J. Simmerer, J. Appl. Phys. **1999**, *86*, 3895.
8. E. Tutiš, M.N. Bussac, B. Masenelli, M. Carrard, L. Zuppiroli, J. Appl. Phys. **2001**, *89*, 430.
9. E. Tutiš, D. Berner, L. Zuppiroli, *J. Appl. Phys.* **2003**, *93*, 4594.
10. Y. H. Tak, J. Pommerehne, H. Vestweber, R. Sander, H. Bässler and H. H. Hörhold, *Appl. Phys. Lett.* **1996**, *69*, 1291.
11. J. Kalinowski, N. Camaioni, P. Di Marco, V. Fattori, A. Martelli, *Appl. Phys. Lett.* **1998**, *72*, 513.
12. J. M. Lupton, V. R. Nikitenko, I. D. W. Samuel, H. Bässler, *J. Appl. Phys.* **2001**, *89*, 311.

13. V. Savvateev, J. H. Friedl, L. Zou, J. Shinar, K. Christensen, W. Oldham, L. J. Rothberg, Z. Chen-Esterlit, R. Kopelman, *Appl. Phys. Lett.* **2000**, *76*, 1501.

14. K. O. Cheon, J. Shinar, *Appl. Phys. Lett.* **2004**, *84*, 1201.

15. K. O. Cheon, J. Shinar, *Phys. Rev. B* **2004**, *69*, 201306.

16. D. Y. Kondakov, *J. Appl. Phys.* **2007**, *102*, 114504.

17. D. Y. Kondakov, J. Soc. Info. Dis. **2009**, *17*, 137.

18. The spike's peak location can be affected by the time constant or delay time of the electronics. In the low- and room-temperature measurements the coaxial cables connecting the OLED to the electronics are ~4 and ~1.5 m long, so the spikes peak at 200–300 and 100 – 200 ns, respectively.

19. L. Zou, V. Savvate'ev, J. Booher, C.-H. Kim, J. Shinar, *Appl. Phys. Lett.* **2001**, *79*, 2282.

20. R. Liu, Z. Gan, R. Shinar, and J. Shinar, unpublished.

21. The field-dependent electron mobility in Alq_3 and hole mobility in α-NPB are ~10^{-4} cm^2/Vs, so if the potential drop across each of these layers is ~4 V, the transit time through the ~45 nm-thick HTL & ETL is ~50 ns.

22. A. Mozumder, *J. Chem. Phys.* **1968**, *48*, 1659.

23. M. A. Lampert, P. Mark, *Current Injection in Solids*, Academic Press, New York, **1970**.

24. P. E. Burrows, Z. Shen, V. Bulovic, D. M. McCarty, S. R. Forrest, J. A. Cronin, M. E. Thompson, *J. Appl. Phys.* **1996**, *79*, 7991.

25.M. Pope and C. E. Swenberg, *Electronic Processes in Organic Crystals and Polymers*, Oxford University Press, **1999**.

26. S. Karg, J. Steiger, H. von Seggern, *Synth. Met.* **2000**, *111-112*, 277.

27 J. Kakalios, R. A. Street, W. B. Jackson, *Phys. Rev. Lett.* **1987**, *59*, 1037.

28. D. L. Huber, *Phys. Rev. E.* **1996**, *53*, 6544.

29. The second and third terms of Eq. (11) are due to the carriers' random walk within the CCPs and to uncorrelated carriers present at t>50 ns, respectively.

30. β increases from 0.38 to 0.59 as the bias increases from 7 to 11 V. This is likely due to the change in the energy distribution of the trapped charges.

31. T. Nakazawa, M. Asano, S. Fujita, S. Fujita, *Jpn. J. Appl. Phys., Part 2* **1999**, ***38***, L206.

32. R. Kersting, U. Lemmer, M. Deussen, H. J. Bakker, R. F. Mahrt, H. Kurz, V. I. Arkhipov, H. Bässler, and E. O. Göbel, *Phys. Rev. Lett.* **1994**, *73*, 1440.

33. Igor Yu. Goliney, *Synth. Met.* **2000**, *111-112*, 359.

34. B. Masenelli, E. Tutis, M. N. Bussac, L. Zuppiroli, *Syn. Met.* **2001**, *121*, 1513.

CHAPTER 6 GENERAL CONCLUSION

In summary, there are two major research works presented in this dissertation. The first research project (Chapter 4) is spectrally narrowed edge emission from Organic Light Emitting Diodes. The second project (Chapter 5) is about transient electroluminescent dynamics in OLEDs.

Chapter 1 is a general introduction of OLEDs. Chapter 2 is a general introduction of organic semiconductor lasers. Chapter 3 is a description of the thermal evaporation method for OLED fabrication.

The detail of the first project was presented in Chapter 4. Extremely narrowed spectrum was observed from the edge of OLED devices. A threshold thickness exists, above which the spectrum is narrow, and below which the spectrum is broad. The FWHM of spectrum depends on the material of the organic thin films, the thickness of the organic layers, and length of the OLED device. A superlinear relationship between the output intensity of the edge emission and the length of the device was observed, which is probably due to the misalignment of the device edge and the optical fiber detector. The original motivation of this research is for organic semiconductor laser that hasn’t been realized due to the extremely high photon absorption in OLED devices. Although we didn’t succeed in fabricating an electrically pumped organic laser diode, we made a comprehensive research in edge emission of OLEDs which provides valuable results in understanding light distribution and propagation in OLED devices.

Chapter 5 focuses on the second project. A strong spike was observed at the falling edge of a pulse, and a long tail followed. The spike was due to the recombination of correlated charge pair (CCP) created by trapped carriers in guest molecules of the recombination zone. When the bias was turned off, along with the decreasing of electric field in the device, the electric field induced quenching decreases and the recombination rate of the CCP increases which result in the spike. This research project provides a profound understanding of the EL dynamics of OLED, and the theoretical model can fit and explain the experiment data quite well.

For the edge emission, we focused on the spectrum and the relative intensity of the edge emission. In the future, more research can be done on the comparison of the intensity between the total edge emission and the surface emission which will give us a sense what fraction of light was trapped in the device. Micro structures can be integrated into the OLED such as DFB and DBR, the character of edge emission should be very interesting.

For the transient spike, the CCP model can give a good explanation. But in the model, the effect of the electric field change is not included, because from the start point (t=0), we assume the mobility of carriers is a constant. If we consider the details of the change of the electric field, then when turning of the bias, the decrease of the electric field results in decrease of the carrier mobility and the dissociation rate. If we can add the electric field effect into the model, the whole theory will be more convincing.